Analysis, Design, Simulation, and Measurements of Flexible High Impedance Surfaces

by

Ahmet Cemal Durgun

A Dissertation Presented in Partial Fulfillment
of the Requirements for the Degree
Doctor of Philosophy

Approved November 2013 by the
Graduate Supervisory Committee:

Constantine A. Balanis, Chair
James T. Aberle
Hongyu Yu
Bertan Bakkaloglu

ARIZONA STATE UNIVERSITY

December 2013

ABSTRACT

High Impedance Surfaces (HISs), which have been investigated extensively, have proven to be very efficient ground planes for low profile antenna applications due to their unique reflection phase characteristics. Another emerging research field among the microwave and antenna technologies is the design of flexible antennas and microwave circuits to be utilized in conformal applications. The combination of those two research topics gives birth to a third one, namely the design of *Conformal or Flexible HISs (FHISs)*, which is the main subject of this dissertation.

The problems associated with the FHISs are twofold: characterization and physical realization. The characterization involves the analysis of scattering properties of FHISs in the presence of plane wave and localized sources. For this purpose, an approximate analytical method is developed to characterize the reflection properties of a cylindrically curved FHIS. The effects of curvature on the reflection phase of the curved FHISs are examined. Furthermore, the effects of different types of currents, specifically the ones inherent to finite sized periodic structures, on the reflection phase characteristics are observed.

After the reflection phase characterization of curved HISs, the performance of dipole antennas located in close proximity to a curved HIS are investigated, and the results are compared with the flat case. Different types of resonances that may occur for such a low-profile antenna application are discussed. The effects of curvature on the radiation performance of antennas are examined.

Commercially available flexible materials are relatively thin which degrades the bandwidth of HISs. Another practical aspect, which is related to the substrate thickness, is the compactness of the surface. Because of the design limitations of conventional HISs, it is not possible to miniaturize the HIS and increase the bandwidth, simultaneously. To overcome this drawback,

a novel HIS is proposed with a periodically perforated ground plane. Copper plated through holes are extremely vulnerable to bending and should be avoided at the bending parts of flexible circuits. Fortunately, if designed properly, the perforations on the ground plane may result in suppression of surface waves. Hence, metallic posts can be eliminated without hindering the surface wave suppression properties of HISs.

To my grandparents

ACKNOWLEDGEMENTS

I would like to express my gratitude to my advisor Prof. Constantine Balanis for his invaluable guidance throughout my studies. It has been an honor for me to have the opportunity to work with such a world-renowned professor. I believe that this will remain as one of the most important experiences of my life.

I also would like to thank to my committee members Prof. James Aberle, Prof. Hongyu Yu, and Prof. Bertan Bakkaloglu for their helpful suggestions and constructive criticism.

It is a pleasure to acknowledge Craig Birtcher for his exceptional work and assistance to perform the measurements. I would not be at this point without his help. I have enjoyed the time when working with him and have learned a lot from him. I am also appreciative to Hai Huang for all of his efforts to fabricate the Perforated High Impedance Surface.

My special thanks go to my family for their continuing support and encouragement. I would not be able to pursue my Ph.D. without their understanding, patience, and sacrifice.

In addition, I would like to thank to my labmates Nafati Aboserwal, Mikal Askarian-Amiri, Wengang Chen, Victor Kononov, Sivaseetharaman Pandi, Alix Rivera-Albino, and Manpreet Saini for the cheerful environment and joyful moments they shared with me.

I am also grateful to my Turkish friends who live in Arizona for being my family away from home. They have been extremely helpful and supportive that I will never forget.

Last but not the least, I would like to utter my gratitude to my beloved wife Pinar Cay Durgun for her enormous understanding and patience. Although we were separated during the first two years of my studies, I have always felt her nearby, and it was this feeling which kept me strong enough to complete my degree.

This work was supported by the ASU Advanced Helicopter Electromagnetics Program.

TABLE OF CONTENTS

CHAPTER Page

LIST OF TABLES

LIST OF FIGURES

Figure Page

Figure Page

Figure Page

CHAPTER 1

INTRODUCTION

In some antenna applications, the radiating elements are placed on a conducting plane which is referred to as the *ground plane*. For instance, if an antenna is mounted on a vehicle, the structure of that vehicle behaves as the ground plane. In such a case, two different fields contribute to the radiated field; the direct field from the radiating element and the fields reflected from the ground plane. The reflected fields can be treated by introducing some virtual sources, so called *images* [1]. For a flat and infinite in extent PEC ground plane, the distance between the image and the ground plane is exactly the same as that of the source. Also, in the case of a horizontal electric current, the directions of the actual and the image currents are opposite. Therefore, the radiated fields from the actual source and its image tend to cancel each other as the source gets closer to the ground plane. Hence, for many conformal antennas, the proximity of a conducting backplane to the radiating element is detrimental to its performance. To alleviate this shortcoming, there are two possible scenarios. The antenna can be elevated by a proper height from the metallic surface of the vehicle on which it is mounted. However, for aircraft, this is not desirable as it would disturb the aerodynamics and airfoil contours. In addition, an antenna protruding above a vehicle's surface might represent a compromise in operational security and radar visibility (RCS). The conventional alternative is to recess the antenna into a cavity in the vehicle's surface, the depth of which places the radiating element flush with the surface while being separated from the bottom of the cavity by an appropriate distance.

A relatively new third alternative has been attracting some attention in the electromagnetic community, which is placing the antenna in close proximity to a surface, with unique properties, that will not:

- conduct AC currents (at frequencies within the designed bandwidth)
- reverse the phase of reflected fields
- support propagating surface waves.

These surfaces are referred to as *Artificial Magnetic Conductors (AMCs)*, or *High Impedance Surfaces (HISs)*. Indeed, many scientists and engineers have been working on HISs for a few decades. Some of the applications of HISs are [1]:

- Change the surface impedance
- Control the phase of the reflection coefficient
- Manipulate the propagation of surface waves
- Control the edge diffractions, especially of horns and reflectors
- Decrease the coupling between the elements in an antenna array
- Design new boundary conditions to control the radiation pattern of small antennas
- Provide detailed control over the scattering properties
- Design tunable impedance surfaces to be used as steerable reflectors and steerable leaky-wave antennas

The very first example of such surfaces are corrugated surfaces, which are very effective in terms of suppressing surface wave propagation and reflection wave characteristics. However, since the depth of the corrugations should be almost a quarter wavelength, they are not appropriate for low-profile antenna applications. For space borne and stealth type of applications,

HISs, which require much smaller height than the wavelength, are more desirable because of aerodynamic and radar visibility considerations.

The physical distance between an antenna and the ground plane can be decreased by inserting a dielectric material between the two. Also, it is known that, under plane wave incidence, a dielectric material can be modeled as an equivalent capacitance; similarly a capacitance can be replaced by a dielectric slab. Thus, the distance between an antenna and the ground plane can be further decreased with the aid of an extra capacitive loading of the dielectric slab, at the expense of decreased bandwidth [2]. A practical realization of such a surface is the HIS where the capacitive loading is achieved by the array of metallic patches. Since HISs, within certain bands, do not conduct AC currents nor reverse the phase of the reflected fields, an antenna can be mounted flush on them without hindering its radiation performance. In addition, the surface wave suppression properties are attained by the inclusion of metallic posts. These properties of HISs make them desirable for low-profile and conformal antenna applications.

HISs have been efficiently utilized in the design of low-profile wire antennas including dipoles [3], curl antennas [4], bent monopoles [4], folded dipoles [5], wideband dipoles [6], [7] and single dipoles radiating circularly polarized fields [4]. Because of their unique reflection phase characteristics, HISs are also used for antenna miniaturization and bandwidth enhancement [6]- [8]. Due to the surface wave suppression, the edge diffractions from the finite size ground planes have been reduced, and smoother radiation patterns have been obtained for monopole and aperture antenna applications [9]. Moreover, scan blindness in an array of dipoles has been significantly decreased [10]. Similarly, coupling between patch antennas can be reduced [4], [11] which improves their overall performance. The enhancement of band-

width and gain of linearly [12] and circularly [13] polarized patch antennas by HISs has also been reported in the literature.

HISs can also be tuned electronically, via varactor diodes and DC bias lines for instance, to obtain a dynamic center frequency and operational band. Those surfaces have been utilized in the design of reflect surfaces [14] and forward and backward leaky wave antennas [15] where electronic beam steering is possible. Another interesting area of application is the generation of microwave holography [16]. Finally, they can also be used as wideband absorbers, if the dielectric substrate is replaced with a lossy one [17].

1.1. Scope of the Work

Because of the aforementioned attractive properties of HISs, they have been extensively investigated by many engineers and scientists. However, the impact of bending on the characteristics of HISs have not received much attention. Indeed, to the author's best knowledge, this is the first time that curved HISs are examined in great detail. At this point, the reader may ask the question: Why do we need to investigate properties of bent or curved HISs, other than pure academic interests? To answer this, it may be useful to turn our heads to another emerging research topic that began to arouse the interest of researchers, which is the design of flexible antennas that can conform with surfaces of any geometry and operate in harsh environmental conditions. Several types of flexible antennas with different flexible substrates can be found in the literature [18]- [20]. Indeed, the design, fabrication and testing of flexible bow-tie antennas have already been investigated and reported by our research team [18]. The physical properties of flexible antennas make them promising candidates for conformal antenna applications. On the other hand, the successful results obtained by HISs, in the radiation performance improve-

ment and low profile antenna realizations, enhanced their utilization in radiating systems. The combination of these two factors, together with the increasing interest in flexible antennas, led our research team to a quest of a conformal artificial ground plane, referred to as *Flexible High Impedance Surfaces* (FHIS).

The next question can be about the basic problems that may be anticipated during this research. Since, this is the first time that FHISs are being investigated, similar to the flat case, we should start with the characterization of the surface. The effects of bending and the level of curvature, on the reflection phase characteristics, should be examined properly. This includes the investigation of FHIS responses for both plane wave and localized source incidences.

In addition to the characterization problem, there are a few practical concerns regarding FHISs. For instance, the selection of the dielectric material is extremely crucial for the design of FHISs. The material should be capable of bending without damaging its electrical properties. *DuPont Pyralux polyimide* [21] is a promising candidate that can fulfill the desired specifications and can be used in the design. However, the thickness of the commercially available samples of this material is very small for X-band applications. This issue introduces some limitations, which will be discussed in Chapter 2, in terms of bandwidth and size of the surface. If the thickness of the substrate is too small compared to the wavelength, then the bandwidth of the FHIS will be too narrow resulting in impractical designs. Hence, bandwidth enhancement is one of the challenging problems related to FHIS design.

Another practical problem may be observed in the presence of metallic posts (vias). It is known that, metallic posts or copper plated through holes in the bending regions of a flexible circuit are extremely vulnerable and should be avoided. Since the copper can easily crack

and fail when flexed, some other solution has to be found for the surface wave suppression problem.

In brief, the basic problems related to the design and physical realization of FHISs are threefold: reflection phase characterization, bandwidth improvement and elimination of metallic posts. Indeed, the aim of this study is to find practical solutions to these problems. The accomplishments of this study can be listed as follows.

- A semi-analytical approach is developed to obtain the reflection phase diagram of a FHIS which is curved in the form a cylinder.
- The effects of curvature on the reflection characteristics of a FHIS are investigated for plane wave and localized source incidences.
- A novel type of HIS is proposed to alleviate bandwidth limitations of conventional HISs.
- It is verified that the same novel structure can also be used to eliminate copper plated through holes (vias), without hindering the surface wave suppression capabilities.

1.2. Outline of the Dissertation

The remaining part of the dissertation is comprised of five chapters.

A brief review of conventional HISs, including the geometry and analytical models, is provided in Chapter 2. The behavior of HISs is discussed by examining a typical reflection phase diagram. Surface wave suppression properties of HISs are summarized together with the basic design limitations.

Chapter 3 begins with a discussion on the practical concerns about the physical realization of FHISs. Then, a semi-analytical method is developed for the characterization of FHISs. The

effects of curvature on the reflection phase are investigated. The types of currents excited on a periodic structure are introduced and their effects on the characteristics of FHISs are discussed. Lastly, the claims are verified with simulations and measurements.

Chapter 4 is devoted to the wire antenna applications of FHISs. A different definition of an operational band is provided for low-profile antenna applications, which is followed by a discussion on different types of resonances that can occur when an antenna is located in close proximity to an HIS. The effects of curvature on those different types of resonances are analyzed. The performance of antennas on a curved HIS is contrasted with the flat case.

Chapter 5 focuses on a novel type of HIS which overcomes the bandwidth limitation of conventional HISs. This new type of HIS includes a periodically perforated ground plane, instead of a solid one as in conventional HISs. In addition, these structures are verified to be capable of suppressing surface wave propagation, provided that the geometry of the perforations is designed judiciously. Therefore, with this type of HISs, it is possible to eliminate the metallic posts without hindering surface suppression properties. It is also possible to overlap the AMC and surface wave suppression bands.

Finally in Chapter 6, all of the work performed during this study is summarized. The advantages and disadvantages of the methods and the structures suggested in this project are discussed, and concluding remarks are stated. Lastly, possible future endeavors, as a continuation of this dissertation, are pointed out.

CHAPTER 2

HIGH IMPEDANCE SURFACES

HISs are artificially engineered two-dimensional periodic structures which behave like magnetic conductors within specified frequency bands. This geometry gives HISs unique reflection phase properties. In addition, due to their periodic configuration, HISs exhibit a stop band which occurs when the period of the surface is on the order of a half wavelength. Therefore, these types of surfaces are also denoted as *Photonic Band Gap (PBG)* or *Electromagnetic Band Gap (EBG)* structures. On the other hand, in some applications, the dielectric substrate can be perforated by metallic posts, which are referred to as *vias*, as shown in Fig. 2.2. This type of HIS is generally referred to as a *mushroom* surface. The vias result in a stop band and suppression of unwanted surface wave propagation at sub-wavelength frequencies [22]. It is worth mentioning that reflection phase and stop bands of a HIS may not overlap and they are not directly dependent. Hence, for an AMC type of an application, the vias are not necessary.

In addition to mushroom surfaces, there are other types of HISs that utilize special types of patches, to eliminate the vias, for surface wave suppression at sub-wavelength frequencies. These HISs are referred to as *Uniplanar Compact Photonic Band Gap (UCPBG)* structures [23], [24].

In this chapter, reflection phase and surface wave suppression characteristics of conventional HISs are summarized. Two different analytical models are contrasted and basic design limitations are discussed.

2.1. Surface Geometry

There are numerous configurations of HISs, but they all share some basic common characteristics. Generally, a conventional HIS is composed of a periodically arranged array of metallic patches mounted on a relatively thin, grounded dielectric substrate. A schematic drawing

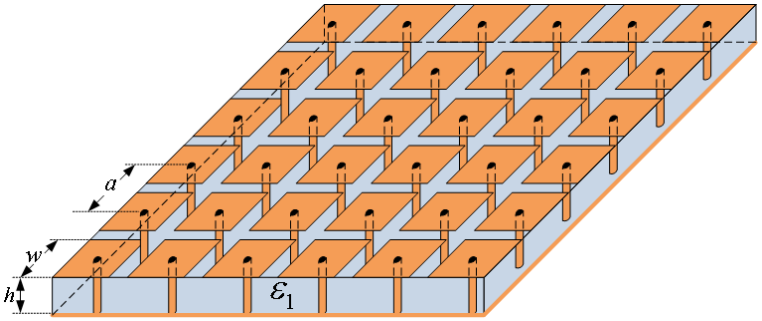

Fig. 2.1. Geometry of a mushroom surface.

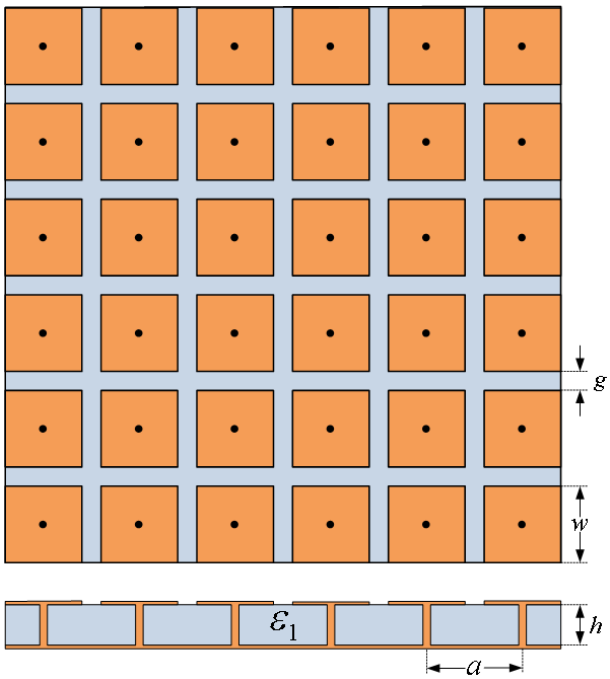

Fig. 2.2. Top and side views of the mushroom surface.

of a mushroom surface is shown in Figs. 2.1 and 2.2 where the distance between the vias, the patch width, the gap between the patches, the height and permittivity of the dielectric material are denoted by a, w, g, h and ε_1, respectively.

An "effective medium" model can be used to analyze mushroom surfaces [22]. HISs can be modeled with lumped circuit elements provided that the periodicity of the surface is much smaller than the wavelength at the operating frequency [22]. If the dimensions of the con-

ducting patches are electrically small, then the surface can be modeled by a capacitance and an inductance connected in shunt. The capacitance of the surface is primarily due to the gap between the conducting plates on the top of the dielectric substrate and the inductance is primarily due to the current loop generated within the unit cell [22]. In case of a HIS without any vias, the inductance is due to the close proximity of the ground plane to the capacitive array of patches. Fig. 2.3 shows the unit cell and the equivalent circuit of the mushroom surface.

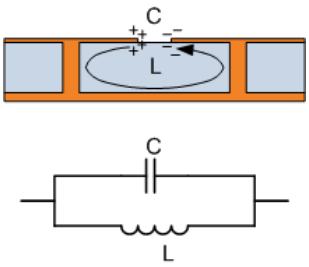

Fig. 2.3. Unit cell of a mushroom surface and its equivalent circuit.

Using the equivalent circuit illustrated in Fig. 2.3, the surface impedance of the individual unit cell can be expressed as in (3.1).

$$Z_s = \frac{j\omega L}{1-\omega^2 LC} \tag{2.1}$$

Hence, the resonant frequency and the bandwidth of such a structure can be obtained by (2.2) and (2.3), respectively. In these expressions, the constitutive parameters of free space are denoted by ε_0 and μ_0. The bandwidth of the structure is defined as the frequency interval where the phase of the reflection coefficient of a normal plane wave incidence varies between $+90^\circ$ and -90°.

$$\omega_0 = \frac{1}{\sqrt{LC}} \tag{2.2}$$

$$BW = \frac{\sqrt{L/C}}{\sqrt{\mu_0/\varepsilon_0}} \tag{2.3}$$

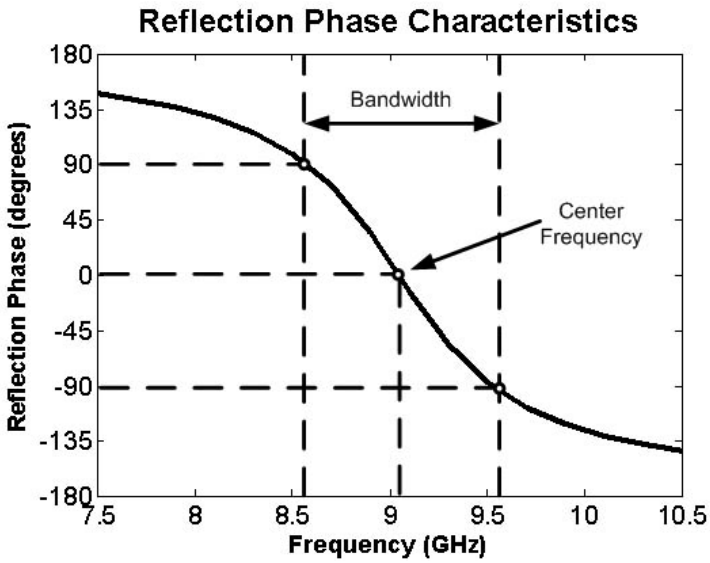

Fig. 2.4. Typical reflection phase diagram of a HIS. The reflection phase is equal to zero at the center frequency. The bandwidth of the structure is defined as the frequency interval where the reflection phase lies between $+90^\circ$ and -90°.

A typical reflection phase diagram of a HIS is shown in Fig. 2.4. The surface behaves like a perfect magnetic conductor (PMC) at the center frequency, since the reflected field is in phase with the incident field. The reflected and incident fields interact constructively when the phase difference remains between $+90^\circ$ and -90°. In the remaining regions of the frequency spectrum, they interact destructively resulting in a degradation in the radiation performance. As the reflection phase approaches 180°, the surface starts to behave like a perfect electric conductor (PEC).

The equivalent surface inductance and capacitance of the HIS structure are given by (2.4) and (2.5), respectively [22].

$$L = \mu_1 h \tag{2.4}$$

$$C = \frac{\omega(\varepsilon_1 + \varepsilon_2)}{\pi} \cosh^{-1}\left(\frac{a}{g}\right) \tag{2.5}$$

It is apparent that, assuming a non-magnetic material, the inductance of the surface depends only on the thickness of the dielectric substrate. On the other hand, the capacitance is a function of the substrate permittivity, patch size and proximity. These relations will be used to explain the design limitations of HISs in the subsequent sections of this chapter. Although there are more accurate models and corresponding equations, in this part of the dissertation these simpler expressions are preferred as they provide a physical insight for the structure. A more accurate transmission line model is given in the next section.

2.2. Transmission Line Model

A transmission line model can be developed for a HIS as shown in Fig. 2.5 where Z_P denotes the impedances of the array of patches. The dielectric layer behaves as an impedance transformer of length h, which is the thickness of the substrate. Z_0 is the wave impedance in the surrounding medium which depends on the angle of incidence (θ) as well as the polarization of the incident field. The angle of incidence is defined from the $z-$axis, which also coincides with the normal of the surface. The transmission line is truncated by a short circuit which represents the ground plane.

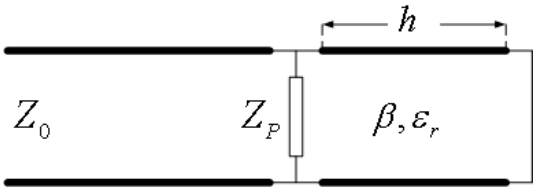

Fig. 2.5. Transmission line model of the HIS.

The details of the derivation of the transmission line model are given in [25]. In this report, only the essential parts are repeated, for the sake of completeness. To obtain the impedance of the patch array, the first step is to solve for the scattered fields of an array of wires under plane wave incidence. Then, an averaged boundary condition is used to relate the average surface currents to the total electric field. Surface impedance of the array of wires can be obtained by using this relation. Since, the scattered fields from an array of wires are approximately identical to those of a wire grid, which is the complementary surface of array of patches, the surface impedance of the wire grid is also very close to that of the array of wires. Finally, Babinet's principle is applied to obtain the surface impedance of the array of patches. The expressions for the surface impedance for two different polarizations are represented by (2.6) and (2.7).

$$Z_P^{TM} = -j\frac{\eta_{eff}}{2\alpha_P} \tag{2.6}$$

$$Z_P^{TE} = -j\frac{\eta_{eff}}{2\alpha_P\left(1-\frac{k_0^2}{k_{eff}^2}\frac{\sin^2\theta}{2}\right)} \tag{2.7}$$

Since the sign of the impedance is negative, the array of patches has a capacitive impedance. In these equations, α_P is referred to as the *grid parameter* and is represented by (2.8).

$$\alpha_P = \frac{k_{eff}a}{\pi}\ln\left(\frac{1}{\sin\frac{\pi(a-w)}{2a}}\right) \tag{2.8}$$

When the surrounding medium is air, the effective permittivity is approximated by (2.9), where ε_r is the relative permittivity of the dielectric layer.

$$\varepsilon_{eff} = \frac{\varepsilon_r + 1}{2} \tag{2.9}$$

Assuming the substrate is non-magnetic, the effective intrinsic impedance (η_{eff}) and the propagation constant (k_{eff}) of the medium are represented, respectively by (2.10) and (2.11).

$$\eta_{eff} = \sqrt{\frac{\mu_0}{\varepsilon_{eff}}} \tag{2.10}$$

$$k_{eff} = \omega\sqrt{\mu_0 \varepsilon_{eff}} \tag{2.11}$$

Fig. 2.6 illustrates the reflection phase of a HIS with no vias comprised of square patches with width (w) of 4.1 mm and a periodicity (a) of 5 mm. The thickness and the relative permittivity of the dielectric substrate are 1.524 mm and 2.33, respectively. The reflection phase is calculated by two different methods and the results are compared with the full-wave solution. It is seen that the transmission line model gives more accurate result compared to Sievenpiper's effective medium model.

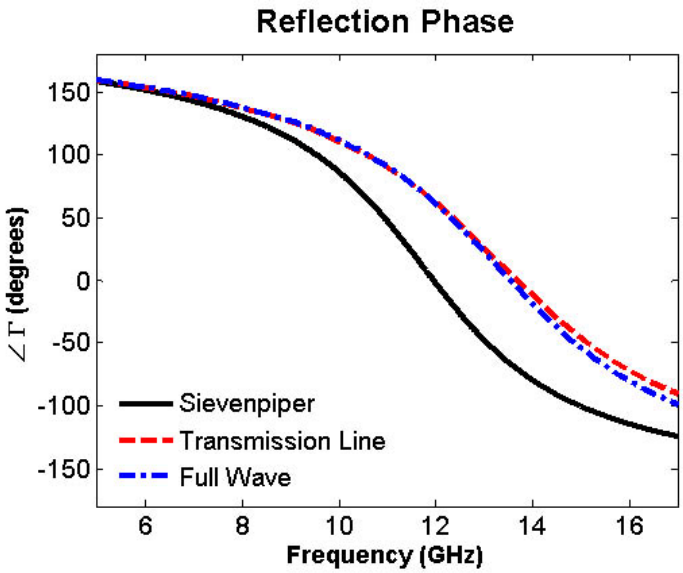

Fig. 2.6. Comparison of the reflection phases obtained by different methods.

2.3. Surface Wave Suppression

As mentioned previously, HISs are capable of suppressing surface waves provided that the dielectric substrate is perforated with metallic posts. In the absence of the vias, surface waves cannot be suppressed since no stop bands occur at the sub-wavelength frequencies. The stop and pass bands of a HIS can be determined with the aid of the dispersion diagram of the structure. Fig. 2.7 shows the dispersion of the HIS whose reflection phase is exhibited in Fig. 2.6. At very low frequencies, the TM modes begin to propagate since they do not have a cutoff frequency, and they continue to propagate even after the TE modes start to propagate. Therefore, the HIS with no vias do not have a stop band below 20 GHz.

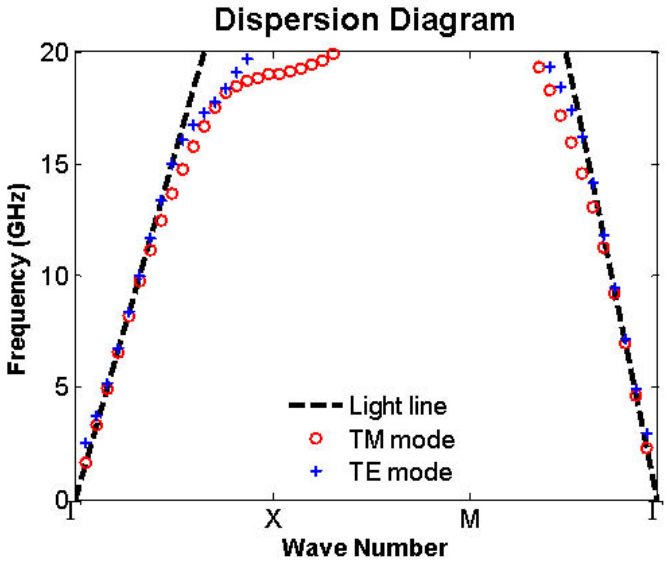

Fig. 2.7. Dispersion diagram of the HIS without vias, obtained by full-wave simulation.

On the other hand, when vias are added to the structure, the TM modes behave differently. For the TM modes, the electric field is parallel to the metallic posts. So, if the surface wave enters the "forest of vias," after a certain frequency, the medium starts to behave as a left handed material, and all the energy is reflected back. This property can be observed by again utilizing

the dispersion diagram displayed in Fig. 2.8. This diagram is particularly for the mushroom surface which has exactly the same unit cell dimensions with the HIS whose reflection phase and dispersion diagram are exhibited, respectively, in Figs. 2.6 and 2.7; the only difference is the inclusion of vias of radius 0.25 mm. It is clear that, just above 9 GHz, the slope of the dispersion curve of the TM mode is negative. Nevertheless, the dispersion curve for the TE mode is almost the same as that of the previous case. The TE polarized surface waves start to propagate around 15 GHz where the dispersion curve crosses the light line. Since there are no possible bound modes between 9 and 15 GHz, the surface waves are suppressed within this interval.

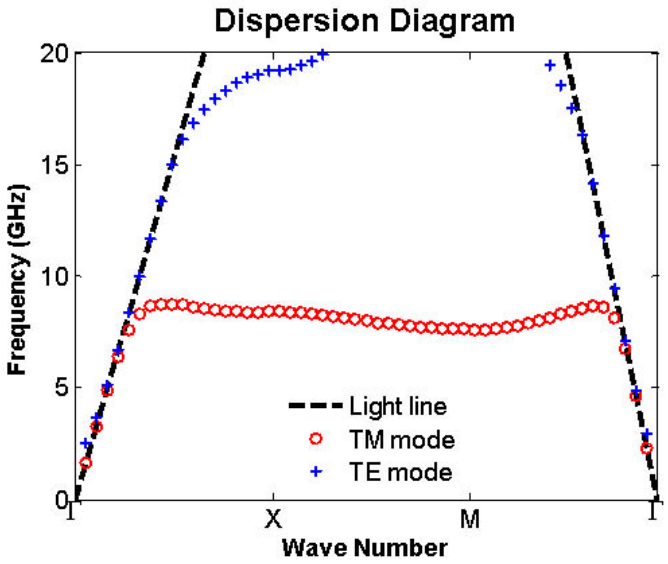

Fig. 2.8. Dispersion diagram of the HIS with vias, obtained by full-wave simulation.

2.4. Design Limitations of HIS

Design limitations of HISs can be understood by examining their physical geometry and analytical model. Although there are several quantitative methods that already have been re-

ported in the literature [26]- [28], a qualitative approach will be followed here to summarize those results.

A conventional HIS is comprised of a periodically arranged array of metallic patches mounted on a grounded dielectric substrate, and it can be modeled by a parallel *LC* circuit, provided that the periodicity of the surface is much smaller than the wavelength at the operating frequency [22]. Hence, the center frequency and the bandwidth are proportional to $\sqrt{LC}$ and $\sqrt{L/C}$, respectively. The capacitance of the surface is due to the gap between the conducting plates on the top of the dielectric substrate and the inductance is due to the ground plane in close proximity to the array of patches. In the literature, there are several analytical models and expressions for the equivalent inductance and capacitance of an HIS [22], [29], [30]. All of those models approach the problem from a different point of view and arrive with different expressions. However, it is common in all of them that the capacitance depends on the patch size and proximity. On the other hand, the inductance and fractional bandwidth depend only on the thickness of the substrate [22]. Because of these reasons, the basic limitation in the design procedure is on the bandwidth.

For a fixed substrate thickness, we do not have control of center frequency and bandwidth at the same time. Once either the center frequency or the bandwidth is specified, the other depends upon it. Furthermore, the entire frequency range cannot be accommodated by using reasonable patch dimensions.

Low-profile applications usually exhibit small bandwidths because of thin substrates. Moreover, since the inductance of a conventional HIS depends only on the thickness, the frequency of operation can be tuned by varying the capacitance of the surface. Expectedly, relatively lower operating frequencies can be achieved only by increasing the capacitance of

the surface. This can be realized by decreasing the gap between the patches, increasing the patch size and/or using the aforementioned patch geometries. However, this either contradicts with the compactness or large bandwidth requirements. Consequently, it is not possible to miniaturize the unit cell and enhance the bandwidth at the same time.

CHAPTER 3

PLANE WAVE SCATTERING FROM FLEXIBLE HIGH IMPEDANCE SURFACES

Design of FHISs is a new research topic and to the best of our knowledge, FHISs have not been investigated by any other person, previously. Hence, the first thing that should be considered is the physical realization of such a surface. If FHISs are found to be feasible in terms of fabrication, then reflection phase characterization should be performed. A rigorous design procedure can only be developed after the completion of these steps. Therefore, this chapter begins with the material selection and physical realization of FHISs and continues with their reflection phase characterization under plane wave incidence. For this purpose, an analytical approach, which assumes a homogenized model for the curved HIS, is suggested, and then compared with simulations. The parameters of the model are extracted from the reflection properties of the flat HIS. In addition, the effects of surface waves are examined in great detail, and the results are verified with measurements.

3.1. Physical Realization

The fabrication process of the FHIS starts with an investigation of an appropriate flexible material. After an extensive survey, *DuPont Pyralux polyimide* was selected as the dielectric substrate of the FHIS. This is a 10 mil($\sim$ 0.254mm)-thick substrate with 2.0 oz copper cladding on both sides. It is known that the bandwidth of a HIS depends on the thickness of the substrate. The thickness of the ployimide, resulting in a narrow bandwidth, makes it inconvenient for X-band (8-12 GHz) operations. Hence, to improve the bandwidth of the FHIS, it is suggested to glue two samples of polyimide on top of each other after removing the copper cladding on one side of each sample. For this purpose, *3M's 300 LSE* [31] low energy acrylic transfer adhesive is employed to adhere the samples. Together with the adhesive, the thickness of the

new substrate becomes 25 mils ($\sim$ 0.635mm) which can result in a practical bandwidth. Fig. 3.1 illustrates a schematic drawing of this new substrate.

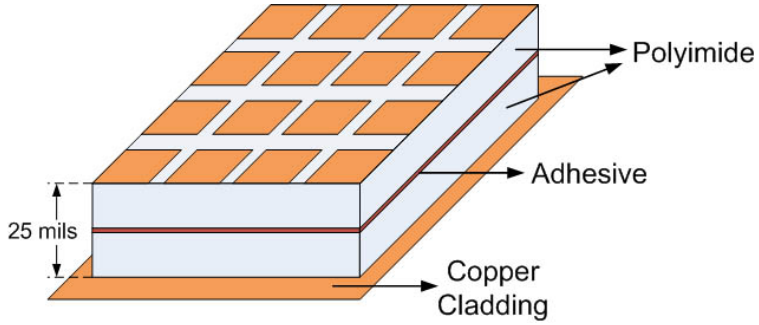

Fig. 3.1. Schematic drawing of the FHIS after the adhesion of the two samples and chemical etching.

Another issue regarding the polyimide and the adhesive is their electrical properties. The relative permittivity of polyimide is 3.3. However, there is no accurate information about the relative permittivity of the adhesive. According to the limited and estimated data, the relative permittivity of the adhesive is assumed to be close to that of the polyimide. Thus, the adhesive layer is not included in the numerical model.

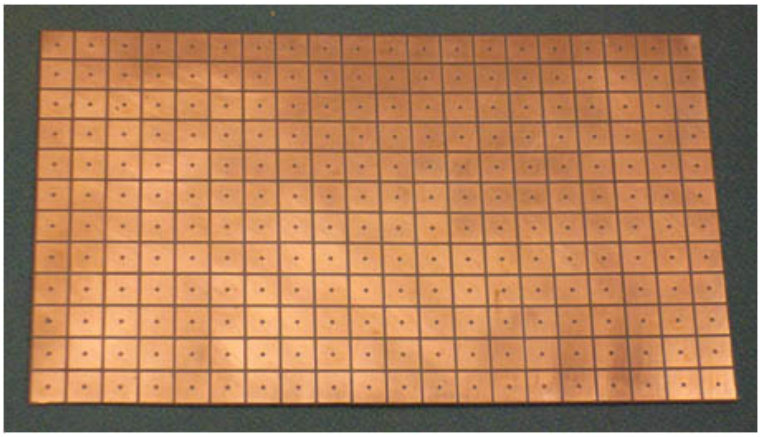

Fig. 3.2. FHIS after photolithography and chemical etching.

The periodic geometry of the FHIS, which is composed of square patches, is obtained by photolithography which is similar to making photographic contact prints. A negative of the image (the copper "artwork") is generated on a transparent film. This is referred to as the "mask". The mask is placed on top of the photo-sensitized substrate, which is then exposed to UV light. The substrate is developed to harden the parts of the "photo-resist" that are exposed, and then washed to remove the parts of the photo-resist that are shielded from the light by the mask. Finally, the copper cladding of the substrate that is not covered by the photo-resist pattern is chemically etched away. The finalized FHIS is displayed in Fig. 3.2.

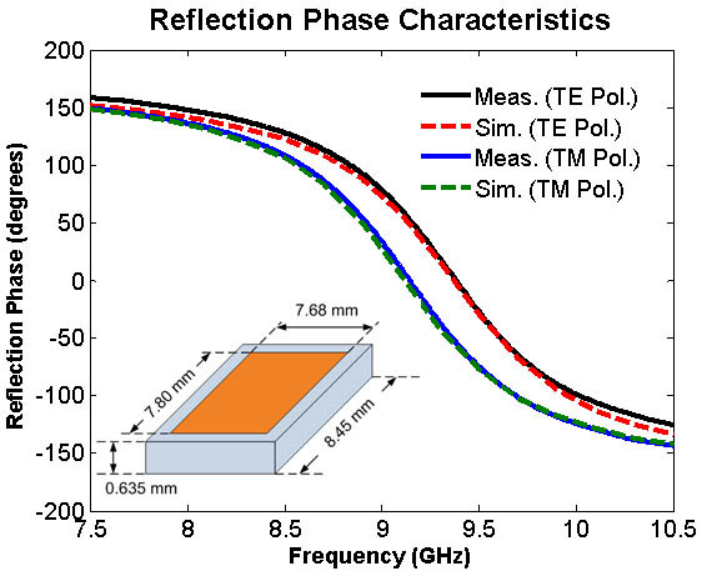

Fig. 3.3. Reflection phase of the fabricated FHIS.

Initially, it was targeted to fabricate an HIS with a patch width and proximity of 7.9 mm and 0.5 mm, respectively. However, due to the tolerances of the in-house fabrication process, slightly different patch widths and gaps for each cell were obtained. The averaged patch widths are 7.80 mm and 7.68 mm in two different principal axes; similarly, the averaged gaps are 0.65 mm and 0.77 mm. Hence, the reflection phase curve of the fabricated FHIS is polarization

dependent. Fig. 3.3 displays the simulated and measured reflection phases of the flat FHIS for TE and TM polarizations; a good agreement is indicated. The center frequencies are 9.2 and 9.38 GHz, respectively.

3.2. Simulations

As it is mentioned in Chapter 2, reflection phase characteristics of a flat HIS can be obtained by simulating a single unit cell because of its periodic geometry. However, this approach cannot be utilized for a FHIS which has an arbitrary shape. For instance, when the surface is curved in the form of a cylinder, either the surface geometry or the incident field is aperiodic, depending on the selection of the coordinate system. This means that a Floquet expansion of the fields cannot be done and periodic boundary conditions cannot be used. Hence, for such a problem, the entire surface should be modeled and simulated, which can be computationally intractable because of the large electrical dimensions of the problem.

To increase the computational efficiency of the problem, a semi-infinite model is utilized for the simulation. Assuming that the FHIS is long enough, periodic boundary conditions can be used along its axis. For normal incidence, the periodic boundary conditions can be represented by electrical and magnetic symmetry planes for TM^z and TE^z polarizations, respectively. Fig. 3.4 illustrates the HFSS [32] model, for TM^z incidence, of a curved FHIS with 10 cells in the circumferential direction. Since the geometry is also symmetric with respect to the axis of the cylinder, only one half of it is modeled. This numerical model significantly decreases the problem size.

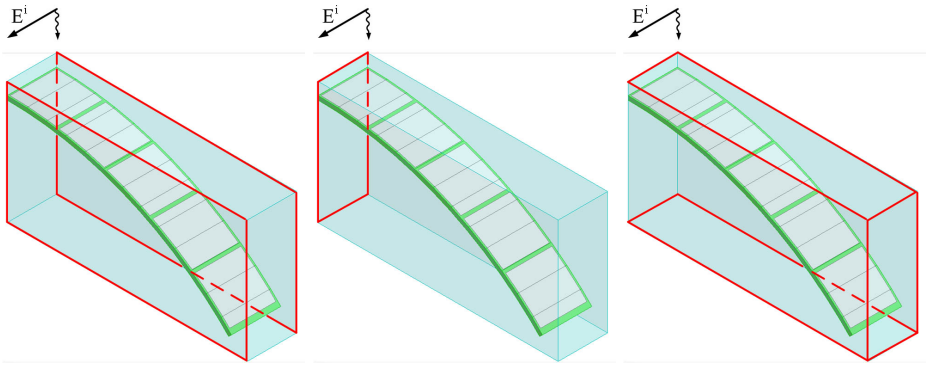

Fig. 3.4. Simulation model of the semi-infinite curved FHIS with 10 cells in the circumferential direction. The outlined planes are assigned the same boundary condition (BC).(a) Electrical symmetry BC. (b) Magnetic symmetry BC. (c) PML BC.

3.3. Analytical Model

Although the problem size can be drastically decreased by the utilized numerical model, it is still large compared to a unit cell simulation. Hence, an approximate analytical model, which gives sufficiently acceptable results, is of great interest.

Reflection phase of a structure is defined as the phase of the reflection coefficient referenced to its surface. Hence, by definition, the reflection phase characteristics of a surface is attained under plane wave incidence. For this problem, i.e., when the source is sufficiently far from the surface, a flat HIS can be modeled by an impedance boundary condition [25]. In other words, the surface can be replaced by an equivalent impedance and the reflection phase of the HIS can be calculated by solving the scattering problem from an infinite impedance sheet. The equivalent impedance can be obtained either by an analytical model [9], [29], [30], as stated in Chapter 2, or can be extracted from a full-wave solution.

When the HIS is curved in the form of a cylinder, as shown in Fig. 3.5(a), the problem becomes somewhat complicated. However, the surface impedance of the flat HIS can be in-

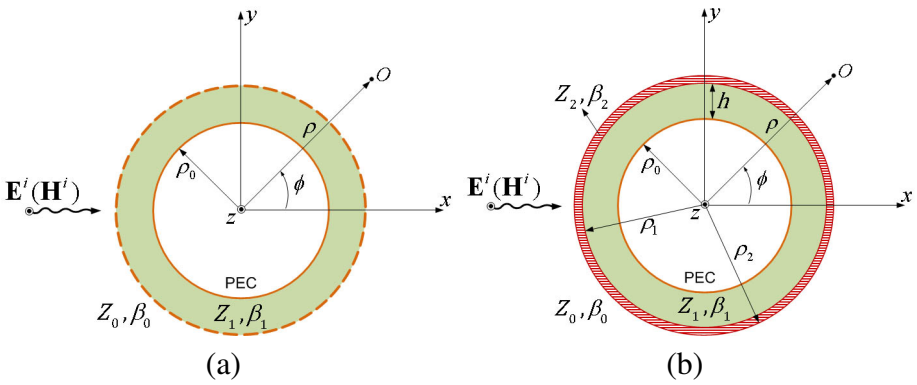

Fig. 3.5. Two dimensional (2-D) geometry of the problem. (a) Actual geometry. (b) Proposed model.

corporated into a modal solution to calculate the scattered fields. To do this, first, the FHIS is modeled as an infinitely long cylindrical sheet, and the problem is approximated by a 2-D canonical model in cylindrical coordinates. This geometry is very similar to the simulation setup with the periodic boundary conditions, which is discussed in the previous section. As displayed in Fig. 3.5(b), the frequency selective surface (FSS) layer of the HIS is represented by a very thin material whose thickness is chosen as the actual thickness of the metal as stated in [30]. The propagation constant and characteristic impedance of this equivalent material are β_2 and Z_2, respectively.

The flat FSS layer, which is a periodic array of metallic patches, can be represented by a shunt admittance. Hence, the characteristic impedance of the material can be expressed in terms of the admittance of the layer. This can be achieved by utilizing the *ABCD* matrix representation. Fig. 3.6 illustrates the relation between the *ABCD* matrix representations of a transmission line of length l and a shunt admittance. If the length of the transmission line is chosen infinitesimally short, the shunt admittance can be modeled as a transmission line or

vice versa. The characteristic impedance of the material can be expressed by (3.1), in terms of the admittance and the propagation constant β_2 of the layer.

$$Z_2 = \frac{j}{Y}\sin\beta_2 l \tag{3.1}$$

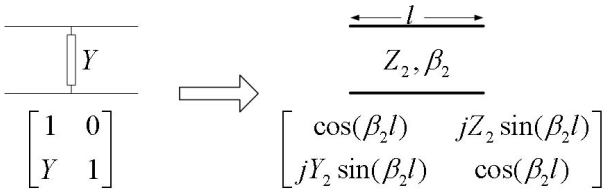

Fig. 3.6. *ABCD* matrix representations of a shunt admittance and a transmission line.

The next step is the determination of the propagation constant which is the most critical part of the problem. For the flat or nearly flat cases, β_2 can be assumed to be equal to β_1, which is the propagation constant of the dielectric layer. If the dielectric layer is lossless, then β_2 should be purely real. For large radii of curvature, this assumption gives sufficiently good results. However, as the radius of curvature decreases, the real propagation constant should be replaced with the complex one (γ_2), which changes as a function of the curvature. Indeed, the imaginary part of γ_2 is closely related to the curvature dependent surface impedance of the curved, periodic surface reported in [33], where the Leontovich boundary condition was utilized to solve the same problem. The propagation constant is expressed in (4.7), where β_0 is the free-space wave number and ρ is the radius of curvature.

$$\beta_2 = -j\gamma_2 = \beta_1(1 - j2\beta_0\sqrt{\varepsilon_1}\rho) \tag{3.2}$$

After all the necessary electrical parameters are obtained, the problem reduces to a plane wave scattering from a multilayer cylinder. The solution of this problem is straightforward

but tedious. The incident field, which is a plane wave propagating in the $+x$ direction, can be expressed as a summation of Bessel functions of the first kind as expressed in (3.3) [1]. In this formulation, a $e^{j\omega t}$ time dependence is assumed and suppressed.

$$\mathbf{E}^i(\mathbf{H}^i) = \hat{a}_z E_0(H_0) \sum_{n=-\infty}^{+\infty} j^{-n} J_n(\beta_0 \rho) e^{jn\phi} \tag{3.3}$$

For the 2-D scattering problem illustrated in Fig. 3.5, the scattered fields from a curved and infinitely long cylinder can also be written as in (3.4), where $H_n^{(2)}$ is the Hankel function of the second kind of order n. **E(H)** represents the electric(magnetic) field for TM^z(TE^z) polarization.

$$\mathbf{E}^s(\mathbf{H}^s) = \hat{a}_z E_0(H_0) \sum_{n=-\infty}^{+\infty} a_n H_n^{(2)}(\beta_0 \rho) e^{jn\phi} \tag{3.4}$$

The coefficient a_n can easily be obtained, as stated in (3.5) and (3.6), by solving the boundary conditions on the boundaries $\rho = \rho_0$, ρ_1 and ρ_2. Therefore, the scattered fields can be expressed in terms of the characteristic impedance (Z_2) and the propagation constant (β_2) of the equivalent layer which represents the FSS layer. The admittance of the FSS layer can be calculated analytically or can be extracted from a full-wave solution of a single unit cell or from measured data. Once the scattered fields are obtained, it is straightforward to obtain the reflection phase of the curved surface. In these expressions, the *"prime"* operator indicates derivative with respect to the argument.

$$a_n^{TM} = j^{-n} \frac{Z_2 J_n'(\beta_0\rho_2) C_n(\beta_2\rho_2) - Z_0 J_n(\beta_0\rho_2) C_n'(\beta_2\rho_2)}{Z_0 C_n'(\beta_2\rho_2) H_n^{(2)}(\beta_0\rho_2) - Z_2 C_n(\beta_2\rho_2) H_n^{(2)'}(\beta_0\rho_2)} \tag{3.5}$$

$$a_n^{TE} = j^{-n} \frac{Z_2 J_n(\beta_0\rho_2) C_n'(\beta_2\rho_2) - Z_0 J_n'(\beta_0\rho_2) C_n(\beta_2\rho_2)}{Z_0 C_n(\beta_2\rho_2) H_n^{(2)'}(\beta_0\rho_2) - Z_2 C_n'(\beta_2\rho_2) H_n^{(2)}(\beta_0\rho_2)} \tag{3.6}$$

$$C_n(\beta\rho) = \frac{B_n D_n(\beta\rho) + A_n(\beta_1\rho_1)Y_n(\beta\rho)}{Y_n(\beta_2\rho_1)} \tag{3.7}$$

$$D_n(\beta\rho) = J_n(\beta\rho)Y_n(\beta_2\rho_1) - J_n(\beta_2\rho_1)Y_n(\beta\rho) \tag{3.8}$$

$$B_n = \frac{-\pi\beta_2\rho_1}{2Z_1}(Z_2 A_n'(\beta_1\rho_1)Y_n(\beta_2\rho_1) - Z_1 A_n(\beta_1\rho_1)Y_n'(\beta_2\rho_1)) \tag{3.9}$$

$$A_n^{TM}(\beta\rho) = \frac{J_n(\beta\rho)Y_n(\beta_1\rho_0) - J_n(\beta_1\rho_0)Y_n(\beta\rho)}{Y_n(\beta_1\rho_0)} \tag{3.10}$$

$$A_n^{TE}(\beta\rho) = \frac{J_n(\beta\rho)Y_n'(\beta_1\rho_0) - J_n'(\beta_1\rho_0)Y_n(\beta\rho)}{Y_n'(\beta_1\rho_0)} \tag{3.11}$$

The reflection phase of a HIS is defined as the phase of the reflected field in the back scattering direction and calculated on the surface [22]. Hence, the scattered fields should be calculated at $\rho = \rho_2$ and $\phi = 180^\circ$. The infinite series given in (3.3) and (3.4) converges very rapidly by using a small number of terms.

Before moving to the verification of the analytical method and the interpretation of the results, it may be useful to make a qualitative analysis of the problem and comment on the expected results. Undoubtedly, for PEC and PMC surfaces, the phase of the scattered field on the surface is independent of the curvature. Therefore, we expect the PEC and PMC limits of a curved HIS would occur at the same frequencies as when it is flat. However, the behavior for the intermediate impedance values is not easy to predict without a quantitative analysis.

Fig. 3.7 shows the geometry and the comparison of the reflection phase curves of the flat and curved HIS for TM^z polarization. The FHIS is comprised of an array of square patches of

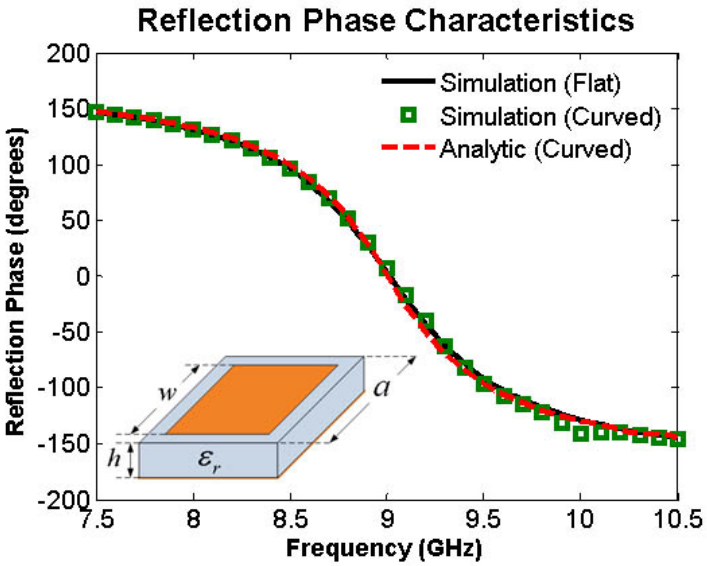

Fig. 3.7. Comparison of the reflection phases of the flat and curved HIS. The HIS is comprised of an array of square patches of width (w) 7.5 mm and period (a) of 8.0 mm. The substrate has a thickness of 0.635 mm and a relative permittivity of 3.5.

width 7.5 mm and separation between them of 0.5 mm. The substrate has thickness of 0.635 mm, relative permittivity of 3.5, and radius of curvature of 50 mm. For the simulations, a semi-infinite model with 8 cells in the circumferential direction has been utilized. As expected, the zero crossing of the FHIS does not change with the curvature. Moreover, the reflection phase of the flat and curved HISs are basically identical within the entire band and there is an excellent agreement between the simulations and the analytical results.

Fig. 3.8 shows the simulation geometry and the comparison of the simulated reflection phases of the HIS given in Fig. 3.7, for the flat and curved cases, under TM^z incidence. Similar to the analytical results, the reflection phase of the curved HIS is very close to that of the flat one. Hence, we can conclude that the reflection phase is independent of the radius of curvature. A similar behavior can also be obtained for the TE^z polarization.

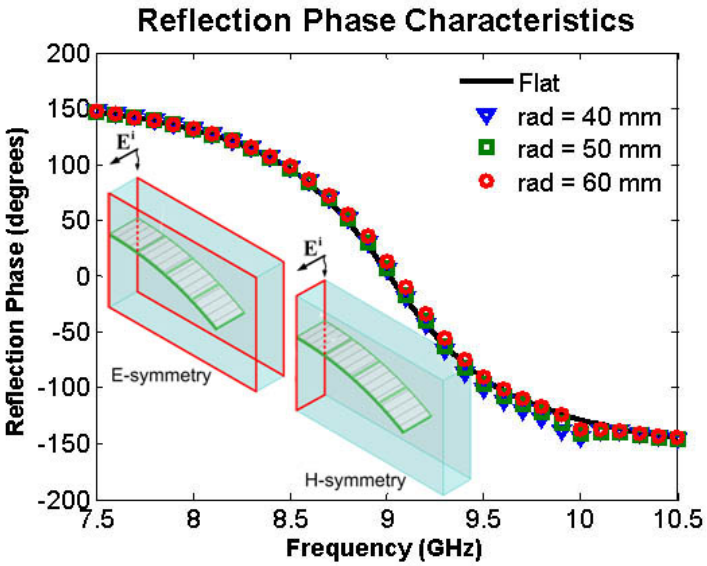

Fig. 3.8. Comparison of the simulated reflection phases of the square HIS for different curvatures.

3.4. Numerical Results

The analytical formulation is not based on a particular type of patch i.e., these results are general and should be valid for any type of HIS, regardless of the shape of the conducting patches. To verify this, similar simulations are repeated for a HIS comprised of strip gratings and dog-bone shaped patches as shown in Figs. 3.9 and 3.10, respectively. The HIS comprised of strip gratings is a complete cylinder while the dog-bone HIS has 11 cells in the circumferential direction. Expectedly, the reflection phase curves for TM^z polarization are almost identical for all curvatures.

The HIS comprised of strip gratings is a complete cylinder while the dog-bone HIS has 11 cells in the circumferential direction. Expectedly, for all of the examples that have been discussed so far, the reflection phase curves, for TM^z polarization, are almost identical for all curvatures.

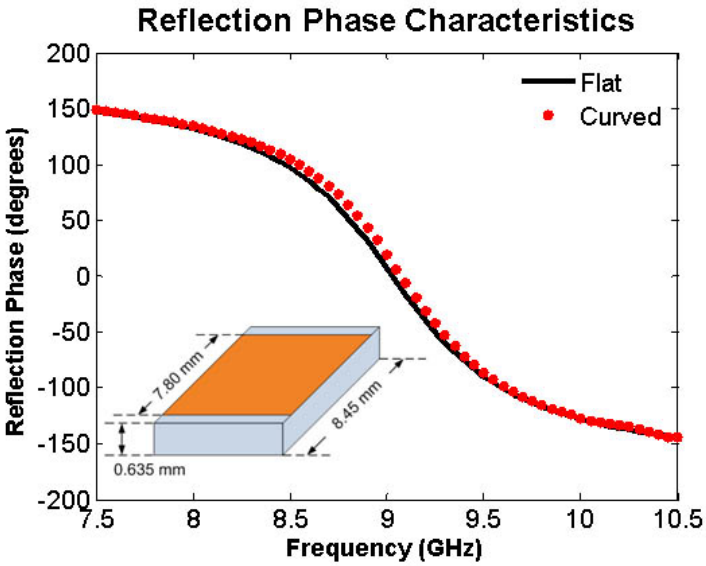

Fig. 3.9. Comparison of the simulated reflection phases of the flat and curved HIS comprised of strip gratings. The radius of curvature is 53.16 mm.

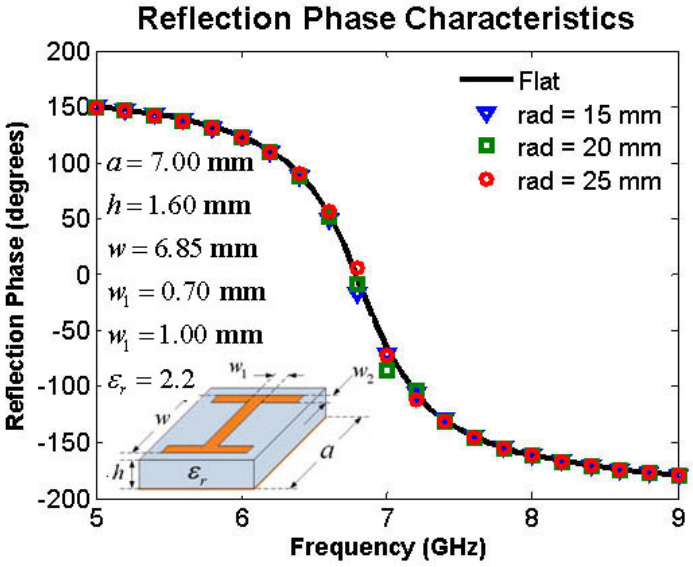

Fig. 3.10. Comparison of the simulated reflection phases of the dog-bone shaped HIS for different curvatures.

All of the examples that have been discussed so far are in agreement and verify the claim that reflection phase of an HIS is independent of curvature. However, this is not always the case. For instance, Fig. 3.11 shows that the reflection phase response of a curved HIS which

is comprised of an array of square patches with a width of 7.9 mm and the separation between them is 0.5 mm. The substrate is 25 mil-thick polyimide with a dielectric constant of 3.3 and the radius of curvature is 50 mm. It is clear that, although we obtain expected results for the surface with 6 cells, the reflection phase of the surface with 14 cells follows that of the surface with 6 cells up to 9.5 GHz. After this frequency, it deviates from the expected curve and converges back at around 10 GHz. Obviously, this not only contradicts the claim that reflection phase is independent of curvature, but also indicates that it changes as a function of HIS size. Indeed, surface waves generated on HISs can have a significant impact on their reflection phase characteristics. Excitation mechanism of the surface waves and their effects on current distribution and reflection phase will be discussed in the section that follows.

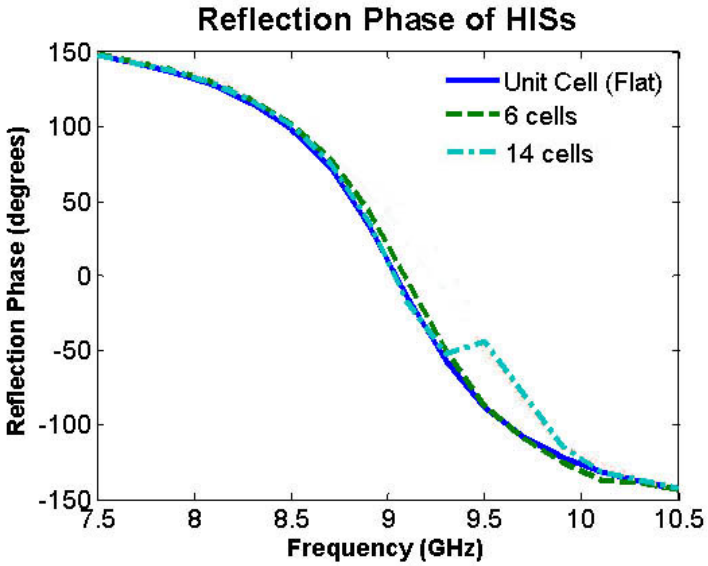

Fig. 3.11. Comparison of the reflection phase of the curved FHIS for different number of cells in the circumferential direction.

3.5. Surface Wave Effects

For a thorough and convincing explanation of the unanticipated results, the currents generated on these surfaces should be examined in detail. This will enable the reader to completely understand the effects of surface waves on the reflection phase characteristics of HISs. Since HISs are periodically arranged arrays of metallic patches loaded with a grounded dielectric, it is prudent to first examine the types of currents generated on a finite periodic array. These are *Floquet currents, array guided surface waves (AGSWs)* and *end currents* [2]. The *Floquet currents*, which are uniformly distributed, are generated on an infinite periodic structure and are in phase with the incoming wave. The *AGSWs* are currents which are observed only on finite periodic structures and within certain frequency bands; nonuniform currents observed on periodic structures are of this type. These currents are different than surface waves supported by a grounded dielectric. They can exist even in the absence of a ground plane. Finally, the *end currents* are due to the truncation of the Floquet currents and AGSWs.

3.5.1. *Excitation of AGSW*

A surface wave is a special type of electromagnetic wave which is tightly bound to the medium it is propagating in. The attenuation constant of surface waves, in the normal direction to the surface, is very large [1]. Therefore, it is not possible to excite surface waves on an infinite surface, for instance an air-dielectric interface, due to the mismatch between the phase of an incident plane wave and the phase of a surface wave. Therefore, for plane wave incidence, the AGSWs are only excited on a finite periodic structure. They can also be generated by localized sources, like an antenna, which will be examined in Chapter 4.

Although the excitation of these currents are detailed in [34], [35], it will be briefly repeated here for completeness. Fig. 3.12 shows the generation mechanism of AGSWs. A finite periodic structure can be modeled as a combination of an infinite periodic array with two semi-infinite arrays. The current distribution on the infinite array is identical to the currents on the finite array. However, the currents on the semi-infinite arrays are exactly opposite. The infinite array generates the Floquet currents. The semi-infinite arrays launch two waves, one traveling to the right and the other to the left. These are the array guided surface waves. These waves are consecutively reflected at the edges of the semi-infinite arrays and contribute to the edge currents [34].

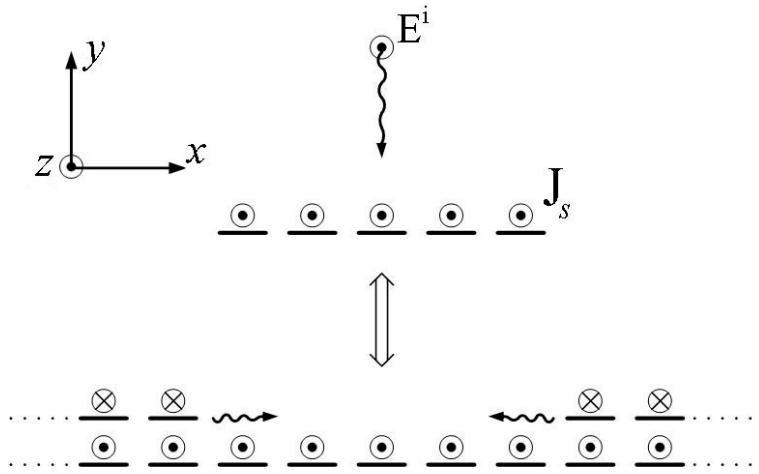

Fig. 3.12. Generation of array guided surface waves on a finite periodic array.

AGSWs are generated only within certain frequency intervals where the scan impedance of the array is zero [34]. For passive periodic structures, this is equivalent to the frequency interval where the determinant of the impedance matrix of the array is zero [36]. These frequencies are simply the eigenvalues of the periodic structure and, hence, the surface wave modes are

the eigenmodes. For HISs, these frequencies can easily be seen with the aid of the dispersion diagram.

Fig. 3.13 shows the simulated dispersion diagram of the fabricated FHIS of Fig. 3.3. The first order surface wave mode excited on an HIS is the TM mode. This mode is attributed to the grounded dielectric substrate, and it does not have a cutoff frequency [1]. On the other hand, the second order surface wave mode is the TE mode. The cutoff frequency of the TE_1 mode surface wave of the FHIS is around 10 GHz. However, the TE_1 mode of the grounded dielectric, with the identical permittivity and thickness, has a cutoff frequency of 77.86 GHz. Thus, the relatively lower cutoff frequency of the TE mode surface wave of the HIS is due to the periodic arrangement of the patches on the top layer of the HIS. Indeed, AGSWs generated on finite periodic structures and TE surface waves generated on a HIS are highly related. As it can be seen from Fig. 3.13, in the ΓX region, the onset of the TE surface waves is slightly higher than 9 GHz and the cutoff is just above 10 GHz. Within this frequency interval, the surface waves have significant impacts on the current distribution on the patches and the reflection phase of the FHIS.

3.5.2. *Current Distribution*

Since the surface wave modes are the eigenmodes of the periodic structure, they can be observed on any type of periodic surface. The frequency range where AGSWs are generated does not depend on the curvature of the surface but rather on its geometric arrangement. Therefore, one should be able to observe their effects regardless of curvature.

Figs. 3.14 and 3.15 display the surface currents on the flat HIS of Fig. 3.11, with different cell numbers, at different frequencies. Due to the symmetry of the structure, only one half of

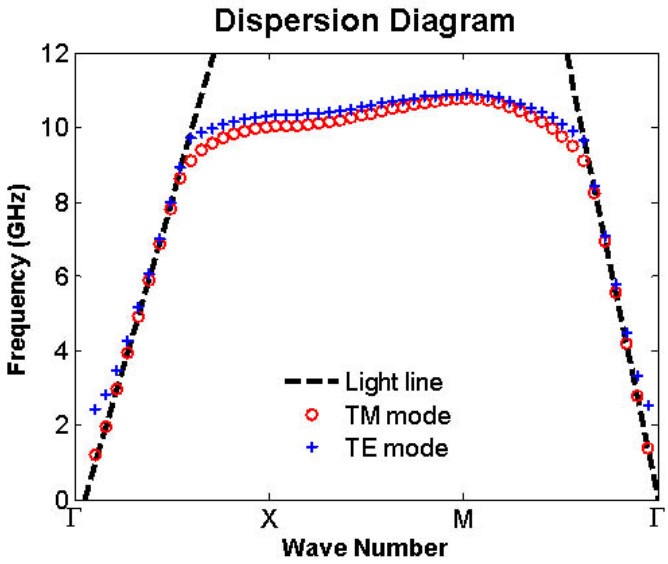

Fig. 3.13. Dispersion diagram of the HIS obtained by full-wave simulation.

the surfaces are shown. Clearly, at 8.9 GHz, the surface currents are almost uniformly distributed, and they are in phase with the incoming wave. Those are the Floquet currents. The effects of the end currents are almost negligible at this frequency. However, at 9.9 GHz the distribution is noticeably nonuniform due to the AGSWs. It is also clear that the current distribution depends on the size of the surface. Because, the surface waves continuously reflected from the edges of the HIS create a standing wave pattern which is a function of the length of the HIS. On the other hand, the propagation constant of AGSW is not a function of the distance between the edges, but of the other geometric parameters [34].

Figs. 3.16 and 3.17 illustrate the surface current densities on the same HISs of Figs. 3.14 and 3.15 when they are curved in the form of a cylinder with a radius of 50 mm. Similarly, at 8.9 GHz, the currents are almost uniformly distributed, especially on the patches close to the center of the FHIS. The magnitudes of the currents are clearly decreased towards the edges because of the shedding of energy [2]. Therefore, the currents closer to the edges of the

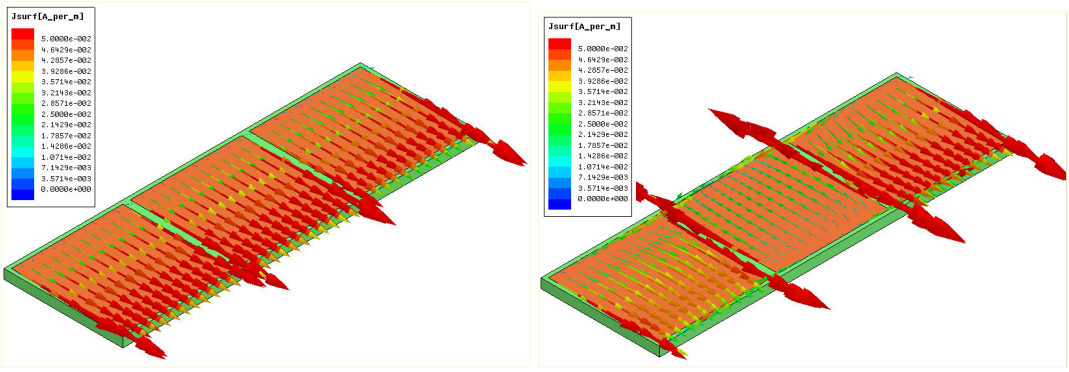

(a) (b)

Fig. 3.14. Surface current density of the flat FHIS, with 6 cells, at different frequencies. (a) 8.9 GHz. (b) 9.9 GHz.

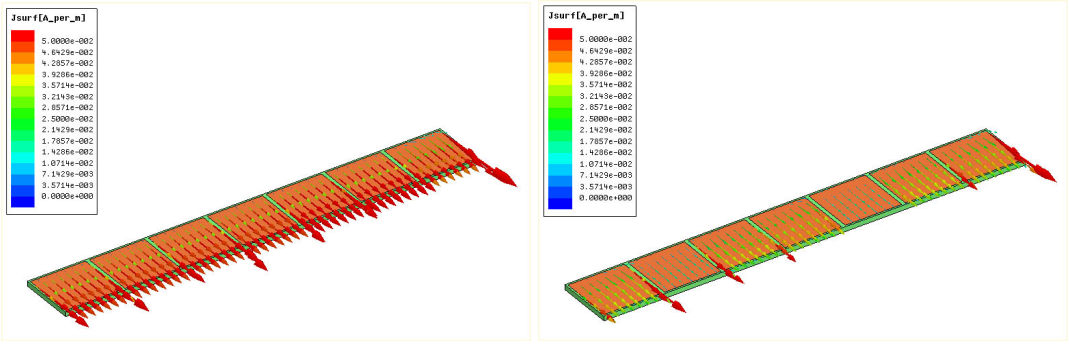

(a) (b)

Fig. 3.15. Surface current density of the flat FHIS, with 14 cells, at different frequencies. (a) 8.9 GHz. (b) 9.9 GHz.

surface have a less significant effect on the reflection characteristics. The shedding of energy becomes more pronounced as the size of the HIS increases. On the other hand, at 9.9 GHz, the currents are extremely nonuniform, even on the central patches. Similar to the flat case, the current distribution is a function of the length of the FHIS. It is also important to note that the frequency intervals in which the AGSWs propagate are almost identical for the flat and curved cases.

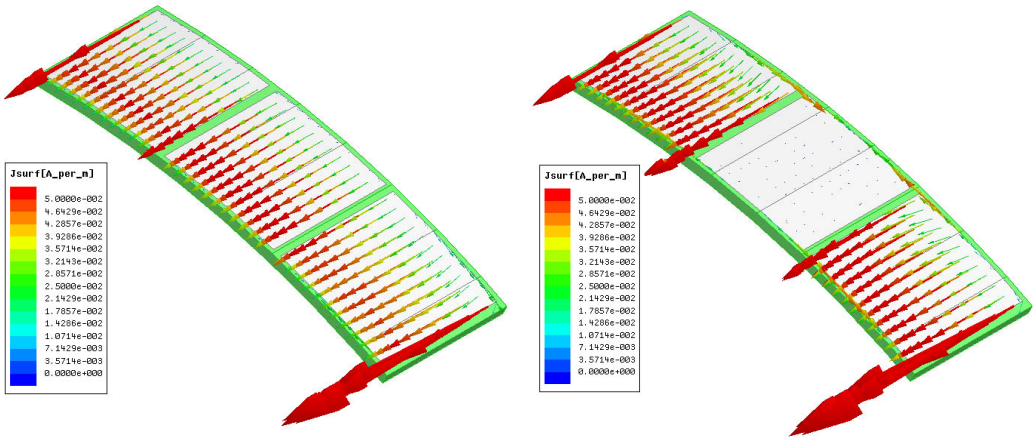

(a) (b)

Fig. 3.16. Surface current density of the curved FHIS, with 6 cells in the circumferential direction, at different frequencies. (a) 8.9 GHz. (b) 9.9 GHz.

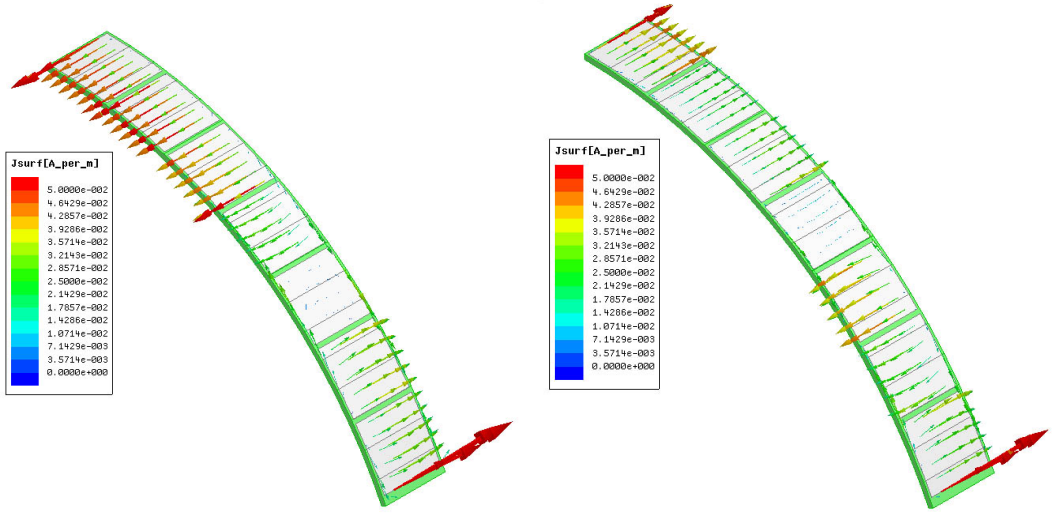

(a) (b)

Fig. 3.17. Surface current density of the curved FHIS, with 14 cells in the circumferential direction, at different frequencies. (a) 8.9 GHz. (b) 9.9 GHz.

At this point, a critical question may come to the mind of the reader. How is it so certain that those deviations are due to the AGSWs but not due to the end currents which are generated by the truncation of the Floquet currents? The very immediate answer to this question is the

fact that the non-uniform current distribution is observed only within certain frequency bands. Another answer can also be provided by examining the following example.

When the radius of curvature is decreased to 17.2 mm, the curved HIS with 14 cells forms a complete cylinder. Therefore, we should not expect strong end currents, which are mainly attributed to the truncation of the surface. However, as illustrated in Fig. 3.18, the surface currents are extremely non-uniform because AGSWs are still excited. Although there is not any discontinuity or truncation in the structure, the non-uniformities can still be observed. Clearly, these currents are not only due to the truncation of the ground plane but also because of its periodic structure.

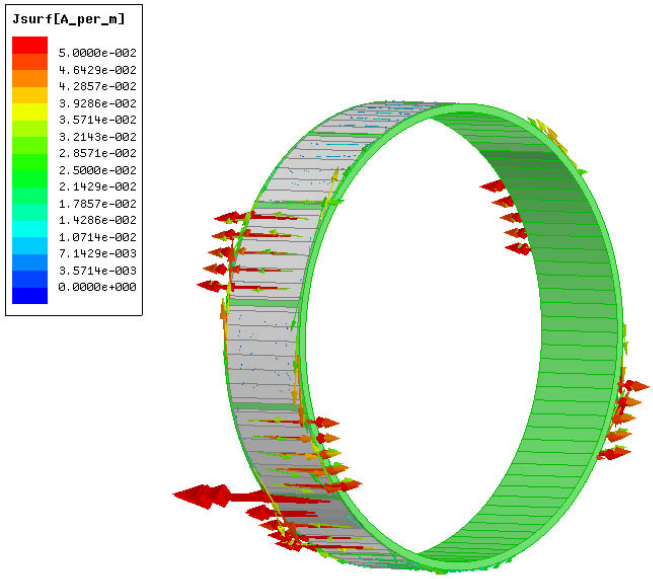

Fig. 3.18. Surface current density of the curved FHIS, with 14 cells in the circumferential direction, at 9.9 GHz. The radius of curvature is 17.2 mm.

The current distribution on the fabricated FHIS is also very similar. Fig. 3.19 exhibits the current distribution for three different frequencies on the flat HIS, which has the dispersion diagram displayed in Fig. 3.13. The HIS has 20 cells in the *y* direction and it is infinite in the

x direction. Only one half of the patches are shown due to the symmetry, with respect to the x-axis, of the surface. The currents on the other side are exactly identical. Also, the incident field is directed in the x direction.

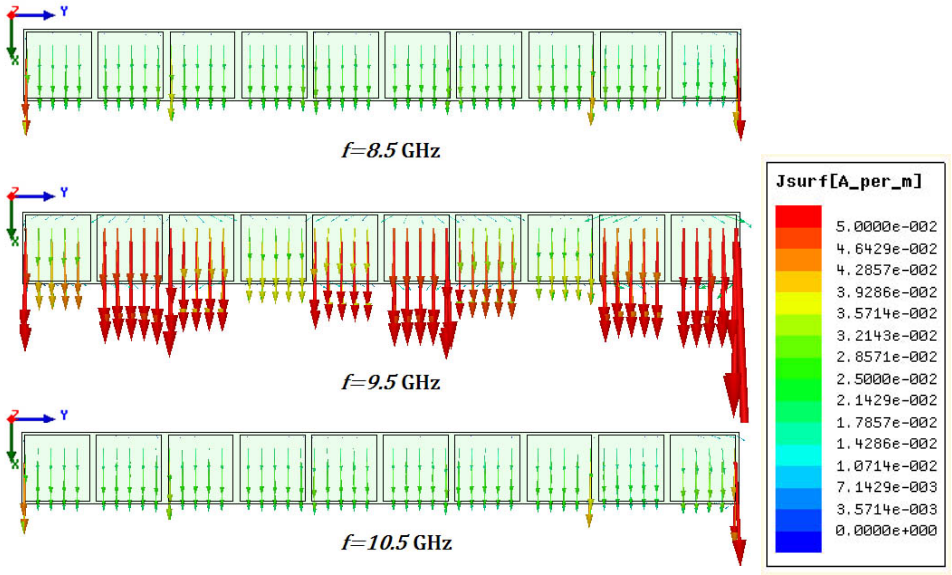

Fig. 3.19. Surface current distribution on the flat HIS at different frequencies.

As expected, at 8.5 and 10.5 GHz, the current distribution is almost uniform because the AGSWs are cutoff for these frequencies; only the Floquet currents are propagating. On the other hand, at 9.5 GHz, the currents are noticeably non-uniformly distributed, due to the excitation of surface waves. It is also apparent that the magnitudes of the currents are increased significantly. The current distribution of the curved HIS is quite similar and will not be repeated.

3.5.3. *Reflection Phase*

The homogenized model, which was used as the basis of the analytical approach, was obtained from the full-wave simulation of the infinite surface. On the other hand, it was stated

that AGSWs can only be excited on finite periodic structures. Therefore, the analytical model cannot be used to investigate the impacts of AGSWs on reflection phase characteristics. For the remaining parts of this chapter, full-wave simulations were utilized.

For the reflection phase simulations, the flat case is considered first. Despite the dependence of surface current distribution on frequency, the reflection phase of the HIS is basically not affected by the changes in the current distribution, as illustrated in Fig. 3.20. The reflection phase characteristics of the semi-infinite HISs of Figs. 3.14 and 3.15, and the infinite HIS are practically identical. Although the current distributions on the flat HISs are significantly impacted by the surface waves, the reflection phases are not distorted. This is attributed to the radiation resistance of the surface waves.

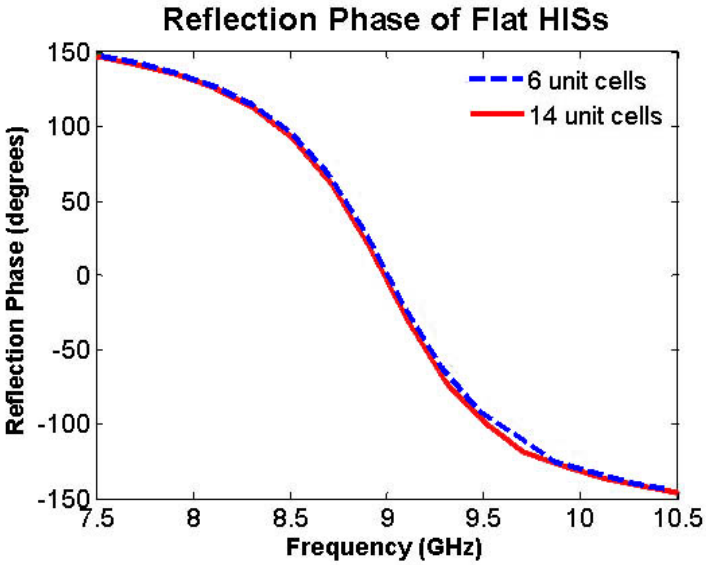

Fig. 3.20. Comparison of the reflection phase of the flat FHIS for different number of cells.

The radiation resistance associated with the AGSWs is much smaller than that of Floquet waves [2]. Therefore, they can only change the scattering pattern of the surface when the observation point is away from the specular reflection direction. For the flat case, the backscat-

tering direction coincides with the specular reflection direction; hence we do not observe the effects of the AGSWs. However, when the surface is curved, the backscattering and specular reflection directions are different which causes distortions in the reflection phase diagrams. For a fixed size of the HIS, the effects of the AGSWs become more evident as the radius of curvature decreases.

The reflection phase of the curved FHIS with 14 cells, for a TM polarized incident wave, is shown in Fig. 3.21, for different curvatures. Expectedly, the reflection phase changes as a function of the curvature. As a matter of fact, for all curvatures, the reflection phase diagram deviates from that of the flat HIS after 9 GHz and converges back around 10.1 GHz. Because at 10 GHz, the guided wavelength is approximately 16 mm. That is, the distance between the patches (periodicity) is approximately half wavelength. At higher frequencies, the distance gets even larger and there is always a Floquet mode propagating. Hence, the effects of AGSWs are not observed [34].

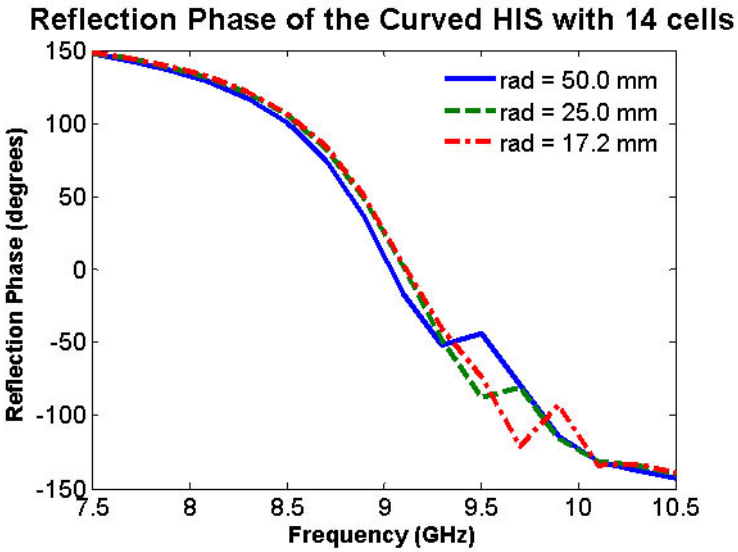

Fig. 3.21. Comparison of the reflection phases of the curved FHIS, with 14 cells in the circumferential direction, for different curvatures.

Up to this point, the simulations verify that there is a parallelism between the surface current distribution and reflection phase characteristics. Hence, recalling Fig. 3.11, one should expect similar current patterns for the curved surface with 6 cells within the entire frequency band since the reflection phase of this surface is very close to that of the flat case. However, Fig. 3.16 shows that the current distributions at 8.9 GHz and 9.9 GHz are completely different. Indeed, this is due to the curvature of the surface. When the radius of curvature is 50 mm, the HIS with 6 cells is almost planar. Thus, the effects of the AGSWs cannot be observed properly.

The effects of the curvature can be observed more prominently for the HIS with 6 cells if the radius is decreased. The reflection phases of this HIS, for different curvatures, are compared in Fig. 3.22. Although the reflection phase of the curved HIS, with a radius of curvature of 50 mm, is almost identical to that of the flat HIS, the reflection phase is significantly distorted if the radius of curvature is decreased to 17.2 mm.

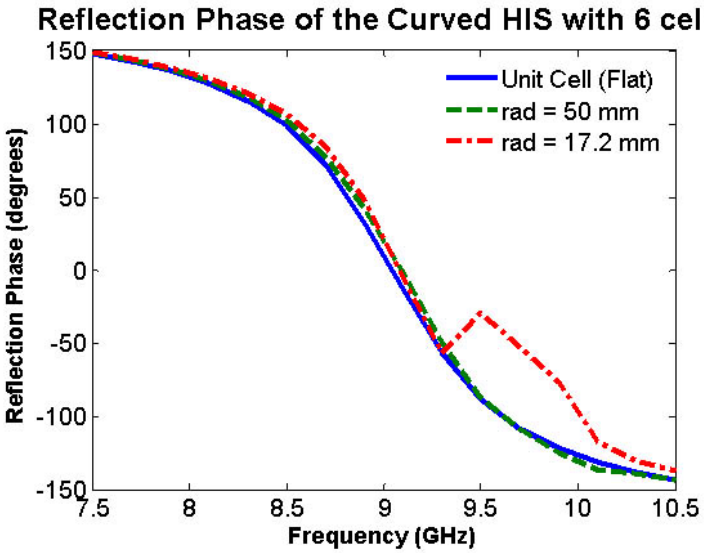

Fig. 3.22. Comparison of the reflection phases of the curved FHIS, with 6 cells in the circumferential direction, for different curvatures.

A similar behavior was obtained for the fabricated FHIS, as well. Fig. 3.23 shows the reflection phase of the fabricated FHIS for three different radii of curvature. The incident wave is TM polarized and the FHIS has 16 cells in the circumferential direction. Obviously, the reflection phase changes as a function of radius. Between 9 and 10 GHz, the reflection phase of the curved HIS deviates from that of the flat one, and around 10 GHz it starts to converge back since the surface waves are cutoff.

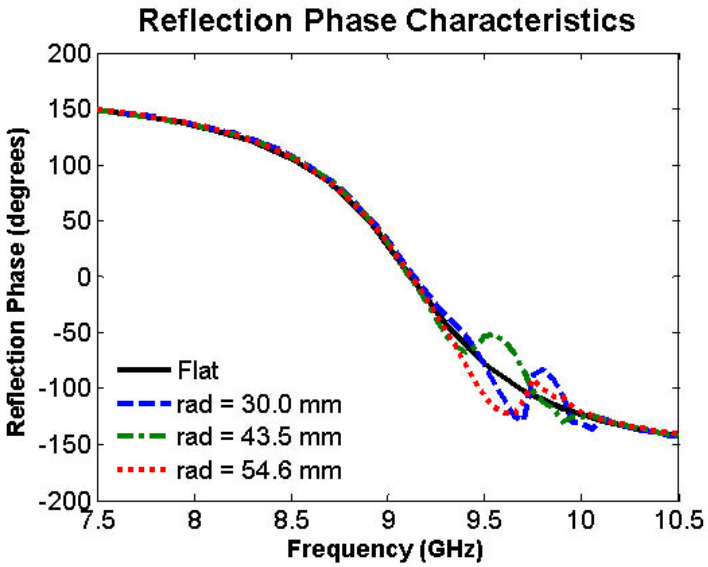

Fig. 3.23. Simulated reflection phase of the curved HIS for different curvatures. The HIS has 16 cells in the circumferential direction. The incident wave is TM polarized.

As discussed previously, the surface waves generated on the HIS are consecutively reflected at the edges of semi-infinite arrays contributing to the edge currents. Due to those reflections, a standing wave pattern is generated on the HIS which depends on its size; hence the reflection phase of a curved HIS is a function of the number of cells. For instance, for a large radius of curvature, the effects of the AGSWs become more noticeable as the size of the

surface increases. For a small number of cells, the distortions are not observed, as shown in Figs. 3.8 and 3.11.

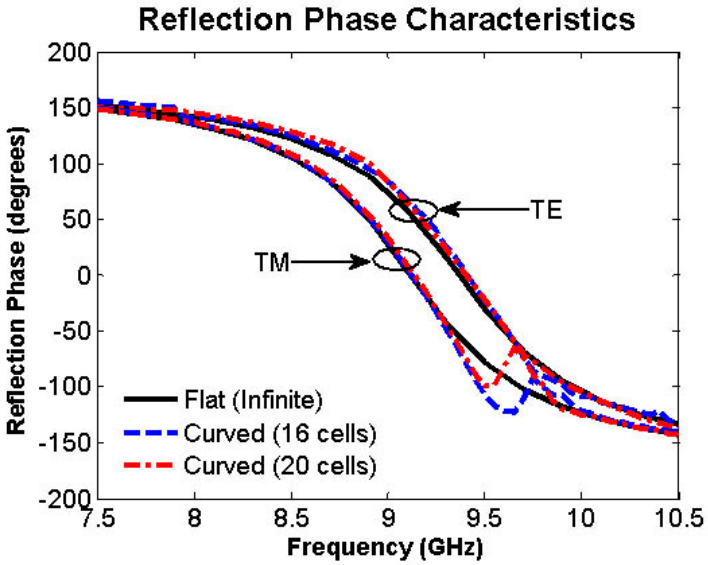

Fig. 3.24. Simulated reflection phase of the curved HIS for different surface sizes. The radius of curvature is 54.6 mm.

The reflection phase of the fabricated FHIS, for different numbers of cells, is illustrated in Fig. 3.24. For both cases, the radius of curvature is maintained constant at 54.6 mm. As expected, the reflection phase changes as a function of surface size. Apparently, for TM polarization, the effects of the surface waves are more dramatic. However, for the TE polarized incident field, both the simulated and measured reflection phase responses of the curved FHIS are almost identical with those of the flat. Since TE polarized incident fields cannot excite TE surface waves, the reflection phase for this polarization is barely distorted.

3.6. Suppression of Surface Waves

It is verified that AGSW may have significant and undesirable effects, which result in deviations from the predicted reflection phase characteristics. So, the next question is: “Is there

a way to control or suppress the propagation of AGSWs?". In [2], a resistive loading was suggested on some of the elements of the periodic structure such that they form a barrier for surface currents. When a tapered resistive loading is applied to the elements towards the edges of a phased array of dipoles, very successful results can be attained [2], [37]. The same concepts can be applied to HISs, as well. For this purpose, as illustrated in Fig. 3.25, the last 12 elements (the elements on the nonilluminated side of the cylinder) are loaded with a tapered resistance such that the surface impedance of the patches changes from 0.5 Ω/□ to 5.0 Ω/□; the remaining 24 elements are kept unloaded. Since the surface is symmetric, only one half of the cylinder is shown. The dashed line and the arrow indicate the symmetry axis and incidence direction, respectively. It is obvious that, when the patches are loaded, the AGSWs are suppressed and the ripples in the reflection phase diagram are removed significantly. However, there is a shift in the center frequency due to the changes in the surface impedance of the HIS.

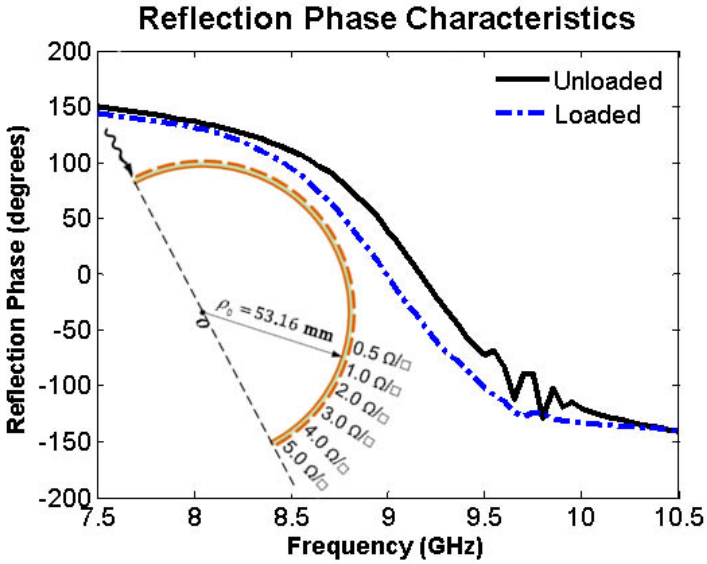

Fig. 3.25. Comparison of the reflection phase curves of the loaded and unloaded FHIS.

It has already been mentioned that the surface waves are still generated, even when the size of the FHIS is equal to the circumference of the cylinder. Interestingly, although the radius of curvature and the patch dimension in the axial direction of the FHIS of Fig. 3.25 and the HIS of Fig. 3.9 are identical, the reflection phase of the strip gratings is not distorted. This is attributed to the non-periodic geometry of the strip gratings in the circumferential direction; AGSWs cannot be generated.

3.7. Measurements

The measurements were performed at the ElectroMagnetic Anechoic Chamber (EMAC) at Arizona State University (ASU). The reflection phase was obtained by measuring the free-space, broadside RCS [22] of the FHIS, which was taped to a curved plastic fixture. This fixture acted as a reference down-range location against which the front surface of the FHIS and the reference plate could be repeatably placed. The fixture was mounted on the top of an expanded polystyrene column.

In order to orient the fixture for broadside illumination, a small piece of mirror was attached to the surface of the reference plate that was installed in the fixture. From the location of the feed horns, a laser beam was bounced off of the small mirror. The orientation of the fixture and support column was adjusted until the reflected laser beam returned to its point of origin. The measurement setup is illustrated in Fig. 3.26.

An HP8510C Vector Network Analyzer was used as the instrumentation at the EMAC facility. The measured data was acquired at 801 frequency points between 7.5 and 12.0 GHz. A synthesized source was operated in step frequency mode, and an IF averaging factor of 2048 was used. Three scattering measurements, as a function of frequency, were collected: one of

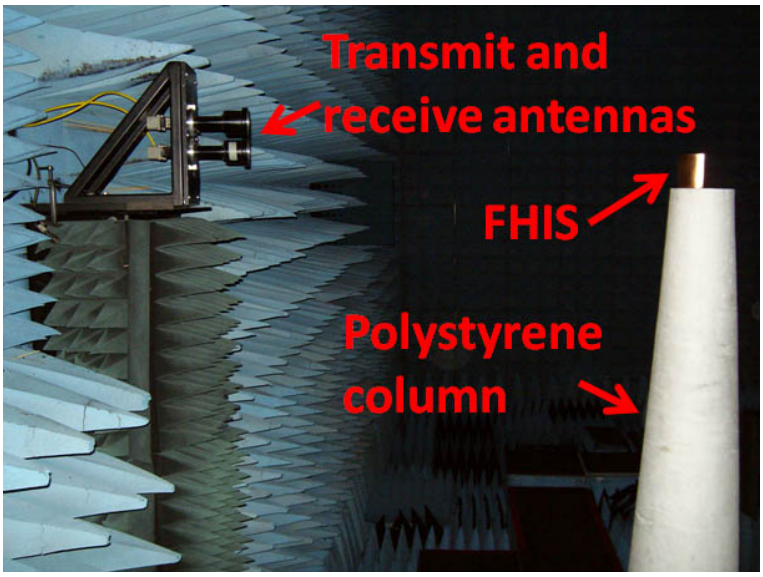

Fig. 3.26. The measurement setup.

the FHIS, one of the empty chamber, and one of curved copper plate. The scattering of the empty chamber was subtracted from both the plate and the FHIS measurements. The resulting measurements were then time-domain gated to remove the effects of feed horn coupling and scattering from the compact antenna test range reflector. Finally, the FHIS measurements were normalized by the curved plate measurements.

Fig. 3.27 displays the comparison of the simulated and measured reflection phase diagrams of the curved FHIS, when the radius of curvature is 54.6 mm. The measured FHIS has 20 and 11 cells in the circumferential and axial directions, respectively.

Although, the effects of AGSWs can be observed both in simulations and measurements, there is a slight mismatch between the two for TE polarization. One reason for the mismatch can be the misalignment in the position of the fixture which may result in significant phase variations in X-band. Another reason could be the misalignment in the tilt angle which may cause cross coupled fields to be generated on the curved HIS. Indisputably, phase measure-

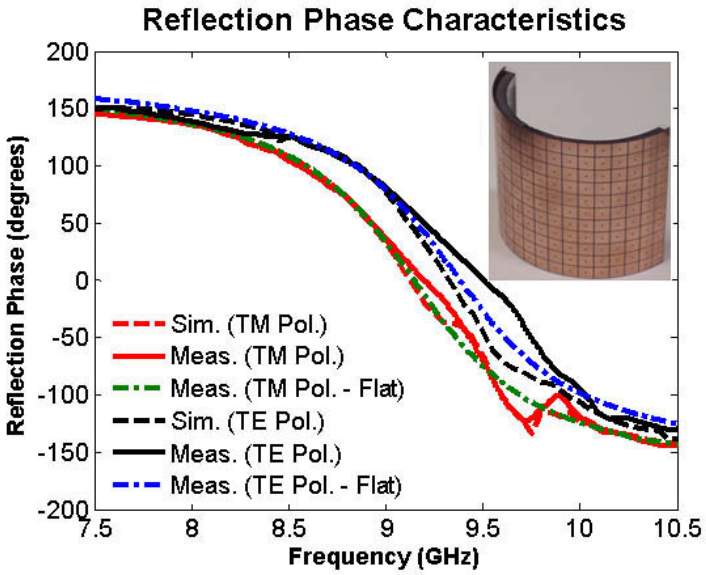

Fig. 3.27. Reflection phase of the curved HIS with 20 cells in the circumferential direction. Radius of curvature is 54.6 mm.

ments at high frequencies are extremely difficult to perform because of the sensitivity to minor alignment changes. It should also be noted that the tape, which was used to adhere the FHIS to the curved fixture to maintain the curved geometry, had significant effects on the reflection phase. Even though the thickness of the tape is very small (~ 0.07 mm), since it changes the surface impedance that AGSWs see, it changes the locations of the "bumps" observed on the reflection phase diagrams. According to the limited available data, the relative permittivity of the tape is approximately 2.5. A good agreement between simulations and measurements is attained when the loss tangent of the tape was adjusted to 0.2, which is assumed to be due to the highly lossy adhesive layer.

Similar results, illustrated in Figs. 3.28-3.30, are obtained for different curvatures and HIS sizes. Clearly, for all cases, there is a good agreement between simulations and measurements. It is verified that the reflection phase of the curved FHIS is considerably distorted within

the frequency band in which surface waves are generated. As expected, the reflection phase changes as a function of curvature and HIS size, concurring with the theory.

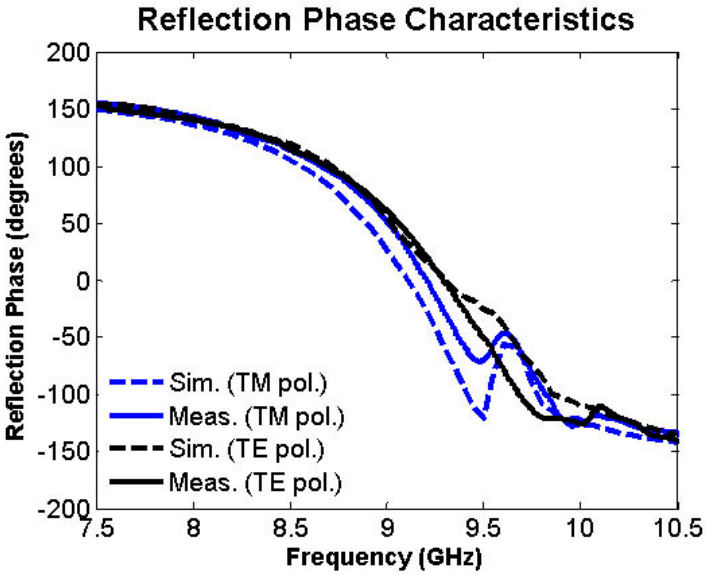

Fig. 3.28. Reflection phase of the curved HIS with 20 cells in the circumferential direction. Radius of curvature is 43.5 mm.

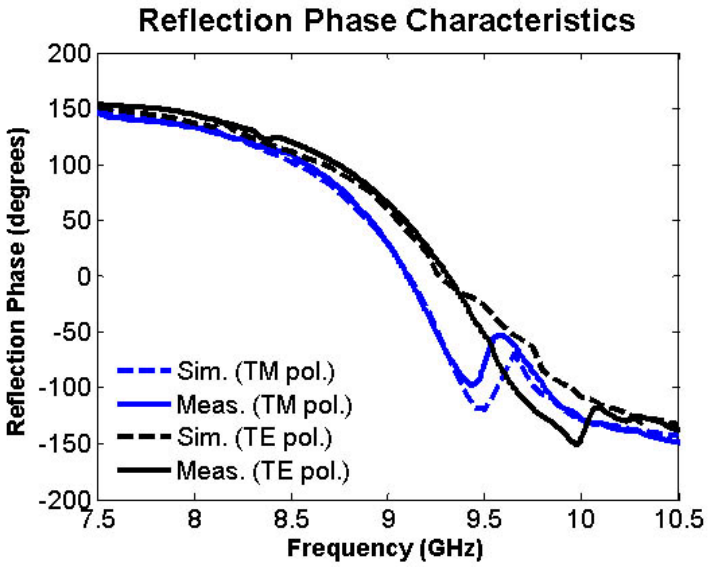

Fig. 3.29. Reflection phase of the curved HIS with 18 cells in the circumferential direction. Radius of curvature is 54.6 mm.

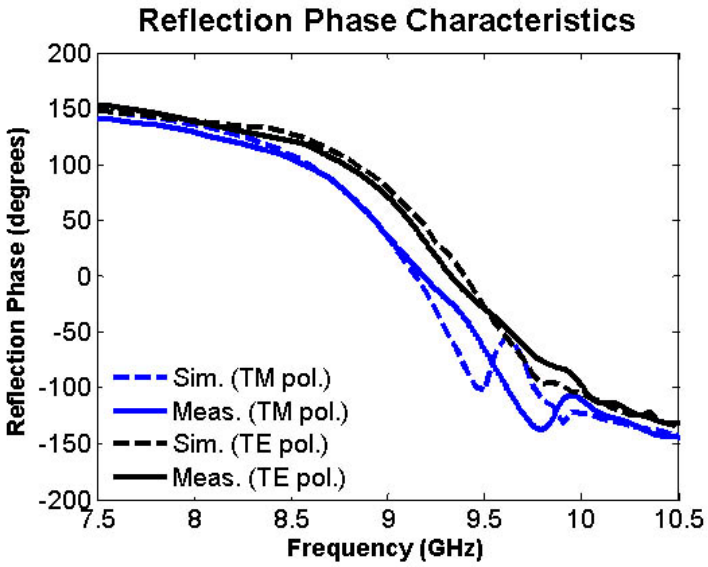

Fig. 3.30. Reflection phase of the curved HIS with 18 cells in the circumferential direction. Radius of curvature is 43.5 mm.

CHAPTER 4

ANTENNA APPLICATIONS OF FLEXIBLE HIGH IMPEDANCE SURFACES

In Chapter 3, the reflection phase characteristics of curved HISs were discussed. However, this chapter focuses on the performance of curved HISs in the presence of a localized source, particulary a dipole antenna. The relation between the reflection phase characteristics and the return loss of an antenna located above an HIS is examined. To accomplish this, a new bandwidth definition is introduced and contrasted with the AMC band of an HIS. In addition, the changes in the return loss of the antennas, which are due to the surface waves, are investigated. Finally, the effects of curvature on the return loss and the radiation patterns of the antennas are stated.

4.1. Operational Band

HISs are promising ground plane candidates for low-profile antenna applications since they do not hinder the radiation performance of an antenna placed in close proximity to them. Furthermore, because of their unique reflection phase characteristics, HISs improve the radiation performance of antennas compared to ideal PMC ground planes [3]. If metallic posts (vias) are also included in an HIS geometry, as in mushroom surfaces, the propagation of surface waves can be suppressed, which allows us to obtain smoother radiation patterns [9].

The radiation performance of an antenna, in the presence of an HIS, is determined by the reflection phase characteristics of the HIS. Usually, the reflection phase diagrams of HISs are attained by assuming a plane wave incidence and far field radiation. However, in a low-profile antenna application, the HIS is in the near field of the antenna in which the radiated fields by the antenna cannot be considered as plane waves. In addition, the reactive fields are extremely dominant in the near field of an antenna. Hence, the operational band of an HIS for a low-profile antenna application is expected to be different than its reflection phase band.

The operational bandwidth of an HIS can be determined by the input impedance of an antenna mounted on top of it. Assuming that a -10 dB return loss is sufficient for a good impedance match for a radiator, the bandwidth of the HIS can be defined as the frequency interval in which the return losses of antennas are smaller than -10 dB. This is known as *the input-match band* of the HIS [3]. In [3], a practical interval, which was obtained empirically, for the operational band of an HIS is given as the frequency interval in which the reflection phase takes values between 135° and 45°. However, it is already known that the input impedance, hence the return loss, of an antenna also depends on the distance between the antenna and HIS. Therefore, a more rigorous method is necessary to determine the operational bandwidth of an HIS.

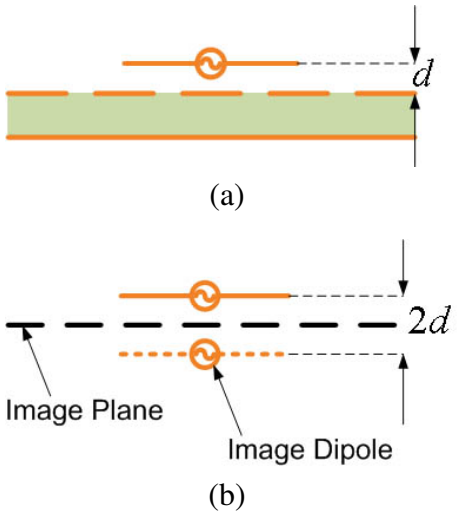

Fig. 4.1. Schematic drawing of a dipole mounted on a flat HIS. (a) The actual geometry. (b) Equivalent geometry.

Consider the geometry depicted in Fig. 4.1, where a typical low-profile application of a dipole is sketched. If the HIS is assumed to be sufficiently large, by using the image theory, the equivalent geometry can be obtained as displayed in Fig. 4.1(b). For a flat and infinite PEC

ground plane, the current on the image flows in the opposite direction of the actual current, which corresponds to a phase difference of 180°. On the other hand, for a PMC ground plane, both currents are in the same direction; i.e., they are in phase. In the case of an HIS, the phase difference between the source and its image is determined by the reflection phase of the HIS. It is known that the reflection phase of an HIS is a function of incidence angle. Hence, for a localized source which is in the near-field region, all of the components in the spectral domain expansion are expected to contribute to the phase difference between the actual and image currents. However, fortunately, the input impedance of an antenna is mostly impacted by the components which are in the vicinity of normal incidence [38], [39]. For those angles, the surface impedance of the HIS changes very slowly. Therefore, the reflection phase response, for a plane wave and normal incidence, of an HIS can be utilized to obtain the return loss of an antenna located in its vicinity.

To obtain the return loss of an antenna located near an HIS, one should find its input impedance first. Since, for a low-profile application, the distance between the antenna and the HIS is extremely small, there is a very strong mutual coupling between the actual antenna and its image. In such a case, the input, or so called the *driving point*, impedance is a function of the antenna's self impedance Z_{11} and the mutual impedance Z_{12} between the antenna and its image [40]. The driving point impedance of the antenna is given in (4.1) where ϕ represents the phase difference between the actual and the image currents. Clearly, this phase difference is a function of the the reflection phase of the HIS and the elevation of the antenna [41], [42]. The reader should also keep in mind that the mutual impedance is also a function of the distance between the antenna and HIS.

$$Z_d = Z_{11} + Z_{12}e^{j\phi} \tag{4.1}$$

After the driving point is calculated, the return loss can be obtained as expressed in (4.2), where Z_0 is the characteristic impedance of the feeding structure [41]. Of course, this is not an exact solution; nevertheless it gives reasonably good estimates for the resonant frequency of an antenna located near an HIS.

$$S_{11} = \frac{Z_d - Z_0}{Z_d + Z_0} \tag{4.2}$$

Having this analytical approach discussed, a practical case can be considered, as illustrated in Fig. 4.2, where a dipole antenna is placed $0.025\lambda_{15}$ above an HIS. λ_{15} represents the free space wavelength at 15 GHz. The patch size and proximity of the HIS are $0.15\lambda_{15}$ and $0.025\lambda_{15}$, respectively. The height of the substrate is $0.05\lambda_{15}$ and its relative permittivity is 2.2. To obtain the operational band of the HIS, its return loss was simulated for different dipole lengths.

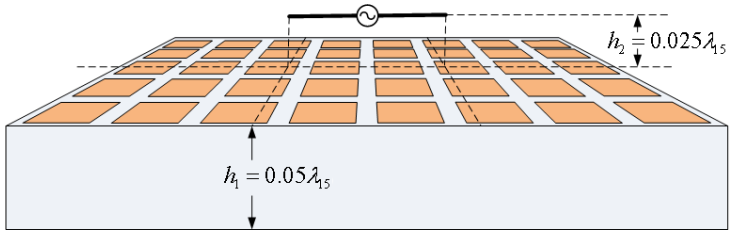

Fig. 4.2. A schematic drawing of a low profile antenna application of an HIS. A dipole is placed in close proximity to a HIS.

Fig. 4.3 displays the return loss of the dipole for different lengths. If the length of the dipole is varied to resonate at different frequencies, the return loss levels at their resonant frequencies would be different in each case because of the presence of the HIS. Again, assuming that -10

dB return loss level is sufficient for a good impedance match, it is obvious from Fig. 4.3 that this particular HIS can perform as a good ground plane, for this specific antenna height, for the antennas operating between 12.4 - 18.4 GHz, which is the input-match bandwidth of the surface.

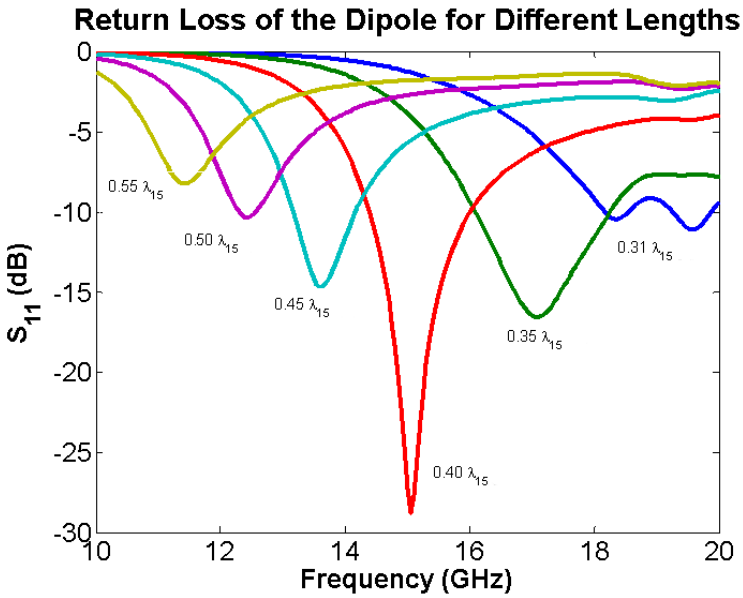

Fig. 4.3. The return losses of the dipoles of different lengths in the presence of an HIS.

Fig. 4.4 shows the reflection phase diagram of the same HIS illustrated in Fig. 4.2. The center frequency of this surface is 19 GHz and clearly, the AMC and input-match bands of the HIS do not match. This illustration successfully verifies the necessity of the new operational band definition.

A careful reader may have noticed that the lengths of the dipoles are smaller than the half wavelength at their individual operating frequencies. Due to the coupling between the antenna and the surface, the antennas resonate at lower frequencies than expected. Hence, HISs can also be utilized to achieve antenna miniaturization [8].

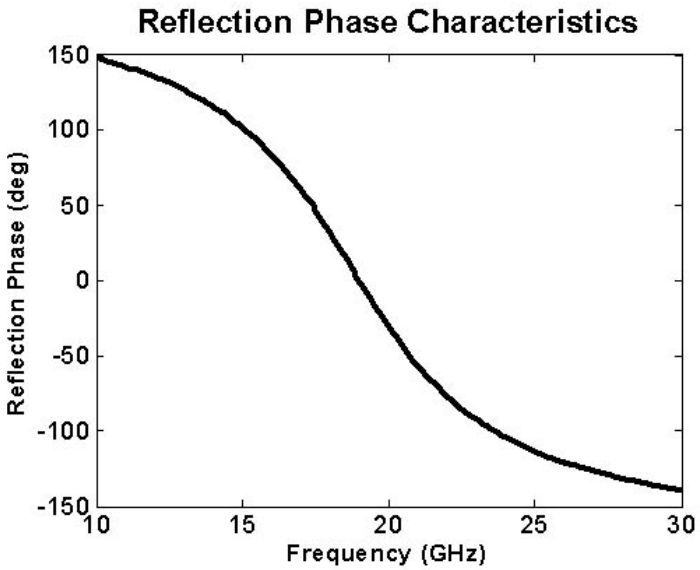

Fig. 4.4. The reflection phase diagram of the HIS in Fig. 5.5.

Another important point, which needs to be mentioned, is that the dipoles resonate efficiently below the center frequency of the HIS which is 19 GHz. This may seem somewhat confusing at the first glance because the minimum return loss is expected at the center frequency where the surface behaves like a PMC. Although this statement may be correct for a plane wave incidence, it is not true for antenna applications. Since the antennas resonate efficiently when they are smaller than a half wavelength, their self impedances should be capacitive around the resonant frequency. On the other hand, the HIS has an inductive surface impedance below its center frequency. Therefore, the imaginary part of the input impedance of the antenna cancels with the imaginary part of the surface impedance and results in a deep resonance [8]. That is, the HIS itself can be used to provide antenna matching, instead of a tuning circuit. This, clearly explains why the input-match band lies on the left hand side of the center frequency.

4.2. Surface Wave Effects

The previous example, which is illustrated in Fig. 4.2, verifies that a dipole antenna mounted on an HIS has an attractive and clean resonance. This is due to the interaction between the antenna and the HIS. However, since the antenna is very close to the surface, it may excite strong surface currents which may distort the return loss of the antenna.

A dipole can generate TE surface waves because of its orientation. In Chapter 3, it has already been mentioned that TE surfaces waves are attributed to the periodic geometry of the structure, and they are also referred to as AGSWs. These surface waves may generate additional resonances whose frequency is determined by the size of the HIS and the propagation constant associated with the surface waves [43].

A cavity model can be utilized to find the positions of those resonances, as stated in [43]. If the HIS is considered as a rectangular cavity, then the propagation constant at resonance can be calculated by using (4.3), where l denotes the length of the HIS in the direction perpendicular to the axis of the dipole. After the propagation constant is calculated, the corresponding frequency is obtained from the dispersion diagram of the HIS [43].

$$\beta l = p\pi \tag{4.3}$$

The validity of the cavity model can be illustrated by several ways. For instance, Fig. 4.5 displays the magnitude of the electric field scattered from the fabricated FHIS, which was introduced in the previous chapter. It has 20 cells in one direction, it is infinite in the other. The FHIS was illuminated by a normally incident plane wave and the scattered fields were computed 100 mm away from the surface. Clearly, due to the cavity resonances, the magnitude

of the scattered field decreases at certain frequencies, which are shown by the arrows. It is also obvious that the reductions in the magnitude of the scattered field are not very dramatic, since a normally incident plane wave is not very efficient to excite the cavity.

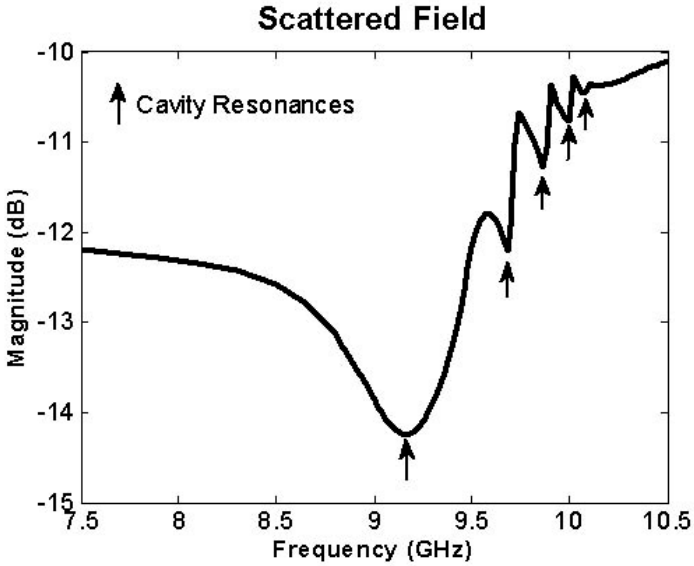

Fig. 4.5. Magnitude of the scattered electric field 100 mm away from the surface. The arrows indicate the cavity resonances.

Table 4.1. Comparison of the cavity model with the full wave simulation.

	Frequency (GHz)				
	$p = 10$	$p = 11$	$p = 12$	$p = 13$	$p = 14$
Cavity	8.93	9.65	9.85	9.94	10.06
HFSS	9.16	9.68	9.86	10.00	10.08

The accuracy of the cavity model can be assessed by comparing its results with the full wave simulation. Table 4.1 illustrates the resonant frequencies obtained by both approaches, which exhibit a very good agreement. Since the length of the HIS is quite large, one can observe the resonances which have orders higher than p =9.

Another way of illustrating the validity of the cavity model is plotting the electric field distribution within the HIS, as shown in Fig. 4.6. At 9.16 GHz, the intensity of the electric field is noticeably higher than that at 8.50 GHz. This demonstrates that at 9.16 GHz, a cavity mode is excited and some part of the energy is confined within the cavity.

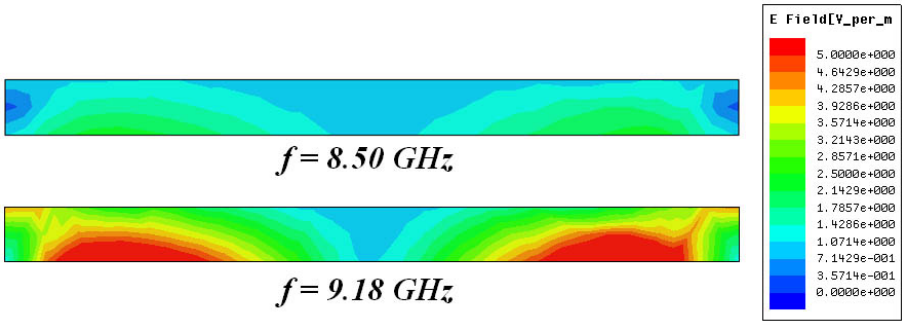

Fig. 4.6. Electric field distribution within the HIS.

Cavity resonances can also be observed in the presence of a localized source. Fig. 4.7 shows the return loss of a wire dipole located on top of a part of the fabricated FHIS, which has 4 cells in both principal axes. The arm length and radius of the dipole are 6.2 mm and 100 mils, respectively. The distance between the center of the dipole and the HIS is 75 mils. The antenna has 4 resonances, of which the first one, which occurs at 8.82 GHz, is due to the interaction between the dipole and the HIS. Starting from this point, this resonance will be referred to as *self resonance*. The other higher resonances are attributed to the surface waves and are referred to as *surface wave resonances*. As stated previously, the locations of the surface wave resonances depend on the size of the HIS, whereas, the self resonance is a function of the reflection phase of the HIS and is independent of its size. The surface wave resonances can be utilized to achieve a wider bandwidths [43].

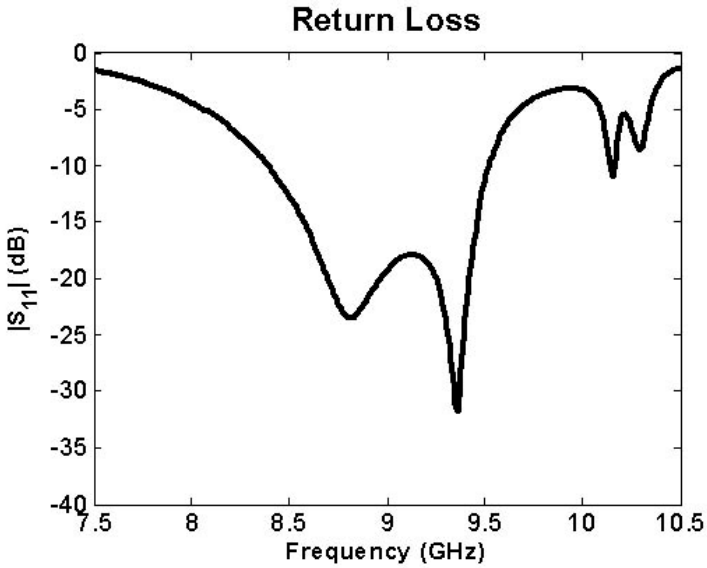

Fig. 4.7. Return loss of the dipole located on top of the 4 by 4 FHIS.

Fig. 4.8 illustrates the comparison of the return losses of the dipole for different FHIS lengths. In the figure, the dimensions of the FHIS are represented by the number of cells in the principal axes. The first and second numbers in the legend, respectively, denote the length and width of the HIS in terms of a unit cell. While all of the FHIS samples have 4 cells along the direction of the dipole axis, their lengths are different. Apparently, the self resonances, which are determined by the reflection phase of the HIS, are identical for all cases. On the other hand, surface wave resonances differ as the lengths of the HISs are different. As expected, the number of surface wave resonances increases with the length of the HIS. Besides, at each surface wave resonant frequency of the HIS of length 4 cells, the HIS of length 8 cells also resonates.

4.3. Curved HIS

The examples that have been discussed so far exhibit the behavior of a dipole antenna mounted on a finite size flat HIS. Starting from this point, the radiation performance of a

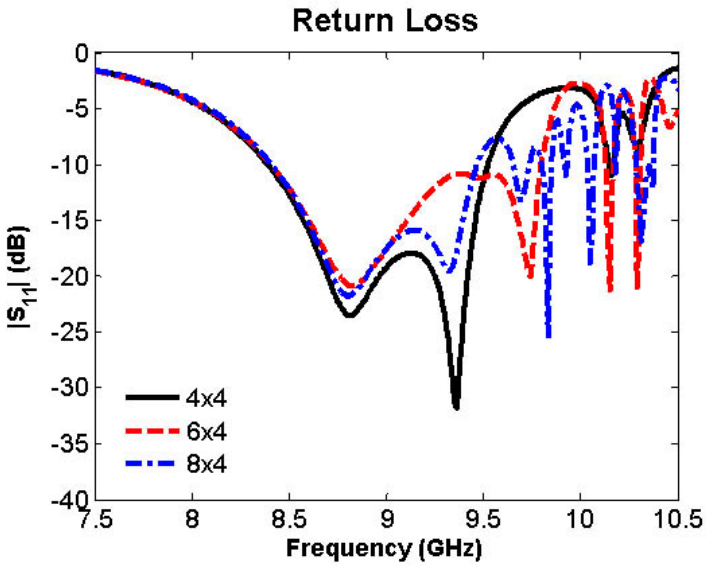

Fig. 4.8. Comparison of the return losses of the dipole located on top the FHIS with different lengths.

dipole on a curved HIS will be investigated. When the HIS is curved in the form of a cylinder, there can be two possible antenna orientations for a low-profile conformal antenna application, as illustrated in Fig. 4.9. A dipole can be conformed to the surface, as shown in Fig. 4.9(a), or it can be oriented parallel to the axis of the cylinder, as shown in Fig. 4.9(b). These orientations are denoted as TE^z (perpendicular) and TM^z (parallel) polarizations, respectively.

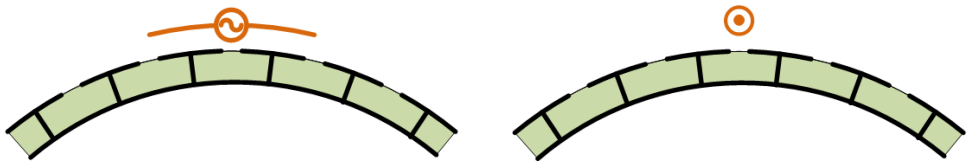

(a) (b)

Fig. 4.9. Schematic drawings of low profile applications of a dipole mounted on a curved HIS. (a) TE^z (perpendicular) polarization. (b) TM^z (parallel) polarization.

It has been explained that when a dipole is located on a HIS, two different types of resonances can occur: self and surface wave resonances. Since the mechanisms of these resonances are different, they will be examined separately.

4.3.1. *Self Resonance*

The self resonant frequency of an antenna mounted on a HIS is basically determined by reflection phase of the HIS and the distance between the antenna and the surface. It was shown that, for a dipole antenna, this resonance occurs in the inductive region of the HIS. In Chapter 3, it was also verified that the reflection phase of the HIS, in its inductive region, remains unchanged when it is curved. Therefore, one should expect the self resonance of a dipole to be independent of the curvature of the HIS. Similarly, the input-match bandwidth, which is of particular interest, of the curved HIS should be very close to that of the flat HIS. Slight differences can be expected since the reflection phase diagrams associated with the spectral components that correspond to oblique incidence are subject to change with the curvature.

To demonstrate this, as in the case of a flat HIS, the lengths of the dipoles are varied and the return losses of the antennas are simulated. In these simulations, the antenna height and the surface parameters, except the curvature, are selected to be identical with the flat HIS of Fig. 4.2. The radius of curvature is set to 3 inches (76.2 mm). As anticipated, similar to the reflection phase band, the input-match bands of the flat and curved HISs, for both antenna orientations, are found to be very close to each other. The return losses are compared in Fig. 4.10, where the return losses of the flat, TE^z and TM^z polarized curved cases are plotted by solid, dashed and dash-dotted lines, respectively.

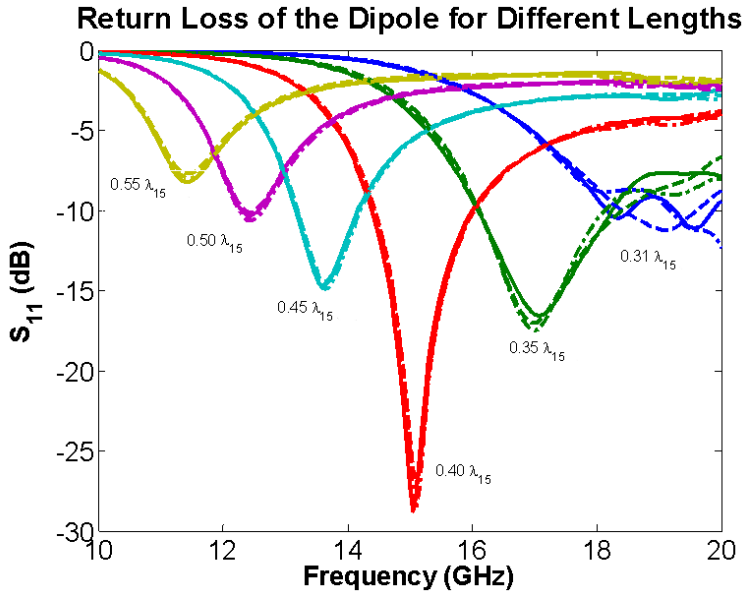

Fig. 4.10. Comparison of the return losses of the dipoles of different lengths mounted on flat and curved HISs. Solid lines are for the flat case. The return losses, for the curved case, for TE^z and TM^z polarizations are shown by dashed and dash-dotted lines, respectively.

The previous simulations are performed for a constant radius of curvature (ρ_0). To be able to make more concrete and reliable conclusions, one should examine the effects of the curvature variations on the return loss of a dipole and input-match bandwidth of a HIS. For this purpose, the return loss of the 0.4 λ_{15}-long dipole is simulated for different radii of curvature. Figs. 4.11 and 4.12 illustrate the return losses of the dipole. Apparently, the return loss of the dipole remains almost constant, provided that the radius of curvature is larger than a wavelength. This simulation also verifies that the position of the self resonance of a dipole mounted on a HIS is independent of the curvature.

4.3.2. *Surface Wave Resonance*

For the analysis of surface wave resonances of curved HISs, one can use the cavity model used for the flat case. The HIS can be considered as a concentric sectoral cylindrical cavity

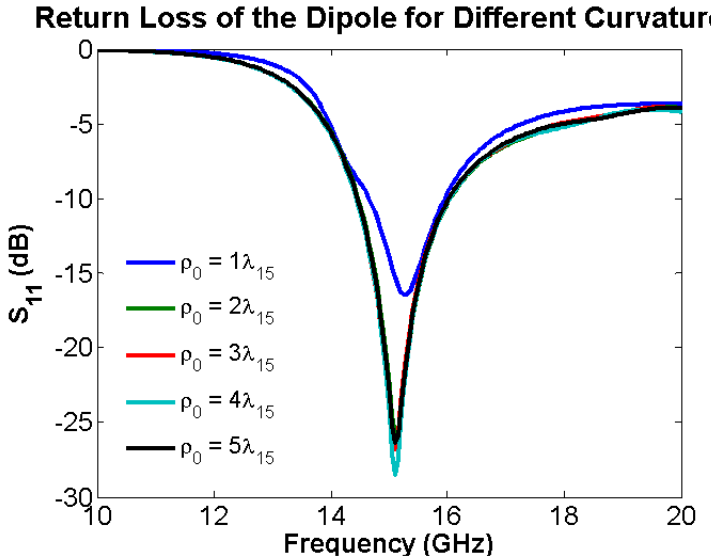

Fig. 4.11. Comparison of the return loss of the 0.4 λ_{15} dipole on a curved HIS with different radii of curvature for TE^z (perpendicular) polarization.

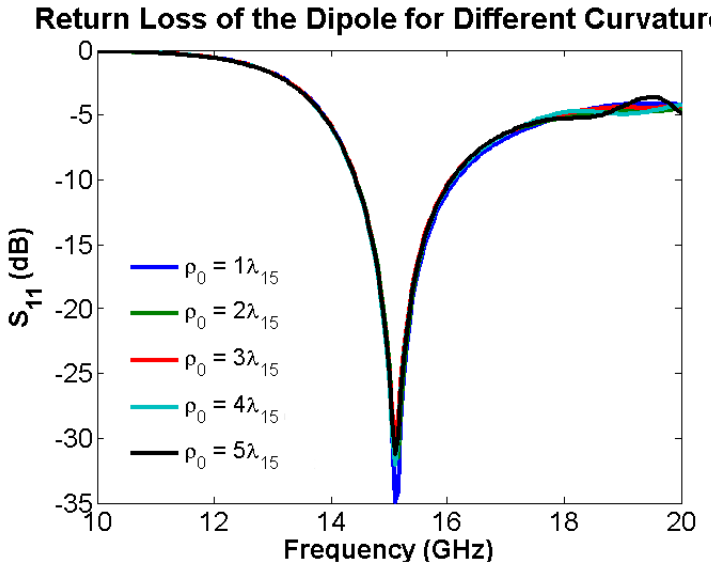

Fig. 4.12. Comparison of the return loss of the 0.4 λ_{15} dipole on a curved HIS with different radii of curvature for TM^z (parallel) polarization.

and the propagation constant within the cavity can be obtained by applying the appropriate boundary conditions. PEC boundary condition can be assumed for the top and bottom surfaces. The other surfaces are approximated by a PMC boundary condition. Then, for a semi-infinite

curved HIS, the electric field for a TE surface wave can be written as in (4.4) [44], where ϕ_0 denotes the half of the angular length of the cavity along the ϕ direction and C is a constant.

$$E_z = CB_{TE}(\rho)\sin(m(\phi - \phi_0)) \tag{4.4}$$

The function $B_{TE}(\rho)$ is expressed in (4.5), where J_m and Y_m are the Bessel functions of the first and second kind, respectively. The order of those functions are determined by the length of the HIS along the ϕ direction, $m = p\pi/2\phi_0$.

$$B_{TE}(\rho) = Y_m(x_{pn}\frac{\rho}{\rho_0}) - \frac{Y_m(x_{pn})}{J_m(x_{pn})}J_m(x_{pn}\frac{\rho}{\rho_0}) \tag{4.5}$$

x_{pn} is a root of (4.6). The distances ρ_0 and ρ_1 are shown in Fig. 3.5 and they denote the curvature of the bottom and top surfaces of the HIS, respectively.

$$f = J_m(x_{pn})Y_m(x_{pn}\frac{\rho_1}{\rho_0}) - Y_m(x_{pn})J_m(x_{pn}\frac{\rho_1}{\rho_0}) = 0 \tag{4.6}$$

The propagation constant of the surface waves within the HIS can be represented by (4.7).

$$\beta = \frac{x_{pn}}{\rho_0} \tag{4.7}$$

Since the orders (m) of the Bessel functions depend on the length of the HIS along the circumferential direction, any variation in the length will change the propagation constant of the cavity. Hence, as in the flat case, the surface wave resonant frequencies should be a function of the surface length.

To find the effects of the curvature on the surface wave resonances, one should focus on the the solution of (4.6). Fig. 4.13 exhibits the function f, with respect to x_{pn}/ρ_0, when

$m = p = 0$. The values of f are contrasted for two different radii of curvature which are within the reasonable practical range. Obviously, the zero crossings, or roots, of the function f do not change with curvature, which means that the propagation constant is independent of the curvature. In other words, the surface wave resonant frequencies should not change with the curvature. Similar results can also be obtained for higher order Bessel functions.

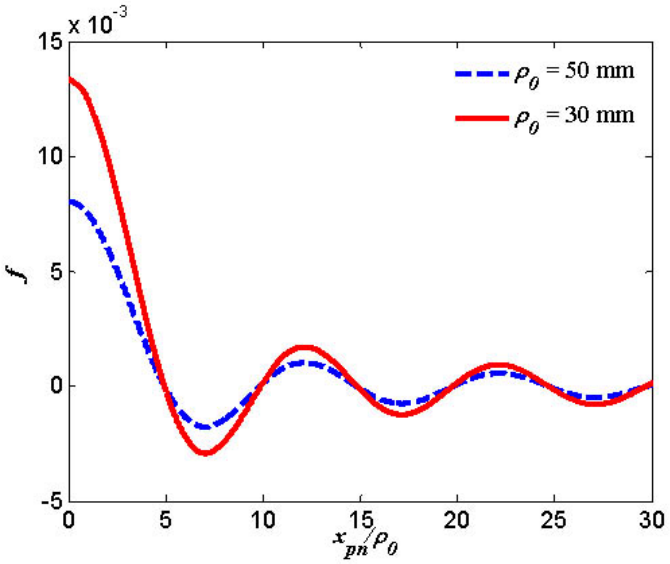

Fig. 4.13. Function f of (4.6) for m =0.

In addition to the previous numerical verification, it is also possible to perform an analytical proof. Since the first zero crossing, for $\rho_0 = 30$ mm, of the function f occurs when the argument $(x_{pn}\frac{\rho_1}{\rho_0})$ of the Bessel function is around 150, the asymptotic approximations of the Bessel functions for large arguments can be utilized in this process. The approximate expressions for the Bessel functions are given in (4.8) and (4.9).

$$J_m(x) \approx \sqrt{\frac{2}{\pi x}}\cos(x - \frac{m\pi}{2} - \frac{\pi}{4}) \tag{4.8}$$

$$Y_m(x) \approx \sqrt{\frac{2}{\pi x}} \sin(x - \frac{m\pi}{2} - \frac{\pi}{4}) \tag{4.9}$$

After making the following substitutions,

$$u = k_{pn}\rho_0 - \frac{m\pi}{2} - \frac{\pi}{4} \tag{4.10}$$

$$v = k_{pn}\rho_1 - \frac{m\pi}{2} - \frac{\pi}{4} \tag{4.11}$$

$$h = \rho_1 - \rho_0 \tag{4.12}$$

the function f can be written as

$$f \approx \frac{2}{\pi\beta\sqrt{\rho_0\rho_1}}(\cos u \sin v - \sin u \cos v) \tag{4.13}$$

which can be further simplified to (4.14).

$$f \approx \frac{2}{\pi\beta\sqrt{\rho_0\rho_1}} \sin(\beta h) \tag{4.14}$$

In (4.14), it is clearly seen that the function f becomes zero whenever βh is equal to zero. This simply indicates that the propagation constant β depends only on the thickness of the HIS. It is also known that the dispersion diagram is not a function of the HIS size since it is computed by assuming an infinite structure. Therefore, the surface wave resonant frequencies should be independent of the curvature.

Fig. 4.14 illustrates the return loss of a dipole mounted on the FHIS, which is comprised of 4 by 4 cells, for different curvatures. As anticipated, the self and surface wave resonant frequencies basically do not change with the curvature. The self resonant frequency of the antenna tends to increase as the radius of curvature decreases. As mentioned before, this can be attributed to the change of the reflection phase associated with different components

in the spectral domain. Furthermore, the distance between the antenna and the surface, for incidence angles other than normal incidence, is a function of the curvature. Although the resonant frequencies do not change with curvature, the magnitude of the return loss at those resonances can change since the excitation efficiency for each surface wave mode depends on the curvature. Similar results, for the FHIS comprised of 8 by 4 cells, are shown in Fig. 4.15.

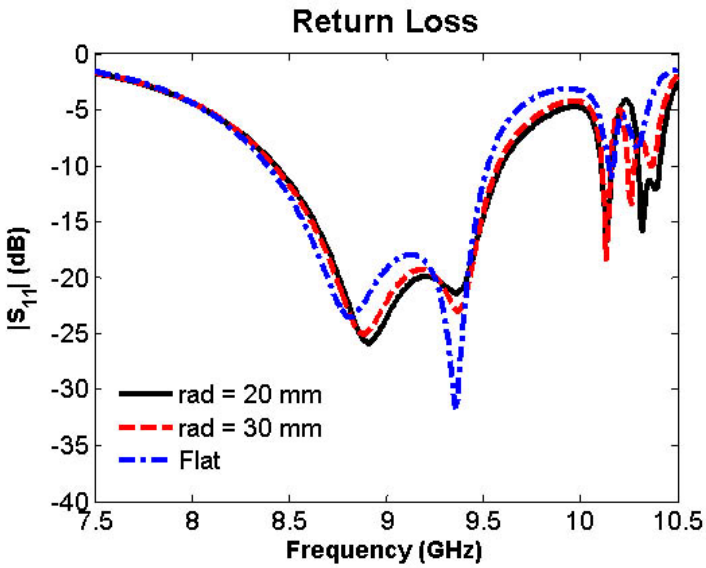

Fig. 4.14. Comparison of the return losses of the dipole mounted on the curved FHIS for different curvatures. The antenna is parallel to the axis of the cylinder and the FHIS is comprised of 4 by 4 cells.

The same theory and interpretations apply for perpendicular polarization, as well. The return losses for this polarization are exhibited in Figs. 4.16 and 4.17. As in the previous case, for both FHIS sizes, the locations of the resonances basically do not change. At this point, it should be mentioned that since the patch dimensions of the FHIS are different along the two principal axes, to be able to make a fair comparison, the HIS, as well as the dipole, should be rotated.

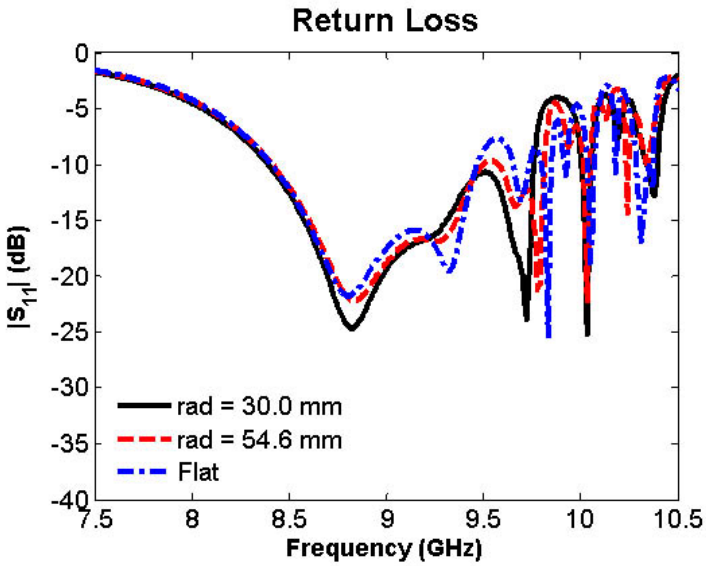

Fig. 4.15. Comparison of the return losses of the dipole mounted on the curved FHIS for different curvatures. The antenna is parallel to the axis of the cylinder and the FHIS is comprised of 8 by 4 cells.

4.3.3. *Amplitude Radiation Patterns*

In order to make a meaningful radiation performance comparison, besides the return loss, one should also consider the amplitude radiation patterns of the antennas. The E- and H- plane patterns of the dipole mounted on the FHIS, for different HIS size, antenna orientation, and curvature, are displayed in Figs. 4.18 - 4.25. The patterns are computed at 8.9 GHz, which is the self resonant frequency of the dipole. As expected, for all the cases, the realized gain of the antenna is on the order of 8 dBi. The realized gain slightly decreases with the radius of curvature; conversely, the main beamwidth increases. The strongest back lobe radiation, which is due to the diffraction at the edges of the FHIS, is observed for the flat cases. Moreover, a null-filling effect can be seen, particularly for the H-plane patterns, as the radius of curvature decreases.

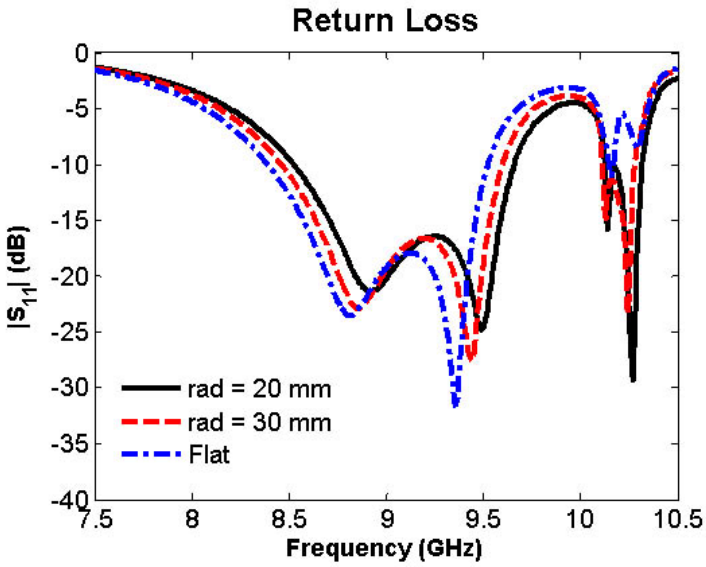

Fig. 4.16. Comparison of the return losses of the dipole mounted on the curved FHIS for different curvatures. The antenna is perpendicular to the axis of the cylinder and the FHIS is comprised of 4 by 4 cells.

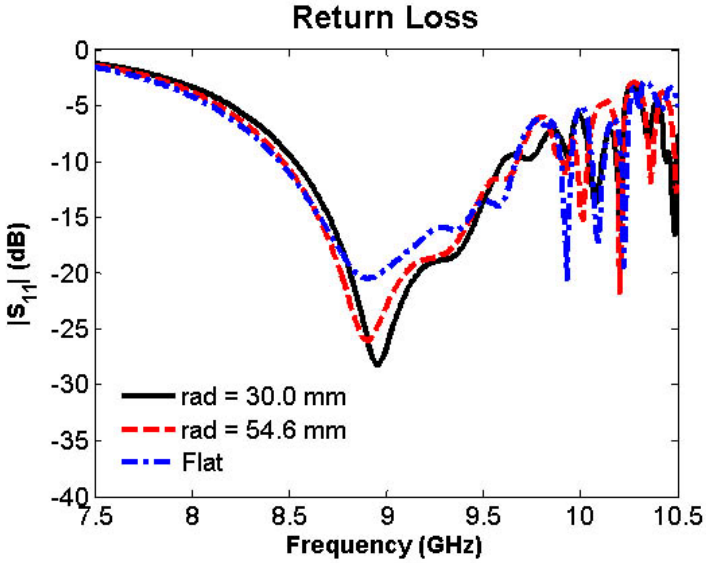

Fig. 4.17. Comparison of the return losses of the dipole mounted on the curved FHIS for different curvatures. The antenna is perpendicular to the axis of the cylinder and the FHIS is comprised of 8 by 4 cells.

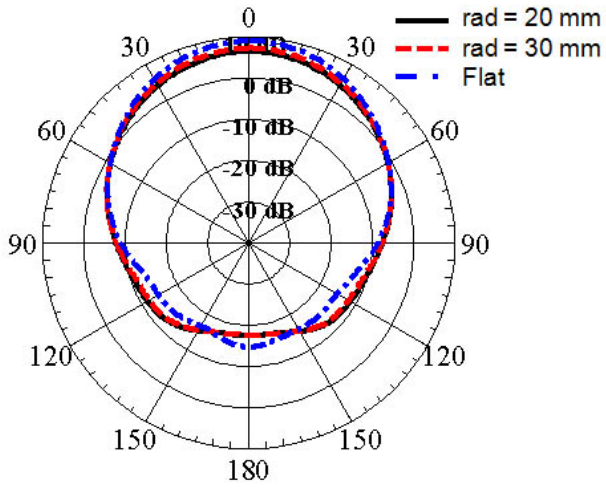

Fig. 4.18. Comparison of the E-plane radiation patterns of the dipole mounted on the curved FHIS for different curvatures. The antenna is parallel to the axis of the cylinder and the FHIS is comprised of 4 by 4 cells.

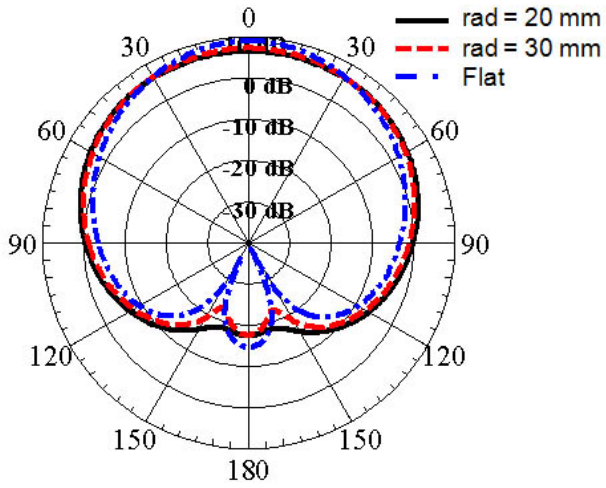

Fig. 4.19. Comparison of the H-plane radiation patterns of the dipole mounted on the curved FHIS for different curvatures. The antenna is parallel to the axis of the cylinder and the FHIS is comprised of 4 by 4 cells.

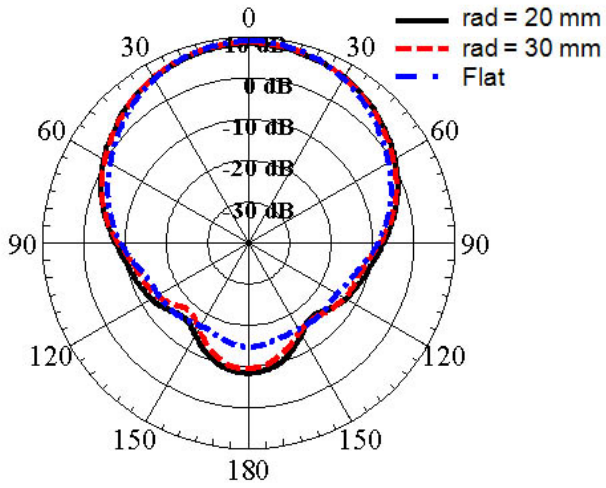

Fig. 4.20. Comparison of the E-plane radiation patterns of the dipole mounted on the curved FHIS for different curvatures. The antenna is perpendicular to the axis of the cylinder and the FHIS is comprised of 4 by 4 cells.

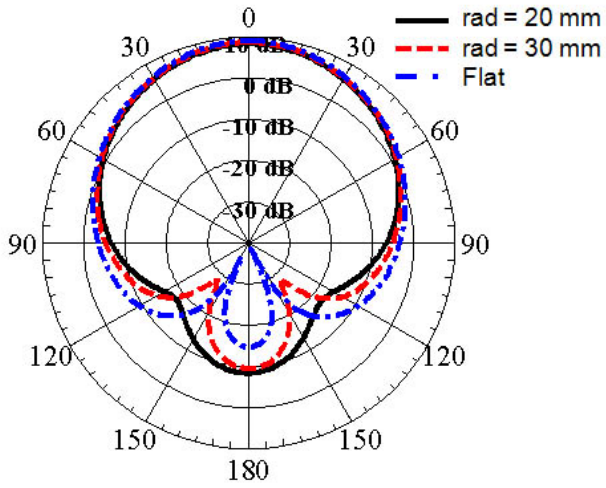

Fig. 4.21. Comparison of the H-plane radiation patterns of the dipole mounted on the curved FHIS for different curvatures. The antenna is perpendicular to the axis of the cylinder and the FHIS is comprised of 4 by 4 cells.

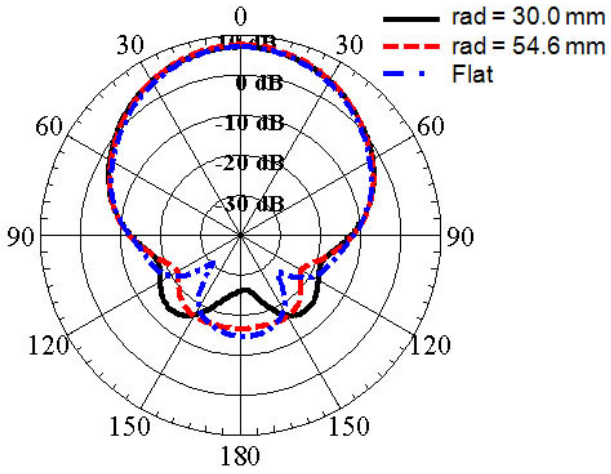

Fig. 4.22. Comparison of the E-plane radiation patterns of the dipole mounted on the curved FHIS for different curvatures. The antenna is parallel to the axis of the cylinder and the FHIS is comprised of 8 by 4 cells.

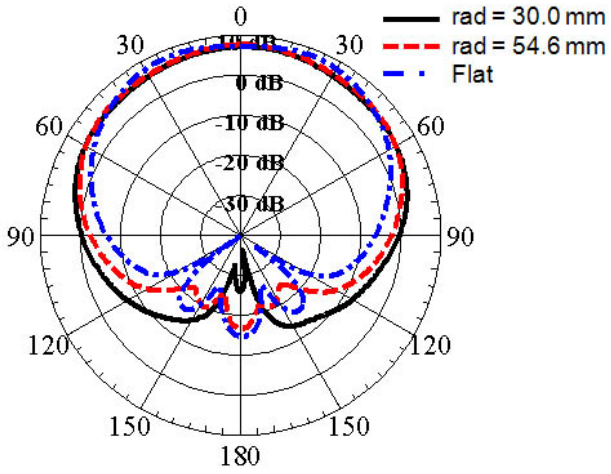

Fig. 4.23. Comparison of the H-plane radiation patterns of the dipole mounted on the curved FHIS for different curvatures. The antenna is parallel to the axis of the cylinder and the FHIS is comprised of 8 by 4 cells.

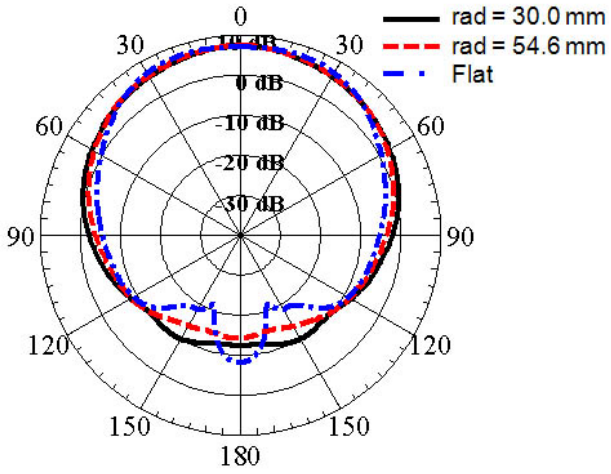

Fig. 4.24. Comparison of the E-plane radiation patterns of the dipole mounted on the curved FHIS for different curvatures. The antenna is perpendicular to the axis of the cylinder and the FHIS is comprised of 8 by 4 cells.

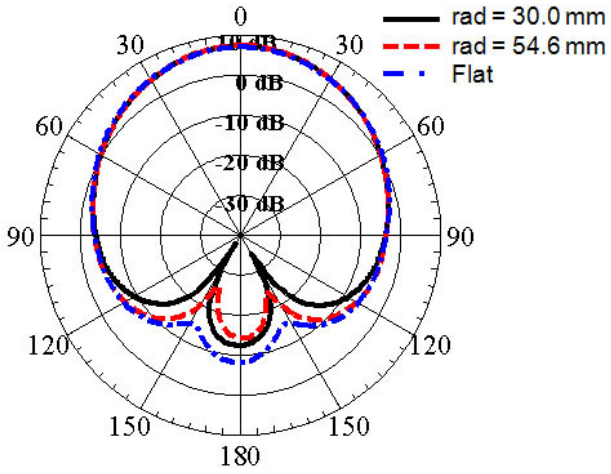

Fig. 4.25. Comparison of the H-plane radiation patterns of the dipole mounted on the curved FHIS for different curvatures. The antenna is perpendicular to the axis of the cylinder and the FHIS is comprised of 8 by 4 cells.

4.3.4. *Concave Reflector*

As another possible application, the FHIS can also be utilized as a concave reflector. In this scenario, the surface is bent in the other direction, as illustrated in Fig. 4.26. This structure is very similar to a cylindrical reflector fed by a wire dipole, except that the antenna is placed in close proximity to the reflector instead of at its focal point. For simplicity, only parallel polarization is considered for this application.

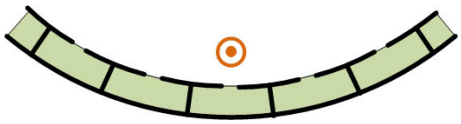

Fig. 4.26. Schematic diagram of the concave HIS reflector.

Fig. 4.27 exhibits the return loss of the dipole which is mounted on the 8 by 4 concave FHIS. The radius of curvature is approximately 21.52 mm, such that the FHIS forms a half cylinder. The distance between the surface and the antenna is exactly the same as in the previous examples. Apparently, because of the multiple reflections from the reflector, the self resonant frequency is shifted to 8.6 GHz; but it is still within the input-match band of the FHIS. Surface wave resonant frequencies are also changed due to the same reasoning.

The E- and H-plane radiation patterns of the dipole are shown in Fig. 4.28. Since the concave geometry reduces the back lobe radiation significantly, there is an increase in the realized gain of the structure. The new gain is on the order of 12 dBi.

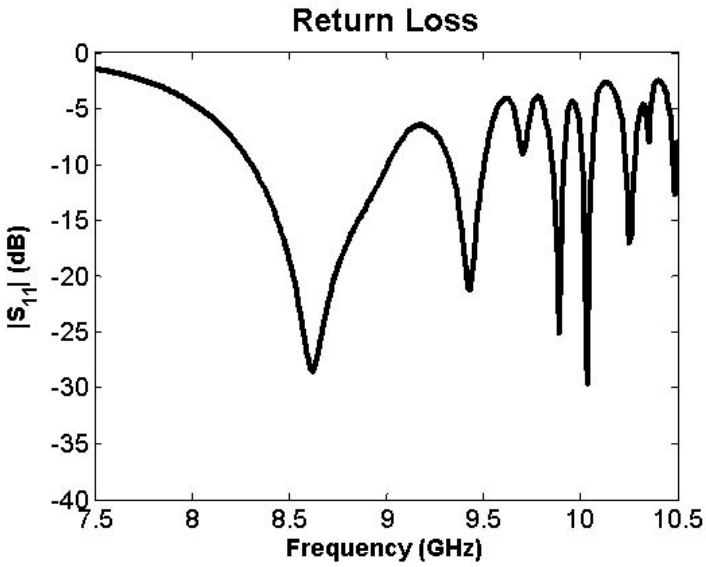

Fig. 4.27. Return loss of the dipole mounted on the concave FHIS. The radius of curvature is 21.52 mm. The antenna is parallel to the axis of the cylinder and the FHIS is comprised of 8 by 4 cells.

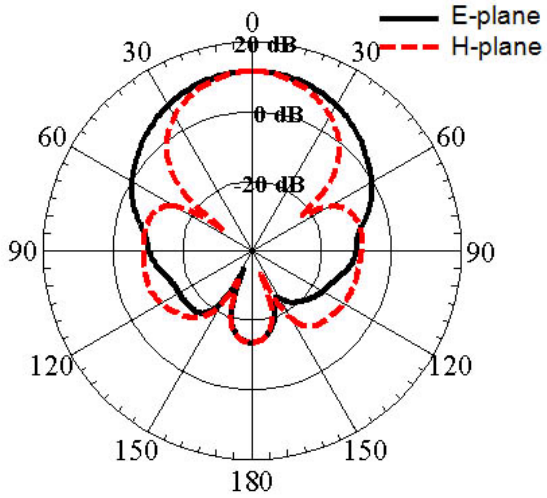

Fig. 4.28. E- and H-plane radiation patterns of the dipole mounted on the concave FHIS. The radius of curvature is 21.52 mm. The antenna is parallel to the axis of the cylinder and the FHIS is comprised of 8 by 4 cells.

CHAPTER 5

PERFORATED HIGH IMPEDANCE SURFACES

For low-profile antenna applications, particularly for the applications that utilize flexible substrates, the thickness of the substrate is usually chosen to be much smaller than the operating wavelength. In addition, in most cases, the size of the ground plane is finite and limited to the available space, which affects the performance of an antenna mounted on it. The size of the unit cell is also important in terms of the dependency of the reflection characteristics to the angle of incidence. It is already known that the sensitivity of an HIS to the angle of incidence decreases with the unit cell size [45]. That is, compactness of an HIS can be extremely important for some cases. On the other hand, a large bandwidth has always been a preferred property for most RF systems. Therefore, it is usually desirable to design an HIS with large bandwidth, thin substrate and small unit cell size.

HIS unit cell miniaturization can be accomplished by utilizing different types of patches, including spiral [46], slotted [3] and space filling curve [47] type patches, instead of square ones. Nevertheless, the immediate shortcoming of these HISs is the bandwidth reduction. In fact, for a given substrate thickness and patch width, the maximum bandwidth can be achieved by square patches [9]. Thus, because of the aforementioned design limitations of a conventional HIS, it is not possible to decrease the operating frequency and increase the bandwidth, at the same time.

These limitations and a need for a compact and wideband flexible HIS, resulted in the quest of a novel HIS geometry which solves the miniaturization and bandwidth enhancement problems, simultaneously. Indeed, this can be accomplished by perforating the ground plane periodically, as shown in Fig. 5.1. This type of a structure was previously considered in [45] to miniaturize single layer Frequency Selective Surfaces and its transmission properties were

discussed. However, in this dissertation, the structure is considered as an AMC ground plane, which is proposed to decrease the operating frequency and increase the bandwidth of two-layer HISs. Its reflection properties are investigated and compared with those of the conventional HISs. Moreover, surface wave (SW) suppression characteristics of these surfaces are also examined in detail.

As discussed in Chapter 2, EBG structures are also used to suppress SWs. It was also mentioned that, to achieve SW suppression at sub-wavelength frequencies, the substrate can be perforated by metallic posts, referred to as *vias*. However, the vias should be avoided in flexible or conformal applications as they are extremely vulnerable to bending. Fortunately, the HISs with periodically perforated ground planes are verified to be capable of suppressing SWs. This can be accomplished by designing the geometry of the perforations properly. Hence, vias can be eliminated without hindering the EBG properties.

This chapter starts with the reflection phase analysis of the novel HIS geometry, which is followed by an examination of antenna performance on these surfaces. Finally, SW suppression characteristics are investigated.

5.1. Design Geometry and Analytical Model

As it has been mentioned previously, the square root of surface inductance is directly proportional to the bandwidth and inversely proportional to the center frequency of an HIS. Therefore, in contrast to the capacitance, an increase in the inductance should result in a lower resonant frequency and a wider bandwidth. It is also known that the inductance of an HIS depends only on the permeability and the thickness of the dielectric substrate. Hence, it is not possible to change the inductance of a conventional HIS without changing the dielectric

material. Alternatively, the inductance of an HIS can be increased, without changing its unit cell dimensions and thickness, by perforating the ground plane periodically, as illustrated in Fig. 5.1. The ground plane can also be considered as a metallic grid composed of perpendicularly intersecting strips of width w_s. In this structure, the currents circulating around the perforations generate a magnetic flux, which flows through the holes and this results in an extra inductance. This additional inductance increases the equivalent inductance of the overall structure, resulting in a lower resonant frequency and larger bandwidth.

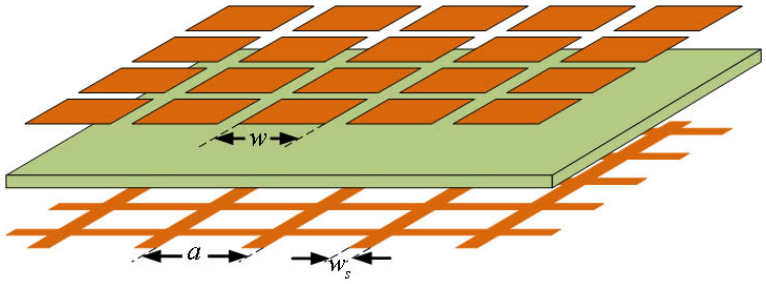

Fig. 5.1. Physical geometry of an HIS with periodically perforated ground plane. On top, there is the capacitive array of metallic patches. The second layer is the dielectric substrate. The bottom layer is the inductive grid.

Similar to the conventional HIS, a transmission line model can be developed for the perforated HIS as shown in Fig. 5.2, where Z_P and Z_G denote the impedances of the array of patches and the perforated ground plane, respectively. The dielectric layer behaves as an impedance transformer of length h, which is the thickness of the substrate. Z_0 is the wave impedance in the surrounding medium. Undoubtedly, the wave impedance is a function of the angle of incidence and the polarization of the incident field. Since the expression for Z_P is already introduced in Chapter 2, only Z_G is given here.

$$Z_G^{TM} = j\frac{\eta_{eff}}{2}\alpha_G\left(1-\frac{k_0^2}{k_{eff}^2}\frac{\sin^2\theta}{2}\right) \tag{5.1}$$

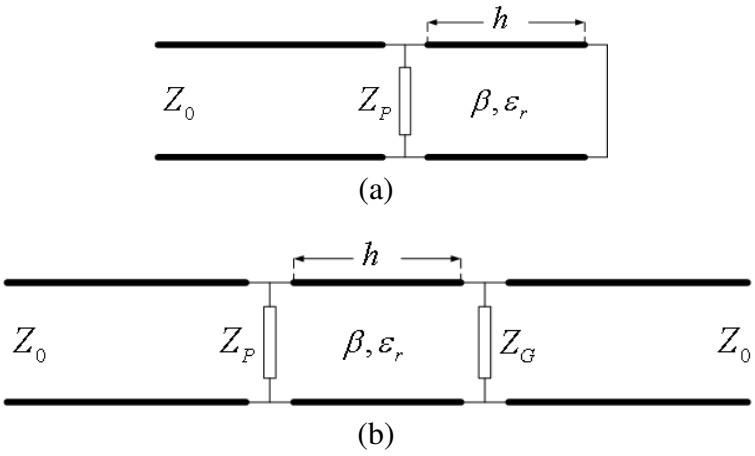

Fig. 5.2. Transmission line model of the HIS. (a) Conventional HIS. (b) New HIS with the perforated ground plane.

$$Z_G^{TE} = j\frac{\eta_{eff}}{2}\alpha_G \tag{5.2}$$

$$\alpha_G = \frac{k_{eff}a}{\pi}\ln\left(\frac{1}{\sin\frac{\pi w_s}{2a}}\right) \tag{5.3}$$

The grid parameter α_G of the perforated ground plane is defined in (5.3). The effective intrinsic impedance η_{eff} and propagation constant k_{eff} are related to the effective permittivity ε_{eff} of the surface which was given in Chapter 2. The reader should also be aware that the expression for Z_G is obtained in the absence of the patch array, Similarly, Z_P is obtained in the absence of the grid layer. Therefore, when the two layers are very close to each other, these equations may not give very accurate estimates.

It is obvious that, while the array of patches has a capacitive impedance, the impedance of the perforated ground plane is inductive. The equivalent capacitance of the surfaces increases with the patch width w. On the other hand, the inductance decreases as the strip width w_s increases. In other words, larger surface inductances can be obtained by larger perforations.

Because the magnitude of the magnetic flux flowing through the ground plane increases with the perforation size, it results in a larger equivalent inductance.

5.2. Reflection Phase

In order to observe the reflection properties of the proposed HIS, one sample is designed and simulated by HFSS. The unit cell size a and the patch width w are selected to be 5 and 4.1 mm, respectively. The dielectric material is Rogers RT/duroid 5870 [48] with a dielectric constant of 2.33 and thickness of 1.524 mm. The widths of the strips are varied from 1 to 3 mm and the effects of the strip width on the center frequency and bandwidth are investigated. The center frequency is assumed to be the point where the surface behaves as a perfect magnetic conductor (zero reflection phase). The bandwidth is considered as the frequency interval where the reflection phase takes values between $+90^\circ$ and -90°.

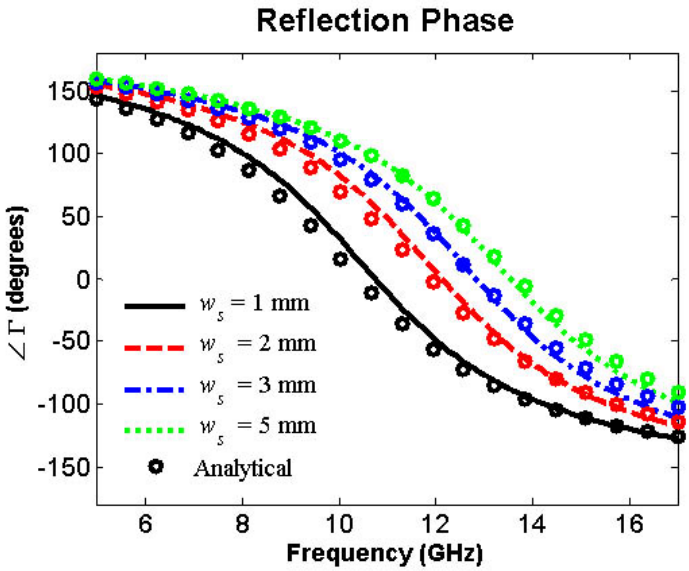

Fig. 5.3. Comparison of the simulated and analytical reflection phase for different strip widths.

Fig. 5.3 shows the reflection phase of the new HIS for different strip widths and that of the conventional HIS with identical unit cell dimensions. The numerical results are also compared

with the analytical ones, obtained by the transmission line model discussed in the pervious section. The numerical solutions are obtained by simulating a single unit cell of the infinite HIS.

The agreement between the analytical and numerical models is excellent for this specific geometry. The agreement may not be very good for some other designs as the analytical formulation is not proved to be valid for any HIS. However, the analytical formulation can still be used to obtain an initial design. The designs can then be fine tuned by numerical simulations.

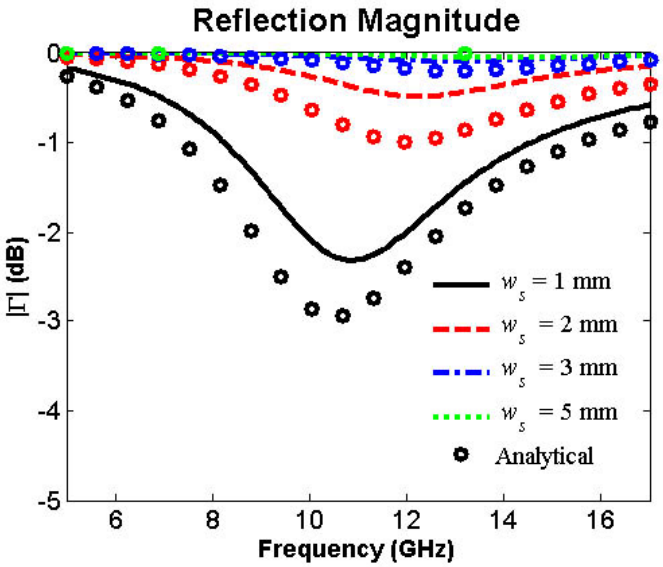

Fig. 5.4. The magnitude of the reflection coefficient for different strip widths.

As expected, the width of the strips, or the perforation size, has a very significant effect on the reflection characteristics of the surface. Clearly, the center frequency of the surface decreases with the strip width. On the other hand, the fractional bandwidth increases as strip width decreases. Hence, without changing the physical dimensions of a unit cell, one can achieve lower frequencies of operation and larger bandwidths, simultaneously, by decreasing

the strip width. However, as the size of the holes within the ground plane is increased, more energy is allowed to leak to the other side of the HIS. Therefore, the magnitude of the reflection coefficient, within the operational bandwidth, decreases with the strip width. Fig. 5.4 exhibits a comparison of the analytical and numerical models for different strip widths. While the agreement is excellent for smaller perforations, it gets worse as the strip width decreases.

Table 5.1. Reflection characteristics of the proposed HIS.

	f_0 (GHz)	BW (%)	$\|\Gamma\|$ (dB)
$w_s = 5.0$ mm	13.5	40.7	-0.06
$w_s = 3.0$ mm	13.0	41.5	-0.10
$w_s = 2.0$ mm	12.0	43.3	-0.50
$w_s = 1.0$ mm	10.7	48.6	-2.30

Table 5.1 summarizes the simulation results that verify the compromise between bandwidth improvement and reflected power. Hence, a designer should take into account the amount of leakage that can be tolerated to determine the size of the perforations and unit cell dimensions. For instance, for the given design, it is possible to obtain a 20.7% decrease in the center frequency and 7.9% bandwidth improvement at an expense of 2.3 dB reduction in the magnitude of the reflection coefficient. On the other hand, as described in Chapter 4, in low-profile antenna applications, HISs are generally operated in their inductive region. Therefore, for such an application, the amount of power loss should be smaller. For instance, if a 0.375 λ dipole is located at a 0.06 λ distance above the PHIS, with strip width w_s of 1 mm, the dipole resonates around 9.5 GHz. Be aware of that the length of the dipole is much smaller than a half wavelength. The magnitude of the reflection coefficient of the PHIS, at the resonant frequency, is -1.8 dB. Fig. 5.5 shows the simulated return loss and the E- and H-plane radiation patterns of

the dipole. The PHIS ground plane is square in shape with a side length of 12 cells (1.8 λ). The gain of the structure is 6.3 dBi, which compares well with the other examples, reported in [4], that utilize conventional HISs.

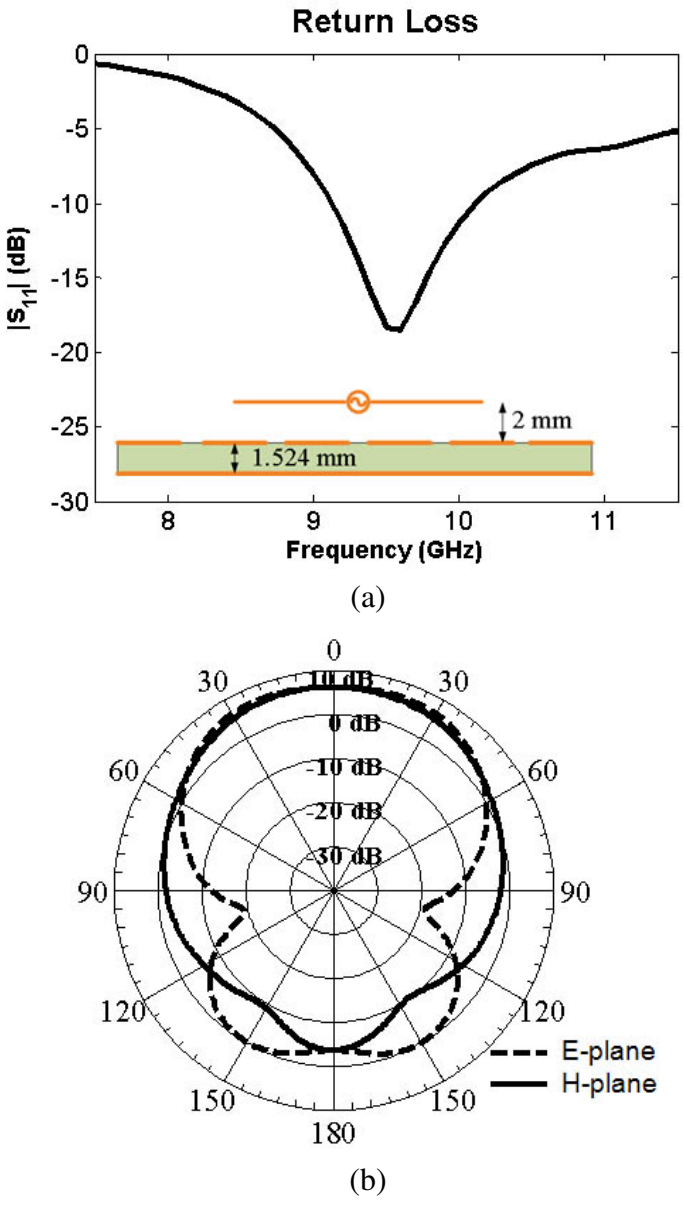

Fig. 5.5. Return loss and radiation pattern of a dipole located on top of a PHIS. One side of the PHIS is 1.8 λ in length. (a) Return loss. (b) Radiation pattern.

5.3. Surface Wave Suppression

Surface waves, which are guided by the surface of the structure, are bound to the surface and decay exponentially in the surrounding medium. Hence, they do not radiate unless they encounter a discontinuity. Metallic plates support TM surface waves because of their inductive surface impedance. However, those surface waves are loosely bound to the metal and they do radiate. If the metal is loaded with a dielectric slab, then the waves become tightly bound to the surface. At high frequencies, the surface impedance becomes capacitive and TE surface waves can also be supported.

For the case of an HIS, the grounded dielectric is loaded by a periodic array of patches, which results in an extra capacitive loading. The HISs have an inductive surface impedance before the resonance and a capacitive surface impedance after the resonance, which means that it supports TM and TE waves before and after the resonance, respectively [22].

Surface waves can be very detrimental for radiating systems and may cause some unwanted effects hindering the overall performance of the system. For instance, the unwanted radiation of surface waves from the edges of a finite sized ground plane may disturb the radiation patterns of antennas. Moreover, the surface waves in microstrip antenna arrays increase the coupling between the elements resulting in distortion of the radiation patterns, scan blindness at certain scan angles [49] and bandwidth reduction. Because of the extra capacitive loading in AMCs, the surface waves can be more tightly bound to the surface and hence, these unwanted effects may become more pronounced in some frequency bands.

To alleviate this problem, the dielectric substrate can be perforated by periodic dielectric inclusions or metallic posts [22], as in the case of a mushroom surface. Mushroom surfaces behave like two dimensional left handed structures and, within their band gap, the energy is

reflected back which prevents the propagation of surface waves. In the literature, there are various successful applications of mushroom surfaces [3]- [5], [10], [12]. However, there are basically two drawbacks of these structures. First, the surface wave suppression and AMC bands of these surfaces do not overlap all the time, and trying to overlap those bands may be highly troublesome for certain designs, especially when we have very thin substrates. Second, in a flexible circuit, the copper plated through holes are very vulnerable to bending. So, vias should be avoided in flexible or conformal applications. Finally, inclusion of vias increases the cost of fabrication.

There are other types of EBG structures in which the vias are eliminated but surface wave suppression is still possible. A very common example of such a structure is the uniplanar compact photonic band gap (UC-PBG) structure [23], [24]. In these surfaces, the center parts of the sides of the patches are notched in a rectangular form and are electrically connected by very thin lines which passes through their centers. This results in an equivalent inductance, as a consequence, the vias can be eliminated. Yet, they have narrower reflection phase bandwidths compared to HISs with square patches [9]. Besides, the overlapping problem of EBG and AMC bands is still unresolved.

Another physical realization of an EBG structure, without vias, is the Defected Ground Structure (DGS). In a DGS, some part of the ground plane is etched away to obtain the band gap. DGSs are generally used in microstrip circuits for filter design [50]- [53]. They are also used to decrease the coupling between microstrip antennas [54] and lines [55], to eliminate scan blindness [56], to control harmonic radiation of microstrip antennas [57], [58] etc. However, one drawback of DGSs is that they do not have AMC properties.

The PHIS, which is proposed in the previous section, can also be considered as a DGS loaded with a periodic array of patches. Hence, one can make use of the defects on the ground plane to achieve surface wave suppression and possibly overlap the AMC and EBG bands. In order to do this, the geometry of the PHIS should be slightly modified.

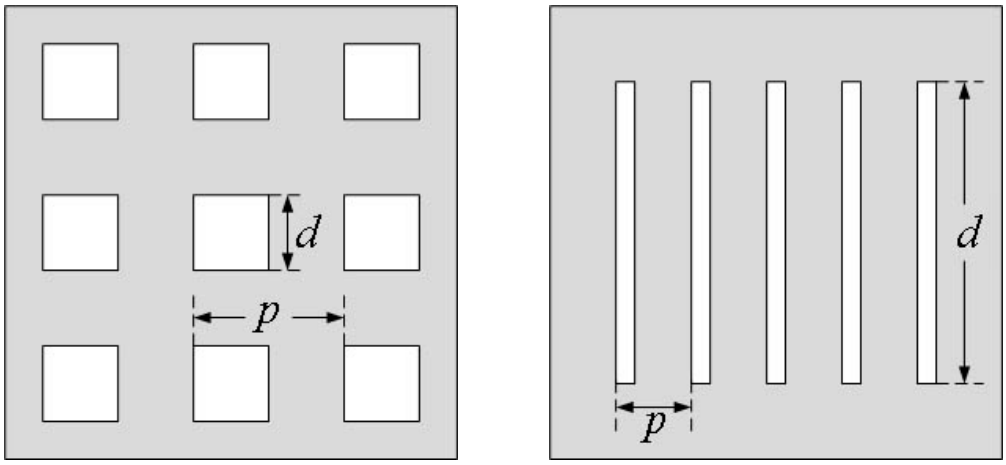

(a) (b)

Fig. 5.6. Schematic drawing of the defected ground structures. (a) Type 1 ($p > d$) (b) Type 2 ($d > p$).

DGSs can be separated into two groups. The first one is a periodic structure which is based on *Bragg's Diffraction* phenomenon. The second group, not necessarily a periodic structure, is composed of defects which form an equivalent *LC* filter. The inductance is due to the extra magnetic flux flowing through the holes, and the capacitance is due to the charges accumulating around the gaps.

Fig. 5.6 displays two different types of DGSs. In the first one, the periodicity of the defects is larger than the width of the defects ($p > d$). For this type, the rejection of waves is due to the Bragg's diffraction and the stop band occurs when $p \approx \lambda/2$ [50]. When the distance between the defects is around a half wavelength, the fields reflected from each defect interacts

constructively resulting in a strong reflection. Thus, to achieve a SW suppression, the distance between the perforations should be approximately half wavelength at the operating frequency.

In the second type, the width of the defects is larger than the periodicity ($d > p$). For this case, the slots (defects) reach resonance (infinite impedance) before the Bragg's diffraction takes place and the propagating fields are reflected back because of the high impedance per unit length [53]. This type of DGSs are also referred to as *High Impedance Wires* [53], when they are utilized in microstrip line applications. The stop band occurs when $d \approx \lambda$ [53]. The defects behave like short circuited stubs, and when the length from the center of the slot to the shorted end is approximately half wavelength, the impedance gets very high and the power is reflected back. The basic advantage of such a structure is its compactness [52].

Since the defects of Type 2 are more compact, it will be more convenient to utilize them. A slot defect, which is folded in the form of a split ring, for this type of an application, has already been reported in the literature [59]. Although promising results were obtained in terms of SW suppression, power loss was a serious issue for that design. Hence, in this dissertation, a dumbbell type defect, which allows further miniaturization and compactness, is used.

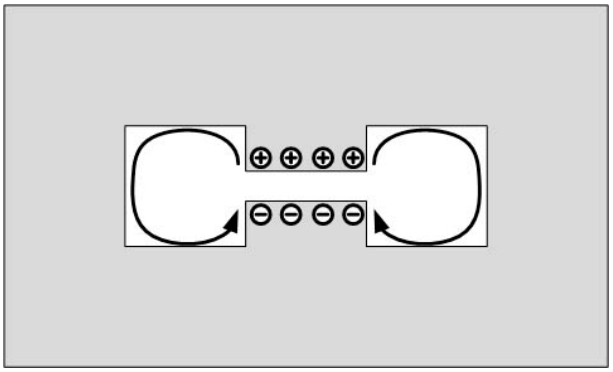

Fig. 5.7. Schematic drawing of a dumbbell type defect.

As explained previously, a dumbbell shaped defect, as shown in Fig. 5.7, can be modeled as an *LC* circuit. The capacitance is due to the charges accumulated on the two sides of the narrow slit and, the currents circulating around the holes result in an inductance [51]. A stop band occurs when the structure reaches its resonance. However, at resonance, the same structure has a pass band for a plane wave traveling in the normal direction. Therefore, a majority of the energy passes through the defect. On the other hand, such a structure may have multiple stop bands and the number of stop bands is determined by the ratio of d and p [53]. It has been observed that, the energy that passes through the defect is considerably decreased at the higher order stop bands. Hence, the structure was designed to operate at its second band to get rid of the excess power loss. To overlap the EBG and AMC bands, the size of the perforations were designed to be larger than the periodicity of the patches. The patches and perforations, together, form a larger super-cell, as illustrated in Fig. 5.8.

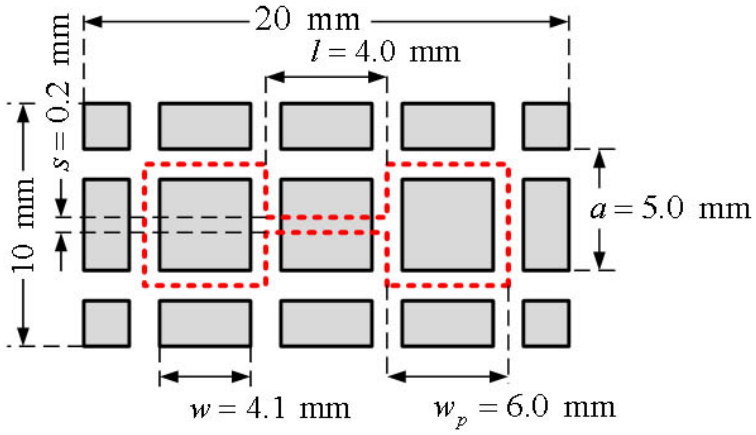

Fig. 5.8. Schematic drawing of a single super-cell of the PHIS. The dashed lines show the boundary of the perforation which is on the bottom of the substrate.

SW suppression performance of the PHIS can be tested by several simulations. For instance, the coupling between two parallel microstrip lines can be reduced when there is the

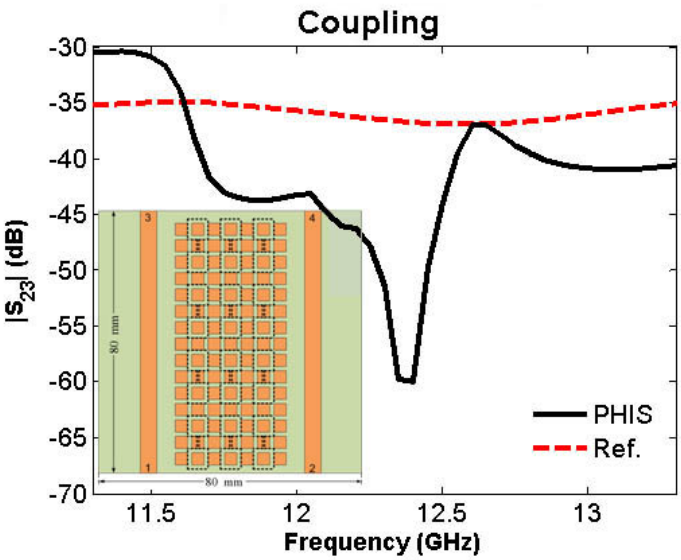

Fig. 5.9. Coupling reduction between two microstrip lines.

PHIS between them, and compared with the reference case, where there is nothing between the two lines. For such a simulation, two 50 Ω transmission lines were designed on a Rogers RT/duroid 5870 substrate with a thickness of 1.524 mm. The distance between the edges of the transmission lines was recorded as 45.5 mm, which is approximately two wavelengths within the operating band. The PHIS has three lines of defects between the transmission lines. Fig. 5.9 shows the simulation geometry and coupling reduction between ports 2 and 3, which are enumerated on the schematic drawing of the simulation geometry. Apparently, there exists a bandgap between 11.7 and 12.5 GHz. The coupling reduction is larger than 10 dB in the entire band.

The next example is the demonstration of coupling reduction between two probe fed microstrip patch antennas. As coupling between the elements of an antenna array results in scan blindness [40], it is very useful to decrease coupling. Since the maximum SW suppression for the previous simulation was obtained at 12.3 GHz, the antennas were designed to operate

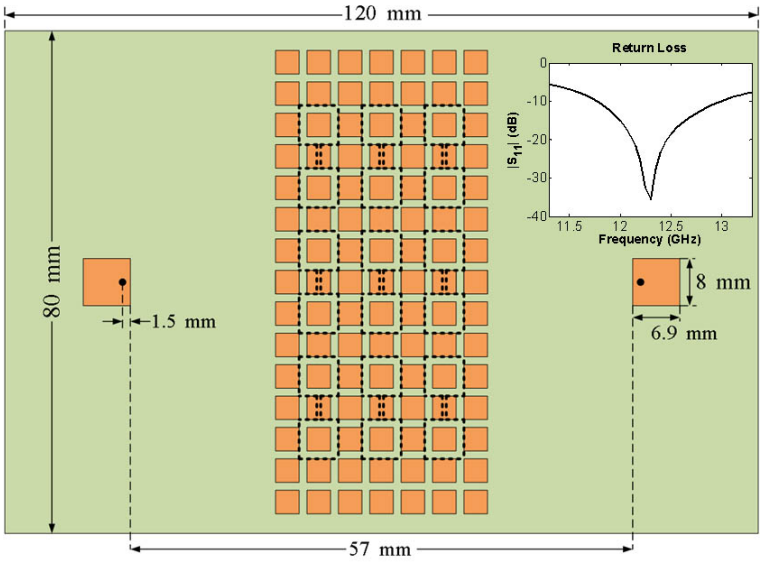

Fig. 5.10. Schematic drawing of the simulation geometry to demonstrate the coupling reduction between the microstrip patch antennas. The antennas operate around 12.3 GHz.

around that frequency. The geometry of the simulation and the simulated return loss of the antennas are illustrated in Fig. 5.10. The dielectric substrate was again Rogers RT/duroid 5870 and the antennas were fed via a coaxial probe.

The mutual coupling between the microstrip antennas was simulated for three different cases, as shown in Fig. 5.11. In the figure, *PHIS* and *Mushroom*, respectively, denote the cases where there is the proposed PHIS and the conventional mushroom surface, with exactly identical patch width and periodicity, between the antennas. Similarly, for the reference case, there is not any structure between the antennas. The radius of the vias of the mushroom surface is 0.25 mm. Clearly, the PHIS exhibits a very nice bandgap around the center frequency of the antennas. On the other hand, the maximum surface wave suppression for the mushroom surface occurs around 11.5 GHz. This is definitely an anticipated result because, the mushroom surface is not designed to have a stop band around 12.3 GHz. On the other hand,

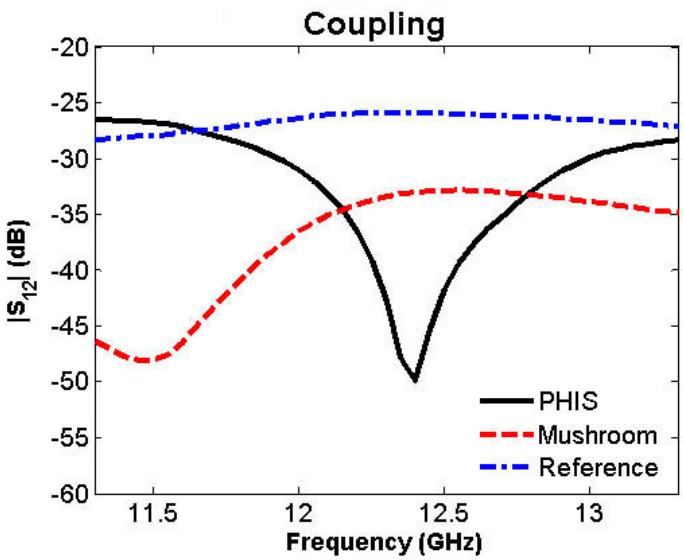

Fig. 5.11. Comparison of the mutual coupling between the antennas for three different cases. Reference: There is no structure between the antennas. Mushroom: A conventional mushroom surface between the antennas. PHIS: Perforated HIS between the antennas.

as stated in Table 5.1, a mushroom surface with identical dimensions has a reflection phase center frequency around 13.8 GHz. So, this example also verifies that the AMC and maximum surface wave suppression bands of a mushroom surface do not necessarily overlap, and it may be tedious to achieve this with a conventional HIS design.

In contrast, since one has control over both the patch and perforation dimensions, a PHIS can be designed to have overlapping AMC and EBG bands. Fig. 5.12 displays the phase and the magnitude of the reflection coefficient of the designed PHIS, for a plane wave propagating in the normal direction. The electric field is polarized in the direction perpendicular to the narrow slots on the ground plane. Apparently, the PHIS has an AMC center frequency around 12.3 GHz. In addition, the magnitude of the reflection coefficient is around -0.7 dB near the center frequency, and it is below -1 dB within the entire band. This means that energy leakage to the other side of the PHIS is within reasonable limits.

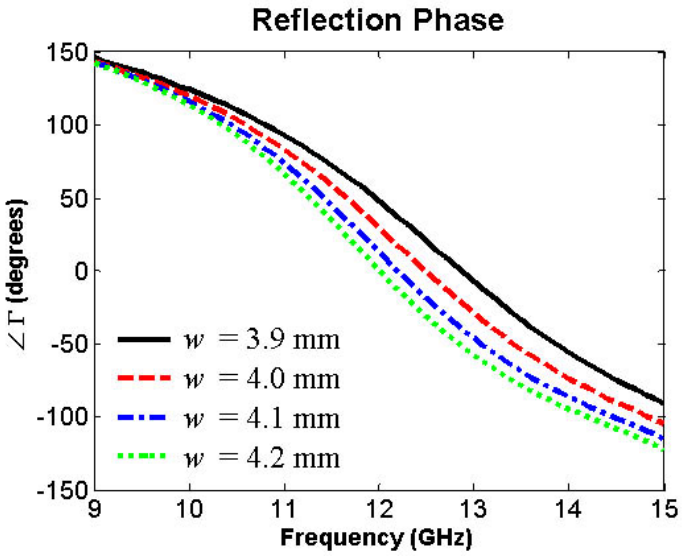

(a)

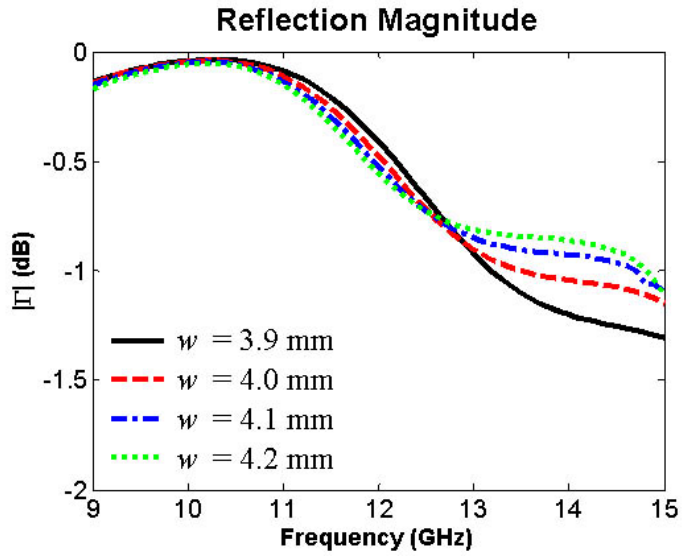

(b)

Fig. 5.12. Phase and magnitude of the reflection coefficient of the PHIS. The electric field is polarized in the direction perpendicular to the narrow slots. (a) Phase. (b) Magnitude.

EBG band of the PHIS definitely depends on the size and geometry of the perforations. In addition, position of the bandgap is also a function of the size of the patches on the top surface of the PHIS. This is attributed to the slow wave effect of the patch loading. Fig. 5.13

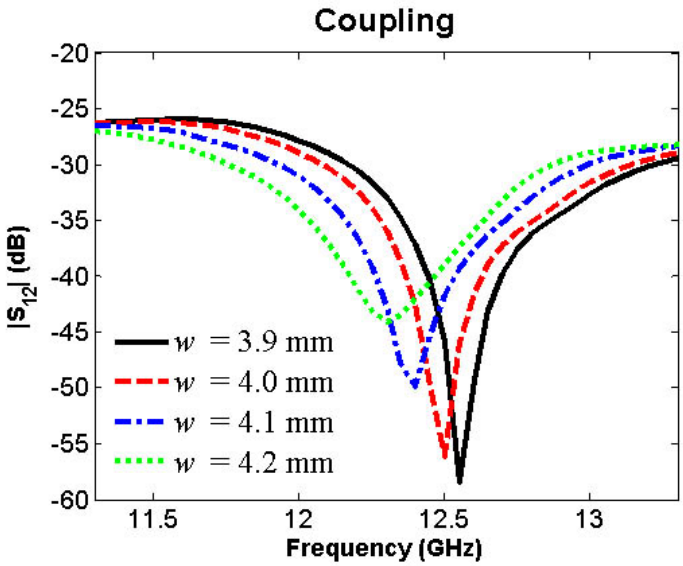

Fig. 5.13. Variation of the EBG band as a function of patch width.

shows the variation of the bandgap of the PHIS with respect to the patch width. As expected, the bandgap moves to lower frequencies as the patch width increases. Obviously, this results in a miniaturization of the surface: i.e., the EBG band of a PHIS occurs at a lower frequency compared to a conventional DGS.

If the variations of the AMC and EBG bands are compared, with respect to the patch width, one can see that the variation in the reflection phase is larger. For this particular example, as the patch width changes between 3.9 mm and 4.2 mm, the reflection phase shifts from 12.9 GHz to 12 GHz, while the bandgap shifts from 12.55 GHz to 12.3 GHz. The difference in the amount of variation of the two bands makes it possible to tune and overlap them.

The reflection and SW suppression properties of perforated structures are subject to change when other objects are placed in close proximity. However, since the PHIS is designed to minimize the power transmitted through the perforations, the impact of the presence of the other objects are also minimized. For example, placing a metallic layer of copper shifts the

EBG resonance at most 150 MHz when the distance between the PHIS and the metallic layer is 0.1 λ or greater. On the other hand, when the distance is 0.08 λ, the resonance shifts approximately 300 MHz and there is a 15 dB reduction in the coupling. Clearly, the PHIS can be designed by taking into consideration these resonance shifts due to the presence of the metallic layer.

At this point, it is worth mentioning one drawback of the PHIS with dumbbell shaped perforations. Due to the charges accumulated around the narrow slot, the capacitance of the PHIS is increased compared to the conventional HIS. Consequently, the reflection phase bandwidth has been reduced from 40.7% to 27.9%. Thus, one can conclude that there is compromise between SW suppression and bandwidth.

5.4. Experimental Verification

5.4.1. *Fabrication*

For the experimental verification of the claimed properties, the setup shown in Fig. 5.10 was fabricated by standard photolithography. Rogers RT/duroid 5870 high frequency laminates cladding with 0.5 oz. (17 μm) copper layer on both sides was used as the substrate. The first step of the process is the dehydration of the dielectric substrate. For this purpose, the substrate was baked in the oven at 120°C for 30 minutes. Since the patterning of the top and bottom surfaces is done separately, during the processing of the top surface, the bottom surface was covered with a photoresist, to protect it. AZ4620 was used as the photoresist which was spun at 1500 rpm for 30 seconds and hard baked at 120°C for 30 minutes. Then, the top surface was covered with the photoresist, at the same speed and duration. After that, the substrate is soft baked at 105°C for 9 minutes. The next step is the patterning of the antennas and

the patches which was done with the aid of the EVG620 mask aligner. The top surface was exposed to UV light with a wavelength and energy of 365 nm and 1000 mJ/cm^2, respectively. While the transparent parts of the mask allowed the UV light to pass through and illuminate the surface, the dark parts block the UV light. Then, the sample was developed in AZ400K developer, which was diluted 1:4 with water, for 4 minutes. The parts that were exposed to UV light were dissolved by the developer; the other parts remained, which protect the copper underneath from wet etching. The photolithography was followed by hard baking at 120°C for 30 minutes to strengthen the remaining photoresist. To finish, the parts which were not covered by the photoresist were etched away by Transene CE-100 copper etchant.

The same process was applied to the bottom surface, to perforate the ground plane, after the removal of the protecting photoresist by acetone. Yet, this time, the top surface was covered by the photoresist. The ground plane was patterned after it was aligned with the top surface. Fig. 5.14 illustrates the top and bottom views of the fabricated structure.

5.4.2. *Measurements*

After fabrication of the experiment setup, the mutual coupling between the antennas was measured for four different cases and the results are compared with simulations. An HP8510C Vector Network Analyzer was used as the instrumentation at the Arizona State University ElectroMagnetic Anechoic Chamber facility. The measured data was acquired at 801 frequency points between 11.3 and 13.3 GHz. A synthesized source was operated in step frequency mode, and an IF averaging factor of 2048 was used. The comparisons of the measurements and simulations are illustrated in Fig. 5.15. It can be observed that maximum SW suppression occurs at 12.55 GHz, instead of the design frequency (12.30 GHz). This frequency shift

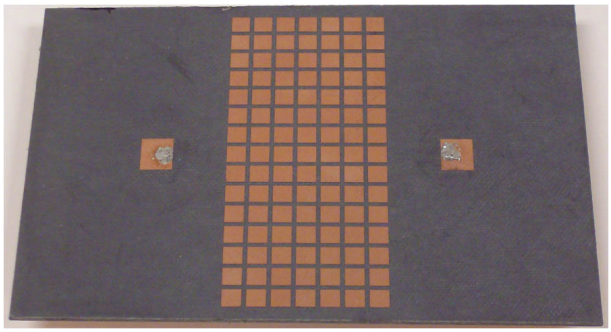

(a)

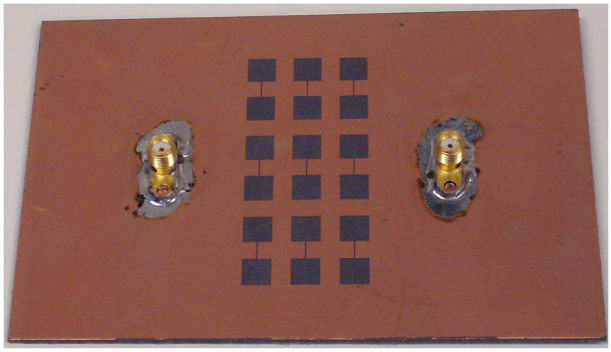

(b)

Fig. 5.14. Photographs of the fabricated PHIS and microstrip patch antennas. (a) Top view. (b) Bottom view.

is likely due to the inaccuracy of the fabrication process, particularly the undercut and non-uniformity of the etching. When the patch width and the perforation sizes are adjusted to 4.05 mm and 5.9 mm, respectively, a good agreement between simulations and measurements can be obtained. Indeed, those values are well within the reasonable range, as far as the accuracy of the fabrication is considered.

Another interesting point that is worth mentioning is that SWs are not suppressed when there is only perforations between the antennas. Indeed, the stopband of the DGS occurs at a higher frequency. However, for the PHIS case, due to the slow wave effect of the patch array, the stopband is shifted to 12.55 GHz.

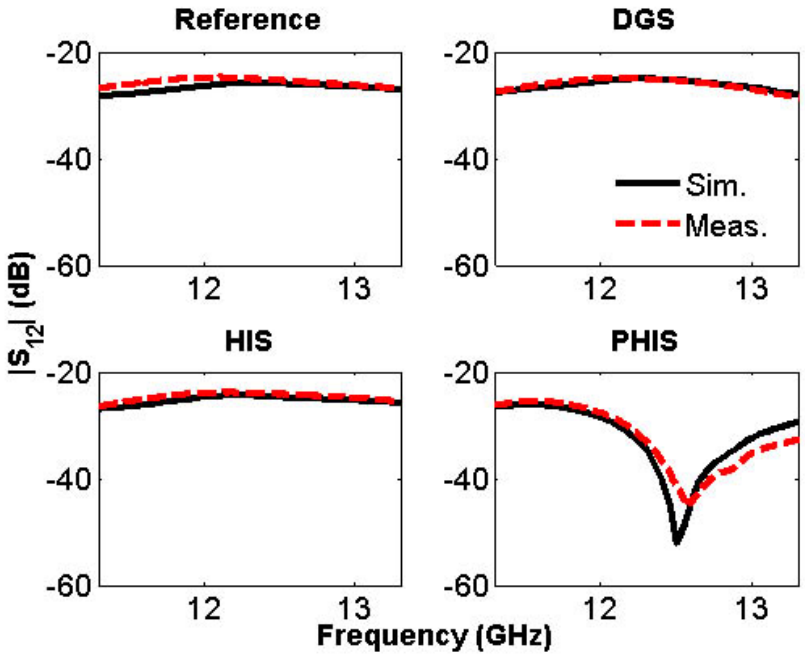

Fig. 5.15. Comparison of the simulations and measurements for four different cases. Reference: Nothing between the antennas. DGS: Only perforated ground plane between the antennas. HIS: Only conventional HIS (no vias) between the antennas. PHIS: Perforated HIS between the antennas.

CHAPTER 6

CONCLUSIONS AND RECOMMENDATIONS

6.1. Conclusions

Analysis and design of flexible HISs are investigated in this dissertation. FHISs are promising candidates for conformal low-profile antenna applications. Nevertheless, design and physical realization of such surfaces is somewhat challenging. The basic challenges are the reflection phase characterization of curved HISs, bandwidth enhancement and elimination of vias without hindering the surface wave suppression properties.

Since curved HISs have not been analyzed before, the first step should be the reflection phase characterization. There are several analytical models to obtain reflection phase diagrams of flat HISs under plane wave incidence. For many cases, those approaches are quite accurate. In addition to the analytical models, the reflection phase of a flat HIS can easily be attained with the aid of a computational tool. Since the plane wave scattering from a periodic structure is inherently a periodic problem, it is possible to get a solution by modeling a single unit cell of the structure with the appropriate boundary conditions. However, full-wave solution of the plane wave scattering problem from a curved HIS is computationally inefficient because of the asymmetry of the geometry. To alleviate this problem, an analytical method is proposed to obtain the reflection phase of the curved HIS for normal incidence. The scattered fields are expressed in terms of the cylindrical wave functions and the surface impedance of the flat HIS. Since it is relatively straightforward to obtain the flat surface impedance, this method increases the computation efficiency considerably. The results of the semi-analytical approach are compared with simulations and a good agreement is attained for some cases. However, there are some cases for which the agreement is not very good. This is due to a particular type of a current inherent to the finite periodic structures.

There are three types of currents excited on a periodic structure: Floquet currents, AGSWs and end currents. AGSWs can only be excited on finite periodic structures when the periodicity is smaller than a half wavelength. When there is only Floquet currents, the reflection phase of the curved HIS is identical to that of the flat HIS and is independent of the radius of curvature. However, when AGSWs are also excited, the reflection phase of the curved HIS deviates from that of the flat HIS and changes as a function of the curvature. The AGSWs are continuously reflected from the edges of the finite sized HIS, forming a standing wave pattern. This standing wave pattern changes with the size of the HIS. Hence, reflection phase characteristics of a curved HIS is also a function of its size.

The semi-analytical model gives accurate results when only Floquet currents are propagating. Within the frequency bands that surface waves are excited, the results of the semi-analytical method are not valid, since it does not take the surface waves into account. In these bands, the reflection phase diagram is pronouncedly distorted. Yet, it can still be used to isolate the effects of AGSWs.

The frequency band where the surface waves are excited can be obtained with the aid of the dispersion diagram, and it is independent of the curvature. However, the impact of AGSWs on flat HISs is somewhat different compared to the curved case. Despite that the surface waves change the current distribution on flat HISs, their effects on the reflection phase characteristics are not observed. This is attributed to the smaller radiation resistance associated with AGSWs, compared to that of the Floquet currents. On the other hand, for curved surfaces, they have a significant effect because the specular reflection and backscattering directions are not the same.

The effects of AGSWs on the reflection phase of a curved HIS are observed via simulations and measurements. The results show that there is a good agreement between the two. There are slight differences which may be due to the misalignments when making precise phase measurements at high frequencies. In addition, it has been shown that surface waves can be controlled by loading some of the elements with a resistive surface impedance.

An antenna mounted on a finite-sized HIS may have two different types of resonances. The resonance due to the mutual coupling between the antenna and the HIS is denoted as the *self resonance*. The self resonance frequency can be attained by calculating the driving point impedance of the antenna. On the other hand, the resonances generated by the surface waves are referred to as *surface wave resonances*, and they can be determined with the aid of a cavity model. It is verified that both types of resonances are basically independent of the curvature. However, the beamwidth of the main lobe of the radiation pattern increases as the radius of curvature decreases.

For the physical realization of FHISs, there are mainly two challenges. The first one is attributed to the small thickness of the commercially available flexible dielectric substrates. Since the bandwidth of a HIS is directly proportional to the square root of the thickness, very thin substrates may result in impractical bandwidths. To overcome this issue, a new type of HIS is proposed with a perforated ground plane. The extra magnetic flux flowing through those perforations increases the equivalent inductance of the surface which increases the bandwidth. Therefore, it is possible to miniaturize the unit cell and enhance the bandwidth at the same time, which is the major limitation of conventional HISs. The bandwidth increases (the center frequency decreases) as the size of the perforations increase. However, there is a compromise between bandwidth improvement (compactness) and reflected power. Hence, a

designer should take the power loss into account to determine the size of the perforations and unit cell dimensions.

The presence of vias in a FHIS is also a critical problem because copper posts may crack very easily when they are bent. Therefore, elimination of vias, which makes flexible EBGs physically realizable and decreases fabrication costs, without losing the surface wave suppression capability, is of great interest. Indeed, the perforated HIS, with a few modifications, can suppress surface wave propagation through the surface. Due to the holes or defects on the ground plane, PHISs behave like DGSs. In a DGS, the suppression can either be caused by Bragg's diffraction or high impedance per unit length. The rejection mechanism is determined by the ratio of perforation size and periodicity. Because of its compactness, a dumbbell-shaped DGS of the second type is utilized in this dissertation. It is shown that PHISs can efficiently suppress surface waves. In addition, the AMC and maximum surface wave suppression bands can be tuned to overlap. It is also possible to decrease the amount of power loss, due to the perforations, by operating the PHIS in its second band. Besides, a performance reduction in terms of miniaturization and bandwidth enhancement is observed when the perforations are designed to suppress SWs.

6.2. Recommendations

It may be useful to separate the recommendations into different categories. Those can be the work related to curved FHISs and PHISs.

6.2.1. *FHIS*

This dissertation focuses on the reflection phase characterization of FHISs, which are curved in the form of a cylinder. Therefore, reflection phase characterization of spherically

curved HISs can be considered as an intriguing research topic. The propagation properties of AGSWs on a doubly-curved surface and their effects on the reflection phase characteristics of FHISs can be investigated. Besides, in this work, the radius of curvature is taken as a constant. The reflection phase of arbitrarily curved HISs can also be examined as a future work.

In terms of low-profile antenna applications, the performance a wire dipole antenna has been investigated and the results were verified by simulations only, although there were some preliminary measurement data. Hence, as an immediate future work, more reliable measurement data can be obtained, and the indications of the dissertation can be strengthened. In addition, the behavior of other types of antennas, in close proximity of curved HISs, can be studied in more detail. This may include narrow band antennas like microstrip patches, as well as some wide band antennas like bow-tie dipoles and spirals. Undoubtedly, a comprehensive research on the performance of wide band antennas on curved HISs will be a challenging endeavor.

Finally, since the phase variation on an HIS can be controlled by the patch size, the utilization of tunable curved HISs for dynamic field collimation can also be a promising research topic.

6.2.2. *PHIS*

It has been indicated that the geometry of the perforations should be modified to suppress surface waves. However, this results in reduced bandwidth, which seems to be the main compromise of the PHIS design. Therefore, other types of perforation geometries can be investigated to overcome this drawback. It may be extremely useful to increase the bandwidth and suppress the surface waves simultaneously.

A few preliminary results about the performance of dipole antennas on PHISs has been discussed in this dissertation. As a continuation, the performance of different types of antennas, including monopoles, bow-tie dipoles and microstrip patch antennas on PHISs, can be investigated. Particularly, the performance of wide band antennas, which may take the full advantage of enhanced bandwidth of PHISs, can be of great interest.

REFERENCES

[1] C. A. Balanis, *"Advanced Engineering Electromagnetics,"* 2^{nd} edition, Hoboken, NJ: John Wiley & Sons, 2012.

[2] B. A. Munk, *"Finite Antenna Arrays and FSS,"* Hoboken, NJ: John Wiley & Sons, 2003.

[3] F. Yang and Y. Rahmat-Samii, "Reflection phase characterizations of the ebg ground plane for low profile wire antenna applications," *IEEE Trans. Antennas Propag.*, vol. 51, no. 10, pp. 2691 – 2703, 2003.

[4] F. Yang and Y. Rahmat-Samii, *"Electromagnetic Band Gap Structures in Antenna Engineering,"* Cambridge, UK: Cambridge University Press, 2009.

[5] A. Vallecchi, J. R. De Luis, F. Capolino, and F. De Flaviis, "Low Profile Fully Planar Folded Dipole Antenna on a High Impedance Surface," *IEEE Trans. Antennas Propag.*, vol. 60, no. 1, pp. 51 – 62, 2012.

[6] M. Z. Azad and M. Ali, "Novel Wideband Directional Dipole Antenna on a Mushroom Like EBG Structure," *IEEE Trans. Antennas Propag.*, vol. 56, no. 5, pp. 1242 – 1250, 2008.

[7] L. Akhoondzadeh-Asl, D. J. Kern, P. S. Hall, and D. H. Werner, "Wideband Dipoles on Electromagnetic Bandgap Ground Planes," *IEEE Trans. Antennas Propag.*, vol. 55, no. 9, pp. 2426 – 2434, 2007.

[8] H. Mosallaei and K. Sarabandi, "Antenna Miniaturization and Bandwidth Enhancement Using a Reactive Impedance Substrate," *IEEE Trans. Antennas Propag.*, vol. 52, no. 9, pp. 2403 – 2414, 2004.

[9] D. Sievenpiper, "Artificial Impedance Surfaces," Chapter 15, in *Modern Antenna Handbook*, C. A. Balanis (editor), John Wiley & Sons, pp. 737 – 777, 2008.

[10] L. Zhang, J. A. Castaneda, and N. G. Alexopoulos, "Scan blindness free phased array design using PBG materials," *IEEE Trans. Antennas Propag.*, vol. 52, no. 8, pp. 2000 – 2007, 2004.

[11] E. Rajo-Iglesias, Ó. Quevedo-Teruel, and L. Inclán-Sánchez, "Mutual Coupling Reduction in Patch Antenna Arrays by Using a Planar EBG Structure and a Multilayer Dielectric Substrate," *IEEE Trans. Antennas Propag.*, vol. 56, no. 6, pp. 1648 –1655, 2008.

[12] D. Qu, L. Shafai, and A. Foroozesh, "Improving microstrip patch antenna performance using EBG Substrates," *IEE Proc. Microw. Antennas Propag.*, vol. 153, no. 6, pp. 558 –563, 2006.

[13] T. Nakamura and T. Fukusako, "Broadband Design of Circularly Polarized Microstrip Patch Antenna Using Artificial Ground Structure With Rectangular Unit Cells," *IEEE Trans. Antennas Propag.*, vol. 59, no. 6, pp. 2103 –2110, 2011.

[14] D. F. Sievenpiper, J. H. Schaffner, H. J. Song, R. Y. Loo, and G. Tangonan, "Two-dimensional beam steering using an electrically tunable impedance surface," *IEEE Trans. Antennas Propag.*, vol. 51, no. 10, pp. 2713 – 2722, 2003.

[15] D. F. Sievenpiper, "Forward and Backward Leaky Wave Radiation with Large Effective Aperture from an Electronically Tunable Textured Surface," *IEEE Trans. Antennas Propag.*, vol. 53, no. 1, pp. 236 – 247, 2005.

[16] B. H. Fong, J. S. Colburn, J. J. Ottusch, J. L. Visher, and D. F. Sievenpiper, "Scalar and Tensor Holographic Artificial Impedance Surfaces," *IEEE Trans. Antennas Propag.*, vol. 58, no. 10, pp. 3212 –3221, 2010.

[17] O. Luukkonen, F. Costa, C. Simovski, A. Monorchio, and S. A. Tretyakov, "A Thin Electromagnetic Absorber for Wide Incidence Angles and Both Polarizations," *IEEE Trans. Antennas Propag.*, vol. 57, no. 10, pp. 3119 –3125, 2009.

[18] A. C. Durgun, C. A. Balanis, C. R. Birtcher and D. R. Allee, "Design, Simulation, Fabrication and Testing of Flexible Bow-Tie Antennas," *IEEE Trans. Antennas Propag.*, vol. 59, no. 12, pp. 4425 – 4435, 2011.

[19] J. So, J. Thelen, A. Qusba, G. J. Hayes, G. Lazzi, and M. D. Dickey, "Reversibly deformable and mechanically tunable fluidic antennas," *Advanced Functional Materials*, vol. 19, no. 22, pp. 3632 – 3637, Oct. 2009.

[20] L. Yang, R. Zhang, D. Staiculescu, C. Wong, and M. Tentzeris, "A novel conformal rfid-enabled module utilizing inkjet-printed antennas and carbon nanotubes for gas-detection applications," *Antennas and Wireless Propagation Letters, IEEE*, vol. 8, pp. 653 –656, 2009.

[21] [Online]. Available: http://www.dupont.com/plastics/

[22] D. Sievenpiper, High-Impedance Electromagnetic Surfaces, Ph.D. dissertation, Department of Electrical Engineering, UCLA, 1999.

[23] R. Coccioli, Fei-Ran Yang, Kuang-Ping Ma, and T. Itoh, "Aperture-coupled patch antenna on UC-PBG substrate," *IEEE Trans. Microwave Theory and Tech.* , vol. 47, no. 11, pp. 2123 – 2130, 1999.

[24] B. Lin, Q. Zheng, and N. Yuan, "A Novel Planar PBG Structure for Size Reduction," *IEEE Microw. and Wireless Comp. Letters*, vol. 16, no. 5, pp. 269 – 271, 2006.

[25] S. A. Tretyakov, *"Analytical Modeling in Applied Electromagnetics,"* Norwood, MA: Artech House, 2003.

[26] M. Gustafsson, and D. Sjöberg, "Physical bounds and sum rules for high-impedance surfaces," *IEEE Trans. Antennas Propag.*, vol. 59, no. 6, pp. 2196 – 2204, 2011.

[27] M. F. Samani, and R. Safian, "On bandwidth limitation and operating frequency in artificial magnetic conductors," *IEEE Antennas and Wireless Propag. Letters*, vol. 9, pp. 228 – 231, 2010.

[28] C. R. Brewitt-Taylor, "Limitation on the bandwidth of artificial perfect magnetic conductor surfaces," *IET Microw. Antennas Propag.*, vol. 1, no. 1, pp. 255 – 260, 2007.

[29] O. Luukkonen, C. Simovski, G. Granet, G. Goussetis, D. Lioubtchenko, A. Raisanen, and S. Tretyakov, "Simple and accurate analytical model of planar grids and high-impedance surfaces comprising metal strips or patches," *IEEE Trans. Antennas Propag.*, vol. 56, no. 6, pp. 1624 –1632, 2008.

[30] S. Clavijo, R. E. Díaz, and W. E. McKinzie,"High-Impedance Surfaces: An Artificial Magnetic Conductor for a Positive Gain Electrically Small Antennas," *IEEE Trans. Antennas Propag.,* Vol. 51, No. 10, pp. 2678-2690, 2003.

[31] [Online]. Available: http://www.3m.com

[32] [Online]. Available: http://www.ansoft.com/products/hf/hfss/

[33] R. A. Depine, "Scattering of a wave at a periodic boundary: analytical expression for the surface impedance," *J. Opt. Soc. Am. A,* vol. 4, no. 4, pp. 507–510, 1988.

[34] D. S. Janning and B. A. Munk, "Effects of Surface Waves on the Currents of Truncated Periodic Arrays," *IEEE Trans. Antennas Propag.*, vol. 50, no. 9, pp. 1254 –1265, 2002.

[35] D. S. Janning, Surface Waves in Arrays of Finite Extent, Ph.D. dissertation, Department of Electrical Engineering, OSU, 2000.

[36] O. A. Civi and P. H. Pathak,"Array guided surface waves on a finite planar array of dipoles with or without a grounded substrate," *IEEE Trans. Antennas Propag.*, vol. 54, no. 8, pp. 2244–2252, Aug. 2006.

[37] J. B. Pryor, Suppression of Surface Waves in Arrays of Finite Extent, M.S. thesis, Department of Electrical Engineering, OSU, 2000.

[38] J. R. Wait, "On the Input Impedance of a Hertzian Dipole over a Flat Surface," *IEEE Trans. Antennas Propag.*, vol. 18, no. 1, pp. 119 – 121, 1969.

[39] D. C. Chang and J. R. Wait, "Appraisal of Near Field Solutions for a Hertzian Dipole Over Conducting Half Spaces," *Can. J. Phys.*, vol. 48, no. 6, pp. 737 – 743, 1970.

[40] C. A. Balanis, *"Antenna Theory: Analysis and Design,"* 3^{rd} edition, Hoboken, NJ: John Wiley & Sons, 2005.

[41] I. T. McMichael, A. I. Zaghloul, and M. S. Mirotznik, "A Method for Determining Optimal EBG Reflection Phase for Low Profile Dipole Antennas," *IEEE Trans. Antennas Propag.*, vol. 61, no. 5, pp. 2411 – 2417, 2013.

[42] M. F. Abedin and M. Ali, "Effects of EBG Reflection Phase Profiles on the Input Impedance and Bandwidth of Ultrathin Directional Dipoles," *IEEE Trans. Antennas Propag.*, vol. 53, no. 11, pp. 3664 – 3672, 2005.

[43] F. Costa, O. Luukkonen, C. R. Simovski, A. Monorchio, S. A. Tretyakov, P. M. de Maagt, "TE Surface Wave Resonances on High-Impedance Surface Based Antennas: Analysis and Modeling" *IEEE Trans. Antennas Propag.* , vol. 59, no. 10, pp. 3588–3596, Oct. 2011.

[44] P. Wounchoum, D. Worasawate, C. Phongchaoenpanich, and M. Krairiksh, "A Two-Slot Array Antenna on a Concentric Sectoral Cylindrical Cavity Excited by a Coupling Slot," *Progress In Electromagnetic Research*, vol. PIER 86, pp. 135 – 154, 2008.

[45] K. Sarabandi and N. Behdad, "A Frequency Selective Surface With Miniaturized Elements," *IEEE Trans. Antennas Propag.*, vol. 55, no. 5, pp. 1239 – 1245, 2007.

[46] Q. R. Zheng, Y. Q. Fi, and N. C. Yuan, "A novel compact electromagnetic band-gap (EBG) structure," *IEEE Trans. Antennas Propag.*, vol. 56, no. 6, pp. 1656 –1660, 2008.

[47] J. McVay, N. Engheta, and A. Hoorfar, "Space filling curve high-impedance ground planes," Chapter 14, in *Metamaterial Physics and Engineering Explorations,* N. Engheta, R.W. Ziolkowski (editors), John Wiley & Sons, Publishers, Inc., pp. 377 – 402, 2006.

[48] [Online]. Available: http://www.rogerscorp.com/products/index.aspx

[49] D. M. Pozar, and D. H. Schaubert, "Scan blindness in infinite phased arrays of printed dipoles," *IEEE Trans. Antennas Propag.*, vol. AP-32, no. 6, pp. 602 – 610, 1984.

[50] T.-Y. Yun, and K. Chang, "Uniplanar One-Dimensional Photonic-Bandgap Structures and Resonators," *IEEE Trans. Microw. Theory and Tech.*, vol. 49, no. 3, pp. 549 – 551, 2001.

[51] H. Kim, and B. Lee, "Bandgap and Slow/Fast-Wave Characteristics of Defected Ground Structures (DGSs) Including Left-Handed Features," *IEEE Trans. Microw. Theory and Tech.*, vol. 54, no. 7, pp. 3113 – 3120, 2006.

[52] C. Caloz, H. Okabe, T. Iwai, and T. Itoh, "A Simple and Accurate Model for Microstrip Structures With Slotted Ground Plane," *IEEE Microw. and Wireless Comp. Letters*, vol. 14, no. 4, pp. 133 – 135, 2004.

[53] A. M. E. Safwat, S. A. Tretyakov, and A. V. R*äisä*nen, "High-Impedance Wire," *IEEE Antennas and Wireless Propag. Letters*, vol. 6, pp. 631 – 634, 2007.

[54] S. Xiao, M.-C. Tang, Y.-Y. Bai, S. Gao and B.-Z. Wang, "Mutual Coupling Suppression in Microstrip Array Using Defected Ground Structure," *IET Microw. Antennas Propag.*, vol. 5, no. 12, pp. 1488 – 1494, 2011.

[55] K. M. K. H. Leong, A. C. Guyette, B. Elamaran, W. A. Shiroma, and T. Itoh, "Coupling Suppression in Microstrip Lines Using a Bi-Periodically Perforated Ground Plane," *IEEE Microw. and Wireless Comp. Letters*, vol. 12, no. 5, pp. 169 – 171, 2002.

[56] D.-B. Hou, S. Xiao, B.-Z. Wang, L. Jiang, J. Wiang, and W. Hong, "Elimination of Scan Blindness with Compact Defected Ground Structures in Microstrip Phased Array," *IET Microw. Antennas Propag.*, vol. 3, no. 2, pp. 269 – 275, 2009.

[57] Y. Horii, and M. Tsutsumi, "Harmonic Control by Photonic Bandgap on Microstrip Patch Antenna," *IEEE Microw. Guided Wave Letters*, vol. 9, no. 1, pp. 13 – 15, 1999.

[58] H. Liu, Z. Li, X. Sun, and J. Mao, "Harmonic Suppression With Photonic Bandgap and Defected Ground Structure for a Microstrip Patch Antenna," *IEEE Microw. and Wireless Comp. Letters*, vol. 15, no. 2, pp. 55 – 56, 2005.

[59] A. C. Durgun, C. A. Balanis and C. R. Birtcher, "Surface Wave Suppression Properties of Perforated Artificial Impedance Surfaces," presented at *Antennas and Propagation Society International Symposium (APSURSI), 2013 IEEE.*